Floating Membranes
molecular structure and orientation
at the water-lipid interface

Floating Membranes
molecular structure and orientation at the water-lipid interface

academisch proefschrift

ter verkrijging van de graad van doctor
aan de Universiteit van Amsterdam
op gezag van de Rector Magnificus
prof. dr. D.C. van den Boom
ten overstaan van een door het college voor promoties
ingestelde commissie,
in het openbaar te verdedigen in de Agnietenkapel
op dinsdag 15 september 2009 om 14:00 uur

door

Maria Sovago

geboren te Baia Mare, Roemenië

Promotiecommissie

promotor:	prof. dr. M. Bonn
overige leden:	prof. dr. H. J. Bakker
	prof. dr. W-J. Buma
	prof. dr. P. G. Bolhuis
	prof. dr. E. Vartiainen
	dr. M. S. Pshenichnikov
	dr. S. Roke

ISBN 978-90-5776-1980

The work described in this thesis was performed at the *FOM Institute for Atomic and Molecular Physics* (AMOLF), Sciencepark 113, 1098SJ, Amsterdam, The Netherlands. The work is part of the research programme of the *Stichting Fundamenteel Onderzoek der Materie* (FOM), which is financially supported by the *Nederlandse Organisatie voor Wetenschappelijk Onderzoek* (NWO).

Publications:

This thesis is based on the following publications:

Chapter 3:

Polarization-resolved broad-bandwidth sum-frequency generation spectroscopy of monolayer relaxation
M. Smits, M. Sovago, G. W. H. Wurpel, D. Kim, M. Müller, M. Bonn
Journal of Physical Chemistry C **2007***, 111, 8878-8883*

Chapter 4:

Calcium induced phospholipid ordering depends on surface pressure
M. Sovago, G. W. H. Wurpel, M. Smits, M. Müller, M. Bonn
Journal of the American Chemical Society **2007***, 129, 11079-11084*

Chapter 5:

1. Vibrational response of hydrogen-bonded interfacial water is dominated by intramolecular coupling
M. Sovago, R. K. Campen, G. W. Wurpel, M. Müller, H. J. Bakker, M. Bonn
Physical Review Letters **2008**, 100, 173901-173904

2. Sovago et al. Reply
M. Sovago, R. K. Campen, G. W. H. Wurpel, M. Müller, H. J. Bakker, M. Bonn
Physical Review Letters **2008**, 101, 139402

3. Hydrogen bonding strength of interfacial water determined with Sum-frequency Generation
M. Sovago, R. K. Campen, H. J. Bakker, M. Bonn
Chemical Physics Letters **2009**, 470, 7-12

Chapter 6:

Determining absolute molecular orientation at interfaces: a phase retrieval approach for sum-frequency generation spectroscopy
M. Sovago, E. Vartiainen, M. Bonn
Journal of Physical Chemistry C **2009**, 113, 6100-6106

Contents

Chapter 1

Introduction

1.1 Water-lipid interactions

This thesis is about lipids and water and their interaction. Lipids are the basic building blocks of the cell membrane. The membrane keeps the cell- the smallest unit of life- together as an entity. The cell membrane is formed by a lipid bilayer in between two water phases: one towards the inside of the cell (intracellular fluid) and one towards the outside the cell (extracellular fluid). Interfacial water directly interacting with the lipid bilayer plays a crucial role in membrane formation and function [1]. Furthermore, interfacial water is of importance in other biological processes (e.g. protein folding, ions transport) and other disciplines, including electrochemistry and (photo-) catalysis [2-7]. Despite its importance, our understanding of interfacial water has lagged that achieved for bulk [8]. Knowledge of the details of water interfacial structure is essential both for a fundamental understanding of this ubiquitous liquid, and for the many technological applications where aqueous interfaces are relevant [1, 9-11].

Water interfaces are characterized by the interruption of the bulk hydrogen bonded network, which gives interfacial water its unique properties (e.g. high surface tension). When a water OH group forms a hydrogen bond, the OH stretch frequency of this group decreases by an amount determined by the H-bond strength. As such, the frequency and lineshape of the O-H stretch vibration of water provide a sensitive markers of the local environment of water molecules. Therefore, vibrational spectroscopies can be used to investigate water structure, by probing its hydroxyl stretch vibration (see, e.g., Figure 1.1). However, a distinct challenge in the study of interfacial water exists, which lies in the specific investigation of the water molecules that participate in forming the interface, as for the majority of experimental approaches the response of the interfacial water molecules remains buried beneath the overwhelming response of the bulk.

The use of even-order non-linear optical techniques provides a solution to this problem, as their selection rules result in the suppression of the signal from the isotropic bulk, and make them inherently sensitive to the region where the bulk structure breaks down, i.e. the interface. Indeed, the second-order technique of

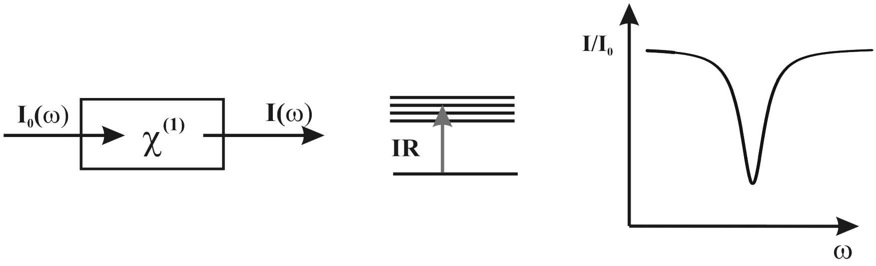

Figure 1.1 Schematic illustration of the optical processes involved in vibrational spectroscopy. When the infrared light is resonant with the vibrational modes of the molecules, part of the incoming light, I_0, is absorbed. In the intensity spectrum, this absorption appears as a dip.

vibrational sum frequency generation (VSFG) has been shown to be a very versatile tool in the study of interfacial water [12-20]. In VSFG, an infrared (IR) and a visible beam are combined at an interface to generate a signal at the sum frequency of the infrared and visible frequencies [21] (see Figure 1.2). When the IR frequency is resonant with the O-H stretch vibration of interfacial water, the sum-frequency signal is strongly enhanced, providing the vibrational spectrum of essentially one monolayer of water molecules at the interface. As such, the water molecules hydrating the lipids at the interface can be probed.

1.2 Sum-frequency generation

As mentioned above, vibrational sum-frequency generation (VSFG) spectroscopy can be used to investigate specifically surfaces and interfaces, in contrast to other vibrational specroscopies. Here we will show the differences between typical vibrational spectroscopy and the non-linear sum-frequency spectroscopy.

A non-invasive way of probing the vibrations of a molecule is to use photons. Information at the molecular level can be obtained if the energy of the photons matches the energy difference between energy levels of the molecules. To resonantly interact with a vibrational mode, the photons need to have infrared frequencies. The electromagnetic infrared field (E) drives oscillations in the molecules and as such a polarization P is created, given by:

$$P(\omega)=\chi^{(1)}(\omega)E(\omega),$$

where $\chi^{(1)}$ represents the first order susceptibility. When the infrared field is resonant with the vibrational modes of the molecules, the individual dipoles of the individual molecules add up to a macroscopic polarization. This polarization will radiate an electric field which will interfere destructively with the incoming infrared field. As such, the destructive interference will appear as dips in the resulting intensity spectrum (see Figure 1.1). In such a case, both the bulk and the surface vibrations are measured simultaneously.

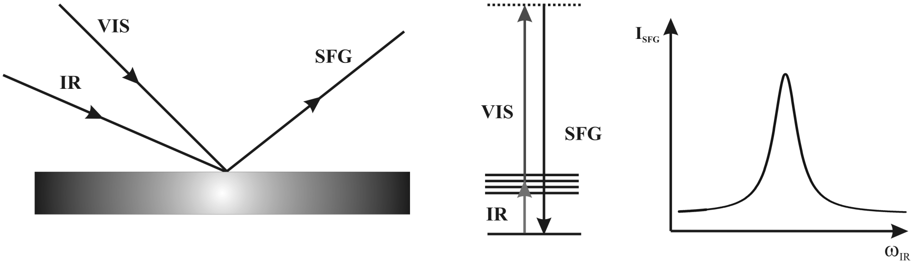

Figure 1.2 Schematic illustration of the sum-frequency generation process. The two incoming beams at the surface, with infrared and visible frequency, respectively, generate a photon with the sum of the frequencies, through a non-linear interaction with the medium. The middle panel represents the molecular level scheme for the resonant sum-frequency process. The resulting SFG intensity appears as a peak as a function of IR frequency, as shown in the right panel.

In the non-linear process of sum-frequency generation, the signal from the bulk is suppressed, as in such a medium this process is forbidden. Here, two photons interact with the medium: one having an infrared frequency and the other a visible frequency (see Figure 1.2). The created non-linear polarization, $P^{(2)}$, due to the interaction of the two electric fields, E_{IR} and E_{VIS}, with the molecules at the surface, is given by:

$$P^{(2)}(\omega_{SFG})=\chi^{(2)}(\omega_{SFG})E_{VIS}(\omega_{VIS})E_{IR}(\omega_{IR}) \tag{1.1}$$

Here $\chi^{(2)}$ is the second-order susceptibility. The polarization given by equation 1.1 radiates an electric field at the sum of the frequency of the IR and VIS photons. This field becomes large when the infrared field is resonant with the vibrational modes of the molecules at the surface. To illustrate the surface specificity of the SFG technique, let us consider that the incoming electric fields invert sign. In such a case, the induced polarization must change sign as well. However, for a medium with inversion symmetry, the second-order susceptibility $\chi^{(2)}$ does not invert sign. Equation 1.1 thus becomes:

$$-P^{(2)}(\omega_{SFG})=\chi^{(2)}(\omega_{SFG})E_{VIS}(\omega_{VIS})E_{IR}(\omega_{IR}) \tag{1.2}$$

Equations 1.1 and 1.2 can be satisfied simultaneously only when $\chi^{(2)} = 0$. Thus, SFG is forbidden in a medium possessing inversion symmetry, and SFG can only occur when $\chi^{(2)}$ is non-zero. At the surface, symmetry is broken, $\chi^{(2)}$ is non-zero and the sum-frequency process is allowed.

An example of the surface specificity of the SFG technique is provided by the SFG spectrum of the heavy water-air interface, shown in Figure 1.3. It contains spectral features originating from specific interfacial water molecules: the ‘free-OD’ from a water molecule with an O-D bond protruding from the surface, centered around

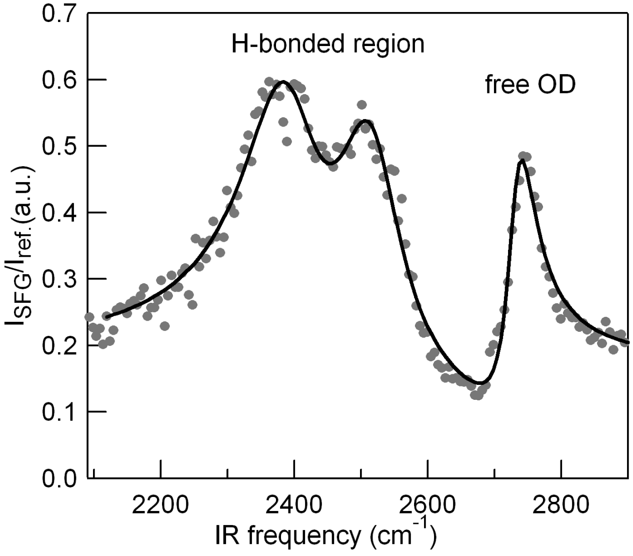

Figure 1.3 SFG spectra of the heavy water/air interface. The narrow peak centered around 2730 cm^{-1} is assigned to the 'free O-D' originating from interfacial water molecules having an OD protruding from the surface into the air. The presence of this peak demonstrates the surface sensitivity of the SFG spectroscopy. Fits to the data are shown by the thin solid lines.

2730 cm^{-1} [13, 14, 17-20] and two peaks in the H-bonded frequency region. It is clear that such spectrum reflects the SFG surface specificity, as the free O-D mode is present only at the surface.

1.3 Broad-band SFG

In narrow-band Sum-Frequency Generation (SFG) technique, the visible and the infrared pulses used to generate the sum-frequency response light have picosecond time duration. In this case, the IR frequency needs to be scanned over the frequency range of interest in order to record the SFG spectrum of the vibrational modes under study. In broad-band SFG, a femtosecond IR pulse is combined at the surface with a picosecond VIS pulse (the VIS narrow spectral bandwidth providing the spectral resolution of the SFG experiment). The IR pulse typically covers a frequency window of ~200 cm^{-1}, such that a multitude of vibrational modes are probed by the infrared profile at once. The advantage of this approach is that the sample response is recorded with every individual laser pulse at all frequencies. Therefore, all data points in the SFG spectrum are measured under the same conditions. Since in this mode of operation every pair of laser pulses contributes to the whole spectrum, the signal-to-noise ratio of the acquired spectra in broad-band configuration is inherently not limited by the laser fluctuations, generally leading to improved SFG spectra.

1.4 Maximum Entropy Method applied to SFG

The non-linear optical susceptibility $\chi^{(2)}$ that relates the driving fields to the sum-frequency polarization (see equation 1.1) is generally described as a combination of a constant non-resonant background and resonant terms, each resonant term originating from a specific molecular vibration. The resonant contributions to $\chi^{(2)}$ contain details about molecular orientation at the interface, as the absolute orientation of the transition dipole moment associated with a vibrational mode is directly correlated with the sign of the resonant amplitude [14, 22]. As such, the SFG technique can in principle be used to determine the molecular orientation. It has been challenging, however, to determine both the phase and the magnitude of the resonant contribution from the SFG spectrum, as the absolute square of the $\chi^{(2)}$ is experimentally measured.

The phase information lost in VSFG, can be experimentally determined from interferometric measurements, as shown by the recent phase-sensitive SFG method [23-25]. However, the phase can also be retrieved using an alternative approach: Maximum Entropy Method (MEM) that is directly used on SFG spectra. MEM is a proven method to retrieve the phase information from intensity spectra [26-31]. Maximum Entropy method is based on a mathematical algorithm that maximizes the entropy in a spectrum.

The method has been successfully employed in third-harmonic generation spectroscopy [28], coherent anti-stokes Raman scattering (CARS) [26, 27, 29], and VSFG spectroscopy [30, 31]. We will use this approach to determine the molecular orientation, and the method is described in detail in chapter 6 of this thesis.

1.5 This thesis

The goal of this thesis is to investigate water-lipid interactions using broad-band SFG spectroscopy. More specifically, we determine the lipid and water conformation and orientation at surfaces of self-assembled monolayers of lipids on water.

In chapter 2, the experimental technique of sum-frequency generation and of surface pressure measurements are described in detail. The data analysis and their interpretation are also presented.

An improvement of the broad-band SFG setup is presented in chapter 3. Namely, a new conformation of the setup allows for the simultaneous recording of SFG spectra with different polarization combinations of the SFG, visible and infrared beams. This method is particularly advantageous for studies in which surface properties are time-dependent, such as kinetic studies. The technique is illustrated by a study that mimics the lung surfactant relaxation during the breathing cycle: a lipid monolayer is compressed from a disordered phase to an ordered phase, and then the monolayer is allowed to relax to its initial state. During the relaxation process, the lipid tails are first changing their orientation on a time scale of tens of seconds, and subsequently the lipids respread to form a homogeneous disordered phase.

Further, the effects of ions on zwitterionic and anionic lipids are investigated. The results are presented in chapter 4. We find that sodium ions do not change significantly the lipid monolayer structure. In contrast, the divalent calcium ion-effects on monolayer are large and strongly depend on the surface pressure. At low surface pressures (~5 mN/m), the presence of Ca^{2+} results in the unexpected appearance of ordered domains. For pressures between ~5 and ~25 mN/m, Ca^{2+} ions induce molecular disorder in the monolayer. For pressures exceeding 25 mN/m, calcium cations expand the monolayer, while simultaneously ordering the lipid chains. Interestingly, these effects are similar for both zwitterionic lipids and negatively charged lipids. In both vibrational sum-frequency generation and surface tension measurements, the molecular signature of the association of Ca^{2+} with the lipids is evident from Ca^{2+}- induced changes in the signals corresponding to area changes of 4 $Å^2$/lipid – precisely the surface area of a Ca^{2+} ion, with evidence for a change in lipid:Ca^{2+} complexation at high pressures.

Chapter 5 focuses on the SFG spectrum of interfacial water, and the interpretation of the double-peaked structure that appears in the vibrational surface response for all aqueous interfaces. We demonstrate that the two spectral features originate from vibrational coupling between the stretch and bending overtone, rather than from structural effects. This is demonstrated by isotopic dilution experiments, which reveal a smooth transition from two peaks to one peak, as D_2O is converted into HDO. Our results show that the water interface is structurally more homogeneous than previously thought. Furthermore, these results imply that the average hydrogen bond strength and its distribution must be inferred through the center frequency and width, respectively, of the O-D stretch vibration of isotopically diluted HDO in H_2O. We find that at the water HDO-air interface, the SFG spectrum in the hydrogen-bonded region strongly resembles the Raman spectrum, indicating that at this interface the interfacial hydrogen bonding properties are very similar to those in bulk water. In contrast, for HDO interfaces of silica-water and lipid-water, interfacial hydrogen bonding is substantially stronger, with a larger degree of heterogeneity.

In chapter 6 we present the numerical algorithm of Maximum Entropy Method applied to SFG spectra to retrieve the absolute phase of the sum-frequency response. From the obtained absolute phase we are able to determine the molecular orientation – i.e. whether molecular groups are pointing ‘up’ or ‘down’ – with respect to the interface. The phase retrieval algorithm is successfully applied to spectra containing different resonance widths and various levels of nonresonant backgrounds.

After testing and establishing the MEM algorithm in this chapter, it is used further in chapter 7, where the water orientation and structure near different types of lipid headgroups is investigated. Here we compare the water orientation at phospholipid-water interface with the orientation found at simple surfactants-water interfaces. Our results demonstrate that water molecules near classical cationic surfactant are oriented with their O-H groups pointing down, i.e. with their oxygen towards the surfactant charge, and that the orientation is inverted when the surfactant charge becomes negative. Remarkably, at the negatively charged phosholipid-water interface and at the zwitterionic lipid-water interface, water orients with its oxygen up, towards the air phase. The orientation of water at phospholipid interfaces is therefore opposite to those of simple surfactants, which is due to the presence of ‘buried’ water molecules between the phospholipid headgroups and their alkyl chain.

Following the approach of determining the water structure and its heterogeneity at the surface used in chapter 5, the change in water structure is also investigated near different types of lipid headgroups. We find that water molecules situated below the lipid headgroup form stronger H-bonds than 'buried' water molecules. Additionally, we find that charged lipid headgroups induce a larger heterogeneity of the water structure.

References:

[1] J. Milhaud, Biochim. Biophys. Acta **1663**, 19 (2004).
[2] I. Benjamin, Acc. Chem. Res. **28**, 233 (1995).
[3] I. Benjamin, Chem. Rev. **106**, 1212 (2006).
[4] G. E. Brown, V. E. Henrich, W. H. Casey, et al., Chem. Rev. **99**, 77 (1999).
[5] T. M. Chang and L. X. Dang, Chem. Rev. **106**, 1305 (2006).
[6] P. Jungwirth and D. J. Tobias, Chem. Rev. **106**, 1259 (2006).
[7] C. J. Mundy and I. F. W. Kuo, Chem. Rev. **106**, 1282 (2006).
[8] A Comprehensive Treatise of Water, edited by F. Franks (Plenum, New York, 1972).
[9] M. A. Henderson, Surf. Science Rep. **46**, 1 (2002).
[10] S. K. Shaw and A. A. Gewirth, J. Electroanal. Chem. 609, **94** (2007).
[11] A. Verdaguer, G. M. Sacha, H. Bluhm, et al., Chem. Rev. **106**, 1478 (2006).
[12] A. V. Benderskii, J. Henzie, S. Basu, et al., J. Phys. Chem. B **108**, 14017 (2004).
[13] Q. Du, E. Freysz, and Y. R. Shen, Science **264**, 826 (1994).
[14] Q. Du, R. Superfine, E. Freysz, et al., Phys. Rev. Lett. **70**, 2313 (1993).
[15] W. Gan, D. Wu, Z. Zhang, et al., J. Chem. Phys. **124**, 114705 (2006).
[16] S. Gopalakrishnan, D. F. Liu, H. C. Allen, et al., Chem. Rev. **106**, 1155 (2006).
[17] D. E. Gragson and G. L. Richmond, J. Phys. Chem. B **102**, 3847 (1998).
[18] E. A. Raymond and G. L. Richmond, J. Phys. Chem. B **108**, 5051 (2004).
[19] E. A. Raymond, T. L. Tarbuck, M. G. Brown, et al., J. Phys. Chem. B **107**, 546 (2003).
[20] M. J. Shultz, S. Baldelli, C. Schnitzer, et al., J. Phys. Chem. B **106**, 5313 (2002).
[21] Y. R. Shen, Nature **337**, 519 (1989).
[22] D. K. Hore, D. K. Beaman, D. H. Parks, et al., J. Phys. Chem. B **109**, 16846 (2005).
[23] N. Ji, V. Ostroverkhov, C. Y. Chen, et al., J. Am. Chem. Soc. **129**, 10056 (2007).
[24] N. Ji, V. Ostroverkhov, C. S. Tian, et al., Phys. Rev. Lett. **100**, 96102 (2008).
[25] V. Ostroverkhov, G. A. Waychunas, and Y. R. Shen, Phys. Rev. Lett. **94**, 46102 (2005).
[26] H. A. Rinia, M. Bonn, M. Muller, et al., Chem. Phys. Chem. **8**, 279 (2007).
[27] E. M. Vartiainen, J. Opt. Soc. Am. B: Opt. Phys. **9**, 1209 (1992).
[28] E. M. Vartiainen, K. E. Peiponen, H. Kishida, et al., J. Opt. Soc. Am. B: Opt. Phys. **13**, 2106 (1996).
[29] E. M. Vartiainen, H. A. Rinia, M. Muller, et al., Opt. Express **14**, 3622 (2006).
[30] P. K. Yang and J. Y. Huang, J. Opt. Soc. Am. B: Opt. Phys. **14**, 2443 (1997).
[31] P. K. Yang and J. Y. Huang, J. Opt. Soc. Am. B: Opt. Phys. **17**, 1216 (2000).

Chapter 2

Experimental Techniques

In this chapter, we describe the experimental techniques which are used to characterize water surfaces and phospholipid monolayers. This chapter starts with a description of the preparation of the phospholipid monolayers, and continues with the characterization of the lipid monolayers using surface pressure measurements, e.g. pressure-area compression isotherm measurements at room temperature. In the second part of this chapter, the sum-frequency generation (SFG) setup is presented and typical SFG spectra are shown. Furthermore, we show how the obtained SFG spectra are analyzed and interpreted.

2.1 Introduction

Phospholipid monolayers represent an excellent model system for biological membranes, as the cell membrane can be considered as two weakly coupled monolayers [1]. As the phospholipids are amphiphilic molecules, they self-assemble on water surface to form a well-defined monolayer, with their headgroups (the hydrophilic part) in the water and their hydrocarbon chains (the hydrophobic part) in the air. In such a monolayer conformation, the surface pressure of the system can be easily controlled by compression such that the different phases of the lipids can be monitored (as described below in section 2.3). Moreover, the water subphase of the lipid monolayer can be easily altered by injecting different molecules, e.g. ions (see chapter 4) or proteins [2].

To characterize the lipid monolayers, we use two complementary techniques: surface pressure measurements and Sum-Frequency Generation (SFG) Spectroscopy. In the surface pressure measurements, we monitor the surface pressure as the lipid monolayer is compressed, at room temperature. The obtained surface pressure curve as a function of area per molecule is called compression isotherm and it represents a macroscopic measure of the phase behavior of the entire monolayer (see section 2.3).

In order to characterize the lipid-water interface from the molecular point of view, the surface pressure measurements are complemented with SFG measurements. In the latter, information on lipid conformation is provided, averaged over a probing area of ~ 10^{-2} mm^2. We employ here broad-band SFG, where two laser pulses are overlapped at the interface: one in the visible (VIS) frequency range and the other in the mid-infrared (IR) to generate sum-frequency photons. The SFG process requires the inversion symmetry to be broken, a requirement that is fulfilled at an interface. Therefore, SFG is a surface-specific spectroscopy. Moreover, SFG is resonantly enhanced when the IR photons are resonant with a vibrational transition at the surface. In broad-band SFG, the IR beam is temporally short (broad in the frequency domain) so that several vibrational modes are probed at once. The IR beam is upconverted with a narrow-band VIS beam (long in the time domain), its width giving the spectral resolution of the experiments. Short VIS (800 nm) pulses, of typically 100 fs duration, are readily produced by an amplified Ti:Sapphire laser system. In our setup, part of the generated VIS beam is used to generate the IR pulses using an optical parametric generation and amplification process, as described in section 2.4. The other part is used to generate narrow-band VIS pulses used in the SFG process.

This chapter starts with the description of the sample preparation, and continues with the description of the surface pressure measurements (section 2.3). In section 2.4, the SFG setup is described, including the laser system, the IR generation, the SFG generation process and the SFG detection. The chapter ends with a brief presentation of typical SFG spectra, their analysis and interpretation.

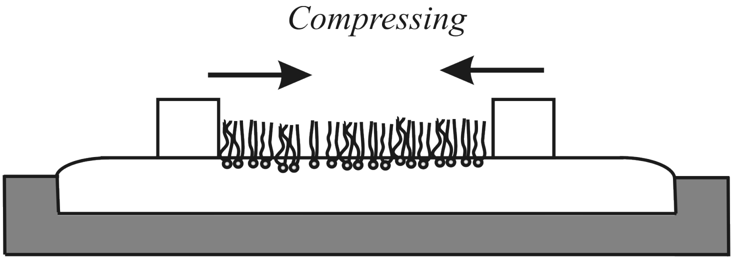

Figure 2.1 Schematic representation of the Langmuir trough used to measure the compression isotherms. Two barriers are used to compress the lipid monolayer, such that the area per molecule is reduced.

2.2 Sample preparation

The phospholipids were obtained from Avanti Polar Lipids, and were used without further purification. The lipids were dissolved in chloroform (Sigma-Aldrich) to form a ~1.5 mM solution. Between experiments, the lipid solution was kept in the freezer at -20°C. The monolayers were prepared at room temperature (22°C) in a home-built Teflon trough (7 X 7 cm^2), unless otherwise specified. The Teflon trough was carefully cleaned using the following procedure. The trough was kept in 2% Hellmanex soap (Hellma GmbH&Co, Germany) solution in Millipore water (18.2 MΩ cm resistivity) over night, and then the soap was removed by rinsing the trough with hot water. Afterwards, the trough was rinsed with Ethanol (Sigma-Aldrich, 99%) and Millipore water. The lipid solution was spread drop-by-drop (0.5 μl each) onto phosphate buffer subphase (pH ≈ 7). For the experiments where the water modes were probed, heavy water (Cambridge Isotope Laboratories, Inc., 99,93% purity) was used as the monolayer subphase. To ensure surface cleanliness, the water surface was cleaned before the lipid monolayers were applied by aspiring water from the surface. The phosphate buffer was prepared by dissolving 0.12 g of monosodium phosphate (NaH_2PO_4) in 90 ml of Millipore water and titrated at pH = 6.99 with sodium hydroxide or hydrochloric acid. Finally, the volume was increased to 100 ml using Millipore water. Using the drop-by-drop spreading method, the surface pressure of monolayers can be controlled between 0-40 mN/m.

2.3 Compression isotherms

As mentioned in the introduction, a macroscopic measure of the phase behavior of the lipid monolayers, surface pressure measurements were performed. A schematic representation of the setup used to measure the compression isotherms (pressure-area π-A) is depicted in Figure 2.1. A commercial Langmuir trough (Kibron Inc, Finland)

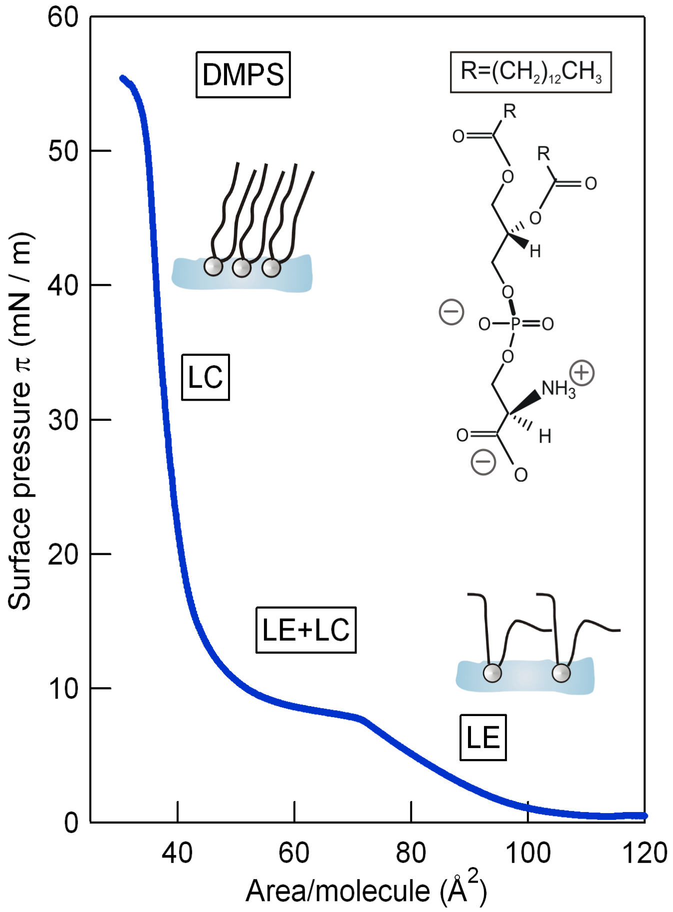

Figure 2.2 Pressure-area (π-A) isotherm of a DMPS monolayer on phosphate buffer at pH = 7. The liquid expanded phase (LE), liquid condensed phase (LC) and the coexistence region of the two phases (LE+LC) are indicated along the isotherm, together with a schematic representation of the monolayer conformation. Inset: the chemical structure of DMPS.

is used and the monolayer was compressed by two barriers at a compression rate of 5 Å^2/chain/min. The surface pressure, π, was measured with a tensiometer using the Wilhelmy plate method. In this method, a thin plate is used to measure the surface tension by suspending it at the water-air interface. By measuring the force on the plate due to the wetting, the surface pressure can be determined. With this setup the surface pressure of monolayers can be controlled between 0-60 mN/m.

As an illustration of a typical surface pressure measurement, we will discuss in the following a compression isotherm and the information that can be extract from it regarding the lipid phases. As a typical example of a Langmuir isotherm, we show the compression of *L*-1,2-Dimyristoyl-*sn*-glycerol-3-phosphoserine (DMPS) monolayer (Figure 2.2). On water, the phase behavior of DMPS is well documented [3]. With decreasing surface area, the following regions have been identified: a gas phase ($A > 110$ Å^2/molecule), a liquid expanded (LE) phase between 70 and 110 Å^2/molecule, a plateau characteristic of the coexistence of the LE and the liquid condensed (LC) phase ($\pi \approx 10$ mN/m), and the pure LC phase for pressures above 10 mN/m. In the LE phase, the lipid tails are disordered and they occupy a large area. When the area per lipid is reduced by compression, the lipids undergo a conformational change, from a disordered to a more ordered phase (see the cartoons in Figure 2.2). The compression isotherm can be further used to monitor the phase change when the conditions of the monolayer changes: mixture between two or more lipid components, or when the water subphase changes [4-8]. We followed the change in the compression isotherms when mono- and divalent ions were present in the water subphase and the results are presented and discussed in chapter 4.

2.4 Sum-Frequency Generation setup

In the following, we are going to describe the SFG setup used to investigate the lipid-water interface. The SFG setup is depicted schematically in Figure 2.3. It consists of a laser system and components associated with infrared (IR) generation, the SFG generation and SFG detection. Each of these parts are described in detail in the following subsections.

2.4.1 Laser system

The laser system consists of a Coherent Legend regenerative amplifier (Regen) seeded by a Coherent Vitesse Ti:Sapphire oscillator (790 nm central wavelength, 100 fs pulse duration FWHM, 80 MHz repetition rate, 500 mW output power) and pumped by a Coherent Evolution laser (527 nm central wavelength, 200 ns temporal FWHM, 1 kHz repetition rate, 23 W output power). The output of the Regen amplifier is centered around 800 nm, has a temporal FWHM of 120 fs and 1 kHz repetition rate. 1.5 W of the 2.5 W ouput power of the Regen is used to run the SFG experiments. The beam is split in two parts: 1 W is used to pump an OPA and generate the infrared (IR) pulses, and the rest of 0.5 W of the VIS beam is used as the upconversion pulse in the SFG generation.

2.4.2 IR generation

The IR pulses used to perform SFG experiments are generated in two steps through optical parametric generation and amplification processes (TOPAS, Light Conversion Inc.). In the first step, two near-infrared pulses (signal S and idler I) are generated in a β-BBO$_3$ (beta-barium borate) crystal in the range of 1-2.5 μm through optical parametric generation and amplification processes. In these processes, part of the 800 nm beam is used as a seed to generate broad-band super-fluorescence in the β-BBO$_3$ crystal. The resulting super-fluorescence has low intensity and is amplified by the rest of the 800 nm beam in an optical parametric amplification process.

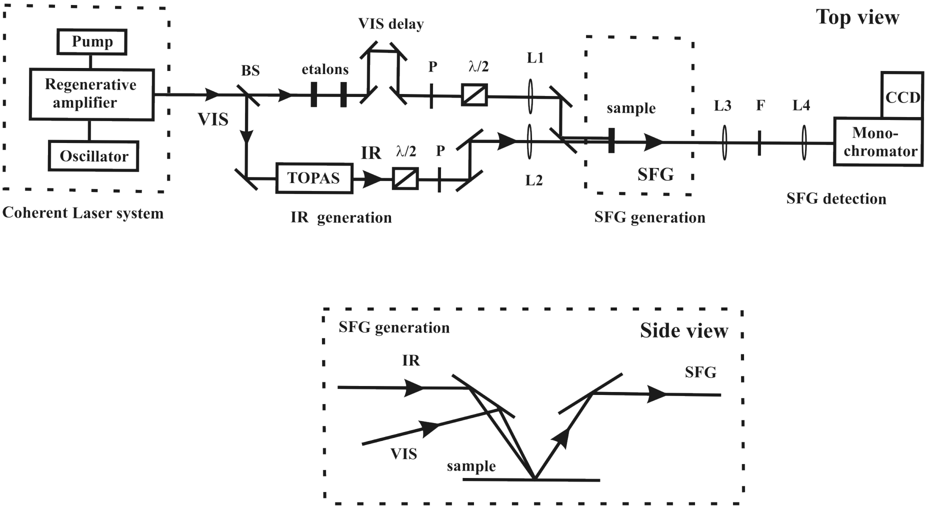

Figure 2.3 Schematic representation of the broad-bandwidth SFG setup. The output from the regenerative amplifier is split into two part using a beamsplitter (BS): one part is used to pump an optical parametric generator/amplifier (TOPAS) with a difference frequency unit to produce the broad-bandwidth IR-pulses; the other part is passed through one or two etalons (for O-D or C-H region measurements, respectively) to produce narrow-bandwidth VIS-pulses. The polarization of the two beams is controlled by using a λ/2-plate (to rotate the polarization) and a polarizer (P, to clean the polarization). The two beams are focused with two lenses (L1 and L2 with focal lengths *f* = 30 and 5 cm, respectively) onto the sample and the SFG signal is collected using a collimating lens, L3 (*f* = 10 cm). Finally, the SFG signal is focused onto the slit of the spectrometer using a fourth lens (L4, *f* = 5 cm). The residual visible (800 nm) light is filtered out using a short wave pass filter (SWP). The signal is spectrally analyzed using a monochromator, coupled to a CCD camera. The bottom panel depicts a side view of the detection part of the setup.

In this process, a selected range of frequencies from the broad spectrum of the superfluorescence is amplified to generate the signal and the idler beams. The overall conversion efficiency of the 800 nm in the generation and amplification stage is approximately 30%. The frequencies of signal and idler are chosen by angle-tuning the β-BBO_3 crystal. In the second step, mid-IR pulses are generated in a $AgGaS_2$ crystal, by non-colinear difference frequency mixing of S and I. The IR pulses have typical energies of 10 μJ, and can be tuned in the frequency range of 3-10 μm by changing the angle of the $AgGaS_2$ crystal.

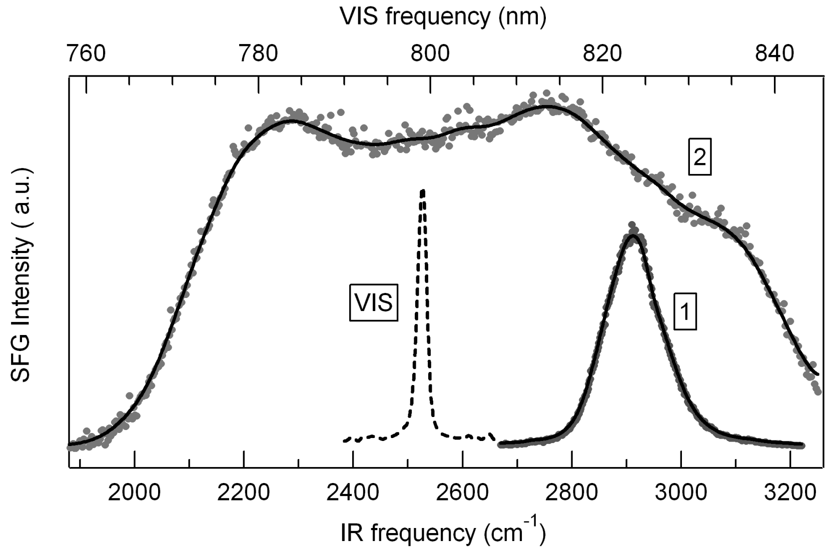

Figure 2.4 The SFG spectrum obtained from a piece of *z*-cut quartz, for IR centered around 2900 cm^{-1} (spectrum 1) and varying its frequency in the region 2050 cm^{-1} and 3250 cm^{-1} (spectrum 2). The solid lines are a guide for the eye. Those spectra are used as a reference to account for the variations of the IR power over the spectral range measured, as explained in the text. The SFG spectra shown here also show the profile of IR beam used for the experiments in the C-H stretch region (spectrum1) and for C-H and O-D stretch region (spectrum 2), respectively. The profile of the VIS beam, centered around 800nm, is also shown (top axis).

2.4.3 SFG experiment

The SFG light was generated by overlapping visible pulses in space and time with infrared pulses. For the experiments in the C-H stretch region, the VIS pulse was shaped by two etalons in series, obtaining pulses with spectral full-width at half-maximum (FWHM) of 15 cm^{-1}. The IR pulse was centered at 2900 cm^{-1}, having a bandwidth of 200 cm^{-1} (see spectrum 1 in Figure 2.4). An example of the obtained SFG spectrum in this region is given in Figure 2.7. For the experiments where both C-H and O-D stretch modes were probed, the VIS was shaped by only one etalon, obtaining pulses with a spectral width of FWHM = 25 cm^{-1}. The IR center frequency was varied continuously between 2050 cm^{-1} and 3250 cm^{-1} so that the whole O-D and C-H vibrational region of ~1200 cm^{-1} is covered (see spectrum 2 in Figure 2.4). The measured SFG spectrum will contain, therefore, vibrational modes from both the lipid tails and the interfacial water, as will be shown in section 2.5.3. Both IR and VIS beams were focused down to approximately 100 μm beam waist. The incident angles of VIS and IR beams were 35° and 40° with respect to the surface normal, respectively, unless otherwise specified.

2.4.4 SFG detection

The SFG light was spectrally dispersed by a monochromator and detected by an intensified Charge- Coupled Device (iCCD, Roper Scientific). For the experiments presented in chapter 7, an Electron-Multiplied CCD (EMCCD, Andor Technologies) was used. The SFG spectra may be recorded under different polarization conditions (*s* and *p*) of the three light fields. The most common polarization combination used in the experiments presented in this thesis is *s*-polarized SFG, *s*-polarized VIS, and *p*-polarized IR (*ssp*); spectra are recorded under these conditions unless otherwise specified. Under *ssp* polarization conditions, the lipid monolayers give the largest signal. Data were acquired for typically 3 minutes for measurements in the C-H stretch region and 6 minutes when both C-H and O-D modes were probed. Finally, the spectra were normalized using a reference signal from a *z*-cut quartz plate.

2.5 Data analysis

To extract the intensities of the different modes present in the SFG spectrum (e.g. methyl or methylene modes), we fit the obtained SFG spectra using a Lorentzian model, as described below. The obtained intensities can be used to determine the lipid tail orientation (as shown in chapter 3 and 4) or to calculate the imaginary parts of the SFG response (see chapter 6). In the following, we will describe in detail the model used and we will give two typical examples of the SFG spectra analysis: one for a spectrum where the modes from the lipid tails are probed (in the C-H stretch region, section 2.5.2), and the other where both the lipid and the interfacial water modes are probed (section 2.5.3).

2.5.1 Lorentzian model

The measured SFG intensity is proportional to the modulus square of the second-order susceptibility, $\chi^{(2)}$, as described in chapter 1 [9]:

$$I_{SFG} \propto |\chi^{(2)} E_{VIS} E_{IR}|^2 ,$$

where E_{VIS} and E_{IR} are the electric fields of the incident VIS and IR beams, respectively.

When the frequency of the incident infrared field is resonant with a vibrational mode, *n*, the SFG field can be strongly enhanced. Then the susceptibility $\chi^{(2)}$ consists of a nonresonant (NR) and a resonant (RES) term:

$$\chi^{(2)} = \chi^{(2)}_{NR} + \chi^{(2)}_{RES} = A_{NR} e^{i\varphi_{NR}} + \sum_n \frac{A_n}{\omega_n - \omega_{IR} - i\Gamma_n} \tag{2.1}$$

Here, A_{NR} represents the amplitude of the nonresonant susceptibility, ϕ_{NR} its phase, A_n is the amplitude of the nth vibrational mode with the resonant frequency ω_n, and Γ_n is the line width of the transition.

The surface susceptibility $\chi^{(2)}$ is related to the hyperpolarizability, $\alpha^{(2)}$, of the individual molecules at the surface by:

$$\chi^{(2)}=N_S\langle\alpha^{(2)}\rangle$$

where N_S is the surface density of molecules, and the angular brackets denote orientational averaging over the position of the molecules. Analogous to $\chi^{(2)}$, the molecular hyperpolarizability can be written as a sum of a nonresonant and a resonant term:

$$\alpha^{(2)}=\alpha_{NR}^{(2)}+\sum_n\frac{a_n}{\omega_n-\omega_{IR}-i\Gamma_n}$$

where the microscopic amplitude a_n is related to A_n by:

$$A_{n,ijk}^{(2)}=N_S\sum_{lmn}\langle(\hat{i}\,\hat{l})(\hat{j}\,\hat{m})(\hat{k}\,\hat{n})\rangle a_{n,lmn} \qquad (2.2)$$

Here the subindices i, j and k refer to the lab reference frame (x,y,z) and l, m and n to the molecular reference frame (a,b,c) (see Figure 2.5). SFG theory shows that the strength of each resonance a_n is described as [10]:

$$a_{n,lmn}^{(2)}=\frac{1}{2\varepsilon_0\omega_n}\frac{\partial\mu_n}{\partial Q}\frac{\partial\alpha_{lm}}{\partial Q} \qquad (2.3)$$

Here, ε_0 is the permittivity in vacuum, and $\partial\mu_n/\partial Q$ and $\partial\alpha_{lm}/\partial Q$ are the derivatives of the infrared dipole moment and the Raman polarizability for the normal mode Q, respectively. Equations (2.2) and (2.3) show that the amplitude A_n is directly related to the orientation of the IR transition dipole moment and the sign of it can be used to infer the molecular orientation at the surface, e.g. whether molecular groups are pointing ‘up’ or ‘down’ with respect to the surface. Examples of determining the molecular orientation at the surface are presented in chapter 6 and 7. Furthermore, A_n is nonzero only when both IR and Raman transitions are spectroscopically allowed. Hence, a vibrational mode is SFG active when it is both IR and Raman active. The sign of A_n is typically found from the spectral fit using the Lorentzian model described by equation (2.1).

To illustrate this model we simulated a SFG spectrum containing only one resonance. The $|\chi^{(2)}|^2$ spectrum together with the corresponding real (Re) and imaginary (Im) parts and the phase of the $\chi^{(2)}$ are displayed in Figure 2.6. The

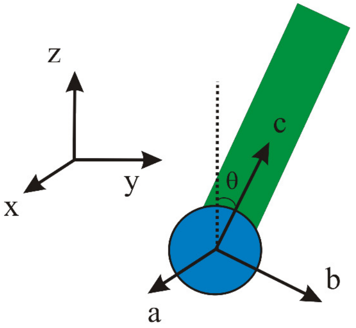

Figure 2.5 A schematic representation of a lipid molecule with the lab (x,y,z) and the molecular frames (a,b,c). The c axis is along the lipid tail, and the tilt of the lipid tail is defined as the angle between c and z.

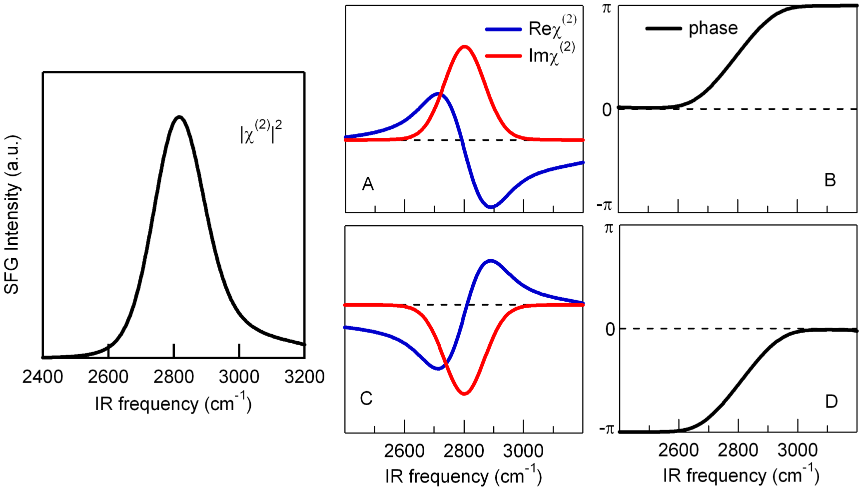

Figure 2.6 Simulated SFG spectrum with one Lorentzian peak centered at 2800 cm^{-1}. The corresponding real, imaginary and phase of $\chi^{(2)}$ for positive resonant amplitude (A,B) and negative amplitude (C, D), respectively. In both cases, the same $|\chi^{(2)}|^2$ spectrum is obtained.

parameters used are: $A_{NR} = 0$, $A = \pm 50$, $\omega_0 = 2800$ cm^{-1} and $\Gamma = 150$ cm^{-1}. The sign of the resonant amplitude has an influence on the resulting Re, Im and phase of $\chi^{(2)}$. For $A > 0$, the Im[$\chi^{(2)}$] is positive, while the Re[$\chi^{(2)}$] is positive for frequencies $\omega < \omega_0$ and negative for $\omega > \omega_0$. The resulting phase increases smoothly from 0 to π. When the sign of the amplitude is inverted (when the molecular orientation flips), Im[$\chi^{(2)}$] and Re[$\chi^{(2)}$] change sign and the phase varies now between $-\pi$ and 0 (see Figure 2.6 C,D). This simulation illustrates the variations of Im[$\chi^{(2)}$], Re[$\chi^{(2)}$] and phase[$\chi^{(2)}$] values around the resonant frequency ω_0. Note that the nonresonant phase, ϕ_{NR}, can have an influence on the apparent sign of the resonant amplitude (see equation 2.1): by changing the ϕ_{NR} with π and inverting the sign of the resonant amplitude A_n, the same $|\chi^{(2)}|^2$ spectrum can be obtained. The resulting $\mathrm{Im}[\chi^{(2)}]$ and $\mathrm{Re}[\chi^{(2)}]$ spectra will change sign, as both are proportional with A_n. As discussed in chapter 6, the set of parameters (ϕ_{NR}, A_n) found from a fitting routine using equation (2.1) for a given SFG spectrum is not unique. To unambiguously determine the sign of A_n, we applied Maximum Entropy Method (MEM), a proven numerical algorithm that retrieves the phase of $\chi^{(2)}$ from the $|\chi^{(2)}|^2$ spectrum (see details in chapter 6).

2.5.2 SFG response in the C-H stretch region

Further, we will show the typical results of the fit procedure for a SFG spectrum obtained in the C-H stretch region (2800-3000 cm^{-1}) from a DMPS monolayer (Figure 2.7). In this region, four vibrational modes can be observed: the peaks centered at 2875, 2935 and 2960 cm^{-1} have been assigned to the CH_3 symmetric stretch (CH_3*ss*), CH_3 Fermi Resonance (CH_3FR) and the CH_3 asymmetric stretch (CH_3*as*), respectively [9].

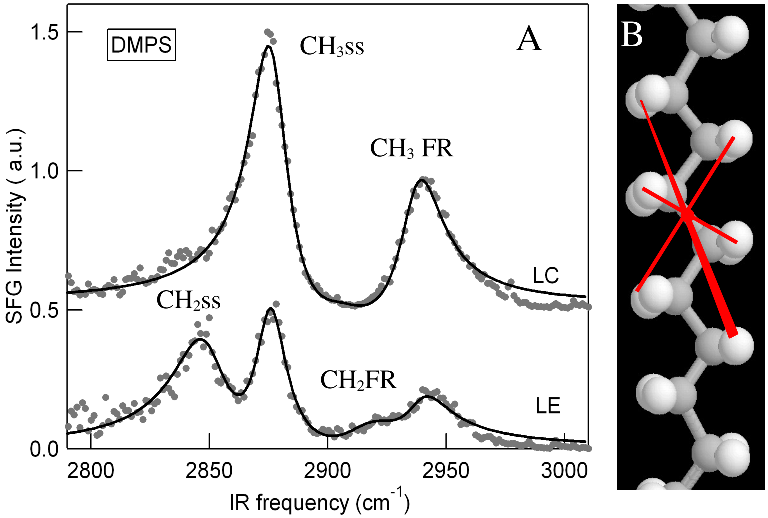

Figure 2.7 A: Typical SFG response in the C-H stretch region for a DMPS monolayer in the expanded (LE) and condensed (LC, offset by 0.5 for clarity.) phase, respectively. The polarization conditions are *ssp*. The positions of methylene symmetric stretch (CH_2 ss), methyl symmetric stretch (CH_3 ss), methylene Fermi Resonance symmetric stretch (CH_2 FR) and methyl Fermi Resonance symmetric stretch (CH_3 FR) are also indicated. Solid lines represent fits to the data, as described in the text. B: Illustration of the ordered lipid tail in the LC phase. The red lines illustrate the center of inversion that is present in the center of the bond between the carbon atoms: the lines connect the CH_2 group on the left side of the tail with its pair group on the right side for which the SFG signal will cancel with each other.

mode	A_n (LE)	A_n (LC)	ω_n	Γ_n
CH_2ss	-7	0	2850	28
CH_3ss	-5	-10	2875	16
CH_2FR	-4	0	2917	22
CH_3FR	-3	-8	2935	22
CH_3as	1.3	2	2960	20

Table 2.1 The fitting parameters used to fit the spectra of a DMPS monolayer on LE and LC phase, with the nonresonant amplitude, A_0 = 0.1 and nonresonant phase, φ_{NR} = -1.4, respectively.

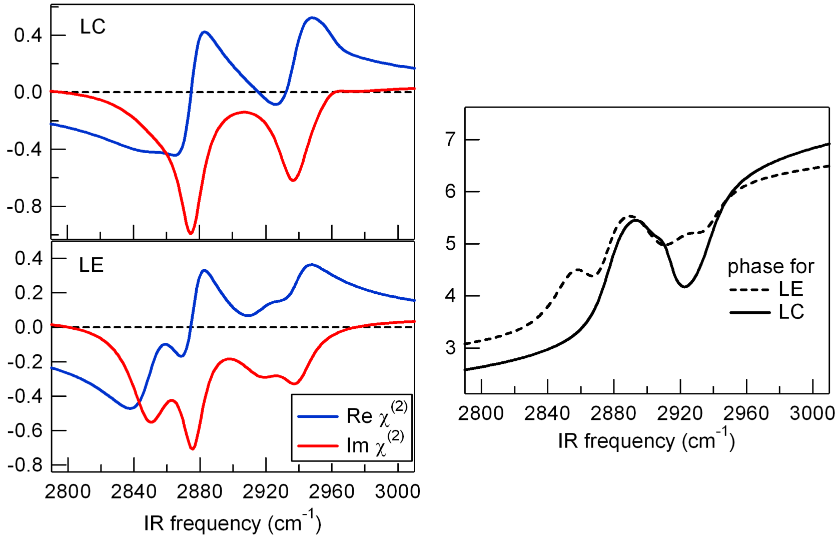

Figure 2.8 The real (blue) and imaginary (red) parts, and the phase (black) of $\chi^{(2)}$ obtained from the corresponding fit to the spectra in Figure 2.7.

The CH_2 symmetric and CH_2 Fermi resonance symmetric stretch frequencies are found around 2850 and 2920 cm^{-1}. The results of the spectral fit are listed in Table 2.1. The amplitudes of the CH_3 symmetric stretch is chosen to be negative, corresponding to an orientation of the transition dipole moment of this mode pointing away from the surface [10, 11].

When the monolayer is compressed to a LC phase, the CH_2 modes disappear, as a local symmetry point appears along the lipid tail when the chain is in its ‘all-trans’ C-C bond conformation (see Figure 2.7 B). The disappearance of the methylene modes proves the surface specificity of the SFG technique. At the same time, the amplitudes of the CH_3 modes increase due to the alignment of the dipole moments at the surface when the lipid tails are ordered. By determining the amplitudes of the CH_2 and CH_3 modes, we can find the local lipid organization at the surface, in a non-invasive way. The ratio of CH_3 and CH_2 symmetric stretched amplitudes can be used therefore as an order parameter to quantify the monolayer order. This ratio was used in chapter 4 to monitor the changes in lipid organization when the water subphase contained mono- or divalent ions.

2.5.3 SFG response in the O-D and C-H stretch region

In the following, the typical vibrational response in both the O-D and the C-H stretch regions is analyzed. In the O-D region, two main peaks are observed, centered at $\nu_1 = 2380$ and $\nu_2 = 2470$ cm^{-1}, respectively (Figure 2.9). As explained in chapter 5, these two peaks are assigned to the O-D symmetric stretch split by the Fermi Resonance with the overtone of the bending mode [12].

mode	A_n	ω_n	Γ_n
OD (ν_1)	-11	2380	100
OD (ν_2)	-42	2470	210
CH_2ss	-4	2845	47
CH_3ss	-11	2876	14
CH_2as	4	2885	20
CH_3FR	-9	2935	15
CH_3as	10	2960	25

Table 2.2 The fitting parameters used to fit the spectra of a DMPS monolayer that includes both O-D and C-H stretch region. The nonresonant amplitude and phase were found to be $A_0 = 0.2$ and $\varphi_{NR} = -1.4$, respectively.

In the experiments where both C-H and O-D stretch were probed, the VIS beam was shaped with only one etalon, such that the resulting bandwidth was larger (FWHM = 25 cm^{-1}), as explained in section 2.4.3. To account therefore for the instrument response, originating from the large bandwidth of the VIS beam, we convolve the expression from equation (2.2) with a Gaussian function $G_n(\omega)$:

$$I_{SFG} \propto \left| \left(\chi^{(2)}_{NR} + \sum_n [A_n / (\omega_{IR} - \omega_n + i\Gamma_n)] \right) * G_n(\omega) \right|^2 \qquad (2.4)$$

The real, imaginary parts and the phase of $\chi^{(2)}$ obtained from the fit using equation (2.4) are displayed in Figure 2.10. Our results show once more that the amplitudes of the CH_3 symmetric mode are negative (see Table 2.2); these can be

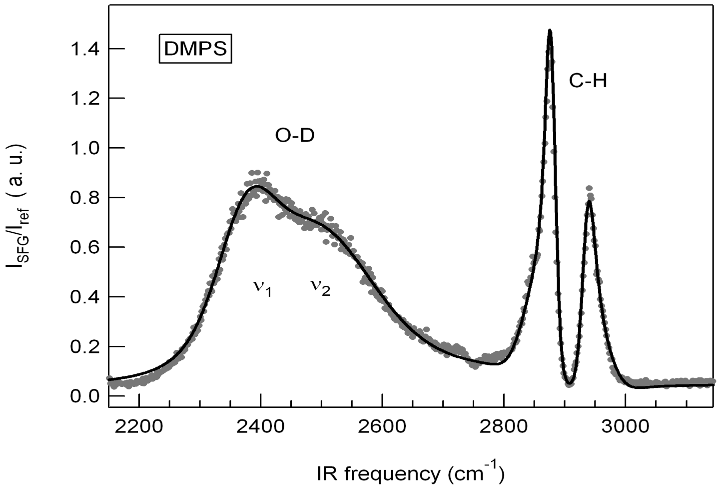

Figure 2.9 Typical SFG response in the O-D and C-H stretch region for a DMPS monolayer at π = 25 mN/m. During the experiment the IR frequency was continuously swung between 2050 and 3250 cm^{-1}. The polarization condition is *ssp*. The two prominent peaks in the O-D stretch region are labeled as ν_1 and ν_2. Solid lines represent fits to the data, as described in the text.

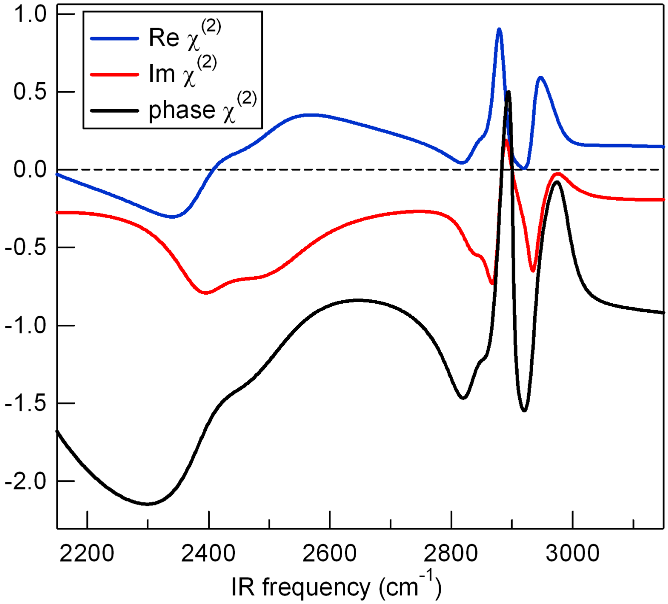

Figure 2.10 The real (blue) and imaginary (red) parts, and the phase (black) of $\chi^{(2)}$ obtained from the corresponding fit to the spectrum in Figure 2.9.

used as a reference for choosing the nonresonant phase, ϕ_{NR}. As can be seen from equations (2.2) and (2.4), a π shift in ϕ_{NR} and a change in the sign of the resonant amplitude will return the same $|\chi^{(2)}|^2$ values.

In such case, the fitting routine is not unique in determining the sign of the resonant amplitudes (see also chapter 6); however, the CH_3 symmetric mode should always have negative amplitudes and they can be used as a reference for determining the sign of the other resonances in the spectra. The spectrum in Figure 2.9 is one of the examples: as the amplitudes of the C-H modes known, the sign of the resonances in the O-D stretch modes can be determined, and therefore the water molecular orientation at the interface. We find that the water molecules orient with their dipole moments pointing away from the surface (e.g. with their oxygens towards the surface), as the sign of the ν_1 and ν_2 are the same as the CH_3 symmetric stretch. Using this procedure, we can determine the water orientation at different interfaces, as shown in chapter 6 and 7.

The fitting routine described above are used throughout the thesis for spectra measured in the C-H stretch region (as in Figure 2.7), as well as for spectra measured in both C-H and O-D stretch region (as in Figure 2.9).

References

[1] V. M. Kaganer, H. Mohwald, and P. Dutta, Rev. Mod. Phys. **71**, 779 (1999).

[2] G. W. H. Wurpel, M. Sovago, and M. Bonn, J.Am. Chem. Soc. **129**, 8420 (2007).

[3] J. Mattai, H. Hauser, R. A. Demel, et al., Biochemistry **28**, 2322 (1989).

[4] D. McLoughlin, R. Dias, B. Lindman, et al., Langmuir **21**, 1900 (2005).

[5] H. A. Santos, V. Garcia-Morales, R. J. Roozeman, et al., Langmuir **21**, 5475 (2005).

[6] V. L. Shapovalov, Thin Solid Films **327**, 599 (1998).

[7] M. Sovago, G. W. H. Wurpel, M. Smits, et al., J. Am. Chem. Soc. **129**, 11079 (2007).

[8] P. Wydro and K. Hauc-Wydro, J. Phys. Chem. B **111**, 2485 (2007).

[9] X. Zhuang, P. B. Miranda, D. Kim, et al., Phys. Rev. B **59**, 12632 (1999).

[10] M. Oh-e, A. I. Lvovsky, X. Wei, et al., J. Chem. Phys. **113**, 8827 (2000).

[11] S. Nihonyanagi, S. Yamaguchi, and T. Tahara, J. Chem. Phys. **in press** (2009).

[12] M. Sovago, R. K. Campen, G. W. H. Wurpel, et al., Phys. Rev. Lett. **100**, 173901 (2008).

Chapter 3

Monolayer relaxation study: a polarization-resolved sum-frequency generation approach

A novel implementation of broad-bandwidth Sum Frequency Generation (SFG) spectroscopy is presented, which allows for the simultaneous recording of SFG spectra with different polarization combinations of the SFG, visible and infrared beams. This method is particularly advantageous for studies in which surface properties are time-dependent, such as kinetic studies. The technique is illustrated by a study that mimics the lung surfactant relaxation during the breathing cycle: a lipid monolayer is compressed from a disordered phase to an ordered phase, and then the monolayer is allowed to relax to its initial state. During the relaxation process, the lipid tails are first changing their orientation on a time scale of tens of seconds, and sequentially the lipids respread to form a homogeneous disordered phase.

3.1 Introduction

In the narrow-band Sum-Frequency Generation (SFG) technique, the VIS and the IR pulses used to generate the sum-frequency response light have picosecond time duration. To record an SFG spectrum in such a case, the IR frequency needs to be scanned over the whole frequency range that one needs to probe. In broad-band SFG, as introduced in chapter 2 of this thesis, a femtosecond IR pulse is used to cover a window of frequencies of ~ 200 cm^{-1}. The advantage of this approach is that the sample response is recorded with every individual laser pulse at all frequencies. Therefore, all data points in the SFG spectrum are measured under the same conditions. This is not the case in narrow-band SFG, where each point of the spectrum originates from distinct measurements, under potentially different conditions. This advantage of the broad-band SFG can be used to perform kinetic measurements on, for example, surfaces that change in time [1-5].

However, distinct measurements are still required for the cases where the polarization of the two incoming beams needs to be changed. In these cases, the SFG intensity is recorded under different polarization conditions in order to determine the orientation of a specific molecular group at the surface [6]. However, this requires comparison of at least two SFG spectra that have been measured under different experimental conditions. Alternative techniques like the Polarization Null Angle (PNA) method [7, 8] to improve the accuracy of the determination of orientational parameters all suffer from the fact that data is obtained from different measurements.

Here an extension of broad-bandwidth SFG which enables the simultaneous measurement of two polarization combinations is presented. This technique circumvents the problem of laser instabilities and changes in the sample over time and further facilitates the SFG measurements, in particular the determination of changes in molecular orientation, when using SFG in kinetic mode [1-5]. The advantage of (near) simultaneous determination of the different polarization contributions to the signal has been shown for various linear spectroscopic techniques, like polarization modulated infrared reflection absorption spectroscopy [9-11] and T-format fluorescence anisotropy spectroscopy [12].

We demonstrate here the polarization resolved method by a kinetic study of lung surfactant compression and relaxation, which mimics the respiration cycle [13]. The main component of mammalian lung surfactant is the lipid dipalmitoylphosphatidylcholine (DPPC). Its function is to lower the surface tension at the alveolar surface during exhalation, reducing the work required during the respiration cycle. Deficiency of the lung surfactant, particularly with premature infants, results in the (acute) respiratory distress syndrome. A recent study has investigated the collapse of DPPC monolayers by compressing the monolayer beyond its collapsing point [14, 15]. Also several studies on DPPC monolayers using SFG are available, mainly probing the CH_2 and CH_3 groups in the chain [16-18], but also recently the CH_2 and CH_3 groups in the headgroup as well as the phosphate group [19]. In the study presented in this chapter, a monolayer of neat DPPC on a water subphase is compressed from low surface pressure to high surface pressure, close to the collapsing point. Subsequently, the monolayer is decompressed and allowed to relax. During the relaxation process, the molecular response is monitored in real-time by measuring the SFG spectra of the CH_2 and CH_3 groups of the lipid tails.

Our approach relies on the use of incident and generated fields polarized at 45°, in between *s*- and *p*-polarized. Considering the possible polarization combinations, it is evident that, when one of the incident IR or VIS fields is polarized at 45° (termed here as 'M-polarized'), SFG with both *s* and *p* polarization is emitted. As evident from Table 3.1, when the IR beam is M-polarized, SFG can be generated in *ppp*- and *sps*-mode, when VIS is *p*-polarized (and *ssp* and *pss* when the VIS beam is *s*-polarized). The same procedure can be applied when the VIS beam is M polarized. Two polarization combinations were measured simultaneously in this study, namely *ssp* and *ppp*.

SFG	VIS	IR
p(pp) s(ps)	p	M = p/s
s(sp) p(ss)	s	
p(pp) s(sp)	M = p/s	p
s(ps) p(ss)		s

Table 3.1 The possible polarization combinations when one of the incoming beams is M-polarized. There are only four polarization combinations for which SFG is generated, namely ppp, sps, ssp, and pss of the SFG, VIS and IR fields, respectively.

3.2 Experimental section

The SFG setup was described in detail in chapter 2 of this thesis. In the experiments described here, only a change of the detection part was made in order to perform polarization-resolved experiments (see Figure 3.1). The generated SFG signal that has both *s* and *p* polarizations, was separated using a beam-displacing prism (Melles Griot): the *s*-polarized light propagates unaffected, whereas the *p*-polarized light is displaced vertically by 4 mm. The SFG fields were spectrally dispersed using an imaging monochromator and were detected using an intensified Charge Coupled Device camera (iCCD, Roper Scientific). Due to the displacing prism, the two contributions with orthogonal polarization were imaged at different heights on the iCCD camera and could be recorded simultaneously. The *s*-polarized signal will appear at the top of the iCCD, while the *p*-polarized signal at the bottom (see Figure 3.1). Because of their collinear propagation from the sample, the two separated SFG beams cannot be simply focused onto the vertical entrance slit of the monochromator

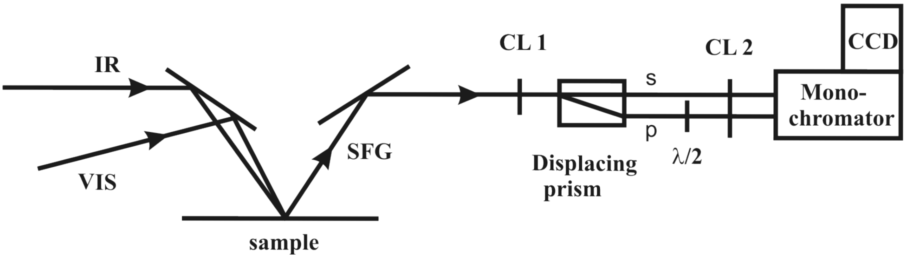

Figure 3.1 Schematic representation of the detection part of the SFG setup. For the detailed description of the whole setup, see chapter 2. In the polarization resolved method, the SFG beam is focused in the horizontal plane by a cylindrical lens (CL1). A displacing prism is used to separate the different polarizations of the SFG signal: the *s*-polarized SFG signal travels unaffected, while the *p*-polarized SFG signal is displaced in the vertical plane, and then rotated to *s*-polarization by an additional λ/2-plate, for improving the detection efficiency. Finally, the signal beams are focused on to the slit of the spectrometer using a second cylindrical lens (CL2). The signal is spectrally analyzed using a monochromator, coupled to an iCCD camera.

using a spherical lens, as they would be focused on the same spot. Instead, the light was focused onto the slit of the monochromator in the horizontal plane using an $f = 50$ cm cylindrical lens (CL1), placed in front of the beam-displacing prism, and in the vertical plane by an $f = 5$ cm cylindrical lens (CL2), placed in front of the slit. Additionally, we compensated for the different monochromator detection efficiency for *s*- and *p*-polarized light, by adding a λ/2-plate to the lower of the two beams to convert the *p*-polarized signal beam into *s*-polarized. The detection efficiency in this channel is enhanced in this way by approximately a factor of 2. As such, no additional correction for differences in detection efficiency for the two channels is necessary. The SFG spectra recorded during the relaxation process were acquired for 20 s each.

The lipid monolayer of *L*-1,2-Dipalmitoyl-*sn*-glycerol-3-phosphocholine (DPPC) was prepared as described in chapter 2. First, a pressure-area (π-A) compression isotherm was measured (Figure 3.2). The isotherm reveals the phase behavior of DPPC, which is similar to that of DMPS (see for more details chapters 2 and 4). During the monolayer relaxation experiments, the monolayer was prepared in the liquid expanded (LE) phase at a surface pressure of 4 mN/m (corresponding to 75 Å^2/molecule), as indicated in Figure 3.2 by pressure π_1. Next, the sample is compressed using only one barrier up to 35 mN/m (π_2 in Figure 3.2) in the liquid condensed (LC) phase and then decompressed by gently but quickly moving the compression barrier to its original position. The moment the barrier has returned to its original position is defined as $t = 0$. The dashed arrow in Figure 3.2 indicates the time-dependent pressure π_3 during the relaxation process starting from pressure π_2 back to pressure π_1.

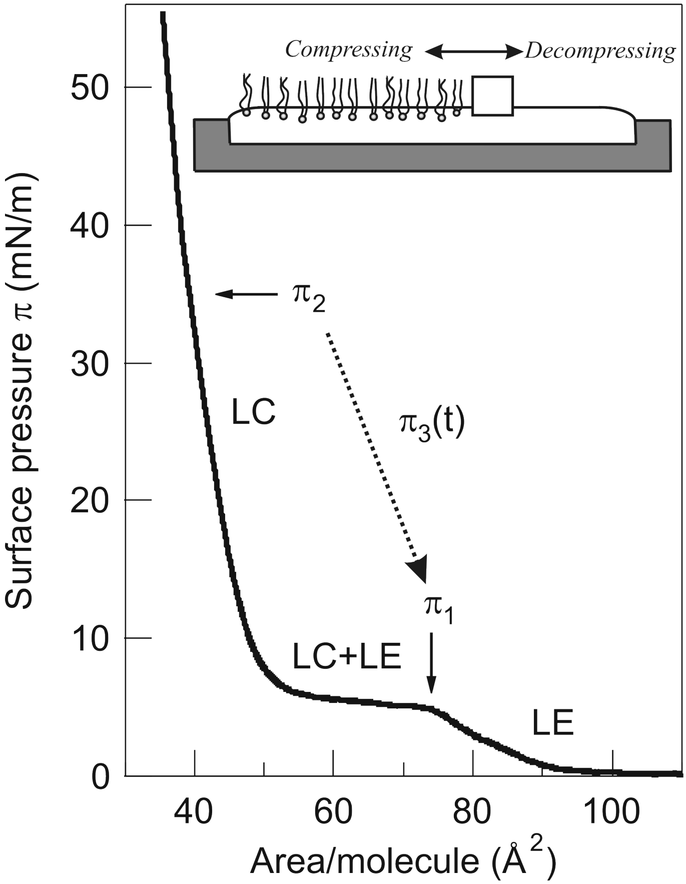

Figure 3.2 DPPC compression isotherm, showing the different lipid phases: liquid expanded (LE), liquid condensed (LC) and the coexistence region between the two phases, LC+LE. During the monolayer relaxation experiments presented here, the lipid monolayer is prepared at an initial surface pressure π_1 in the LE phase. Then the monolayer is compressed to a high surface pressure π_2 in the LC phase. As the barrier is moved to its initial position, the monolayer will relax to low surface pressure, shown by the dotted arrow. The pressure during relaxation is indicated as $\pi_3(t)$. The schematic of the Langmuir trough used for the monolayer relaxation is shown schematically in the inset.

3.3 Results and discussion

3.3.1 The surface symmetry of lipid monolayers

The polarization-resolved broad-bandwidth SFG method relies on the generation of SFG with orthogonal polarization when one of the incoming beams is M-polarized. In the case of surfaces with symmetry around the surface normal, it can be shown theoretically that indeed the two contributions to the SFG signal have orthogonal polarization, but in the general case for arbitrary symmetry, this is not necessarily true. It is well known that DPPC forms an isotropic monolayer, symmetric around the surface normal. To confirm its symmetry, we performed an experiment using the polarization-resolved SFG approach, where the SFG spectra are measured in a conventional way, with no M-polarized beams. If the surface is indeed isotropic, each polarization combination of VIS and IR beams should result in an SFG beam of either *s*- or *p*- polarized light, but not both. For example, *s*-polarized VIS and *p*-polarized IR beams should give rise to a *s*-polarized SFG beam, and not *p*-polarized. Therefore, the full image recorded by the CCD camera should only contain one spectrum instead of two. In the left panel of Figure 3.3, the top image shows the SFG signal of a saturated DPPC monolayer, recorded with the VIS and IR polarized *s* and *p*, respectively. The generated SFG signal with *s* polarization is visible in the top part of the image, as expected.

The same is true for the case where both VIS and IR beams are *p*-polarized, as shown in the bottom part of Figure 3.3. Here, the main signal is present in the lower part of the image, corresponding to *p*-polarized SFG. This clearly confirms that the surface is isotropic as anticipated. The small signals present at the bottom part of the image for *ssp* polarization and at the top part for *ppp* polarization are less than 10 % of the main contribution. In principle, these signals could be due to a contribution from a non-isotropic surface (or chiral molecules), but additional measurements using a gold substrate as a reference indicate that these signals originate from slight impurities in the polarizations of the incoming beams.

As we will show in the next section, by using an M-polarized beam, we can measure simultaneously two SFG spectra with different polarization combinations. Namely, when the IR beam is M-polarized, *ppp* and *sps* spectra are measured together when VIS beam is *p*-polarized, and *ssp* and *pss* spectra when VIS is *s*-polarized. When the VIS beam is chosen to be M-polarized, then *ppp* and *ssp* spectra are recorded simultaneously for *p*-polarized IR beam and *sps* and *pss* spectra for *s*-polarized IR beam (see Table 3.1).

3.3.2 The kinetics of lipid monolayer relaxation

The kinetics of the monolayer relaxation are followed in real time by recording simultaneously *ppp* and *ssp* spectra in the C-H stretch region. Figure 3.4 displays the raw CCD image of the SFG signal from the monolayer before compression (π_1 in Figure 3.2), with the *ssp* contributions of the SFG signal in the top part of the image, and the *ppp* contribution in the bottom part. The SFG spectra contain resonances from both CH_2 and CH_3 stretch vibrations, as explained in detail in chapter 2. In the *ssp* spectrum, the most intense peak is the CH_3 symmetric stretch Fermi Resonance (CH_3FR) centered at 2935 cm^{-1}, whereas in the *ppp* spectrum the main peak is the CH_3 antisymmetric stretch (CH_3as), centered at 2960 cm^{-1}.

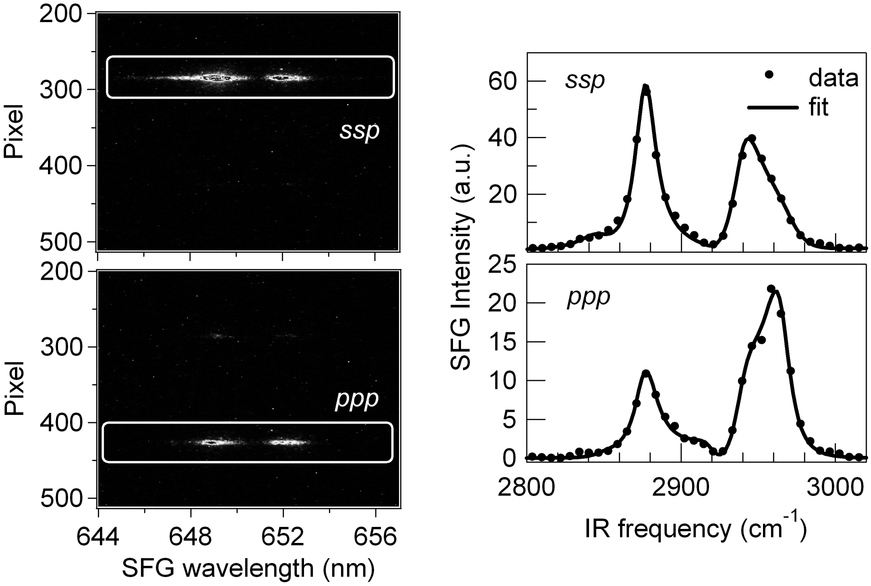

Figure 3.3 The raw CCD image recorded with *s* (top) and *p* (bottom) polarized VIS light is shown for a DPPC monolayer at the surface pressure π_2 = 35 mN/m. The presence of only one polarization component in each image indicates that the surface of the sample is isotropic. Next to the images, the corresponding spectra are shown (circles) by integrating the image in the vertical direction over the region of interests as indicated. The solid line is a fit to the data using a Lorentzian model.

Next the monolayer is compressed to 35 mN/m (π_2 in Figure 3.2), and then decompressed to its initial state. Immediately after the return of the barrier to its initial position (t = 0), the kinetic measurement is started, recording continuously both the two SFG spectra every 20 seconds for a total of 6 minutes and the surface pressure. After the release of the barrier, the pressure π_3 shows a rapid decrease from pressure π_2 to a value below pressure π_1 (see Figure 3.5). This undershoot of the surface pressure can be explained using the compression isotherm shown in Figure 3.2. After compression, the monolayer is in the LC phase, where the lipids are highly ordered, forming a homogeneous monolayer (as shown by the dark areas in the first cartoon of Figure 3.5). When the barrier is removed, the monolayer falls apart into LC and LE domains (second cartoon in Figure 3.5, where the dark and the light regions represent the lipids in the LC and LE phase, respectively) [20].

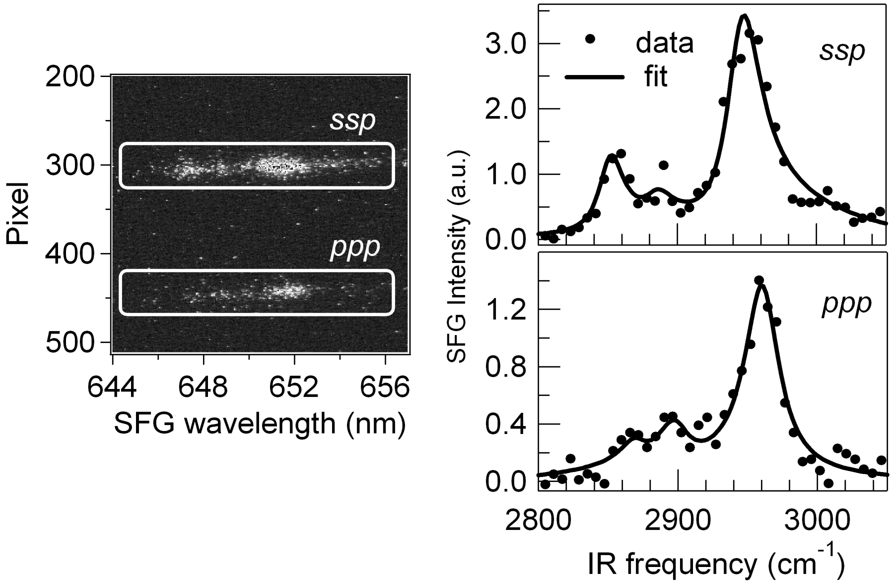

Figure 3.4 The raw image is shown for the polarizations *ssp* (top) and *ppp* (bottom), measured with the polarization resolved method at a surface pressure of 3.7 mN/m. The signal appears at different vertical positions in the same CCD image due to the displacement prism. Next to the image, the corresponding spectra are shown (circles) by integrating the image in the vertical direction over the region of interests as indicated. The solid line is a fit to the data.

The surface pressure measured in this configuration is the average pressure of the large areas with low lipid density and the small areas with high lipid density and, as such, it can be lower than pressure π_l because of the presence of LC domains. As the monolayer is allowed to relax, the LC domains disappear and the system equilibrates to its original state, as seen in Figure 3.5. During this slow process of equilibration, the lipids respread from the dense domains and cover the whole surface evenly (third cartoon in Figure 3.5). The slow component of the relaxation process can be described by a biexponential fit (solid line), with characteristic decay times of 60 and 300 s.

For further understanding of the changes that occur in the monolayer conformation during the relaxation process, the recorded SFG spectra are analyzed. The peak areas in the region 2920-2980 cm^{-1} are obtained as the most useful markers of the spectral changes during monolayer relaxation. Figure 3.5 shows the areas of the peaks as a function of time for the *ssp* and *ppp* spectra, normalized to the initial peak area at pressure π_l. Note that the peak area obtained from the *ppp* spectrum is multiplied by -1 to point out that the amplitudes of the $\mathrm{CH_3}$FR and $\mathrm{CH_3}$as vibrations have opposite signs. The change in the peak areas follows to some extend the surface pressure, with decay times of 70/300 s and 50/300 s for the *ppp* and *ssp* data, respectively.

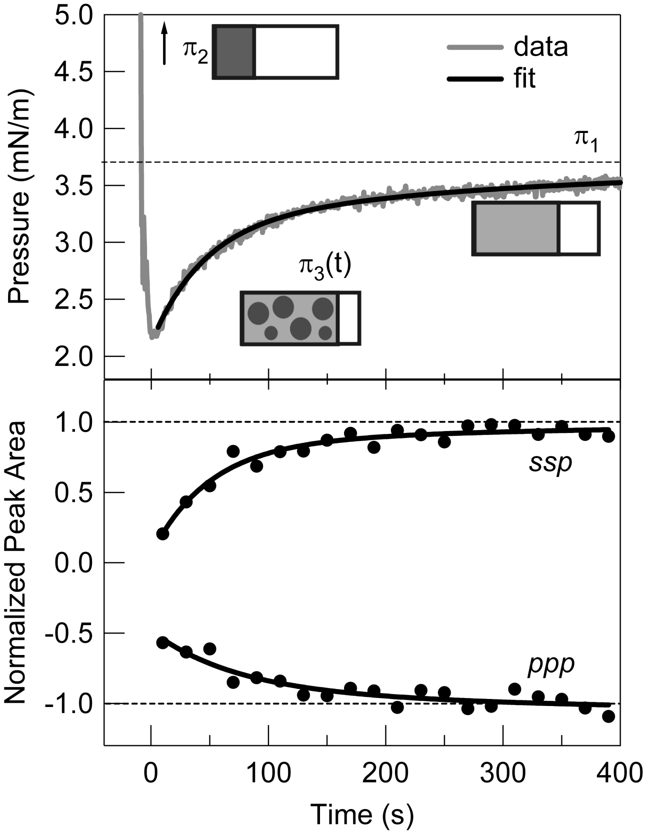

Figure 3.5 Top panel: the surface pressure as a function of time during the monolayer relaxation process. The initial surface pressure π_1, before compression is shown by the horizontal dashed line. The cartoons represent a view of the trough, showing the morphology of the lipid monolayer: dark regions represent the LC domains, and the light regions are the regions with lipids in LE phase. Bottom panel: the amplitudes of $\nu_{as,CH3}$ (*ppp*) and $\nu_{sFR,CH3}$ (*ssp*) as a function of time during the monolayer relaxation. The initial amplitudes are normalized to ±1 (dashed line). The solid lines represent a fit using a biexponential function, as described in the text.

As a result, the monolayer relaxation is governed by two processes: the change in the orientation of the lipid and the respreading of the lipids from the LC domains to the uniform LE domain that covers the entire monolayer. The first process can be explained as follows: the main contribution to the peak areas for *ssp* and *ppp* spectra arises from two perpendicular transition dipoles (CH_3FR and CH_3as). Hence, a change in the ratio of the peak areas *ppp*/*ssp* can qualitatively be interpreted as an orientation change in the terminal CH_3 group of the lipid chains.

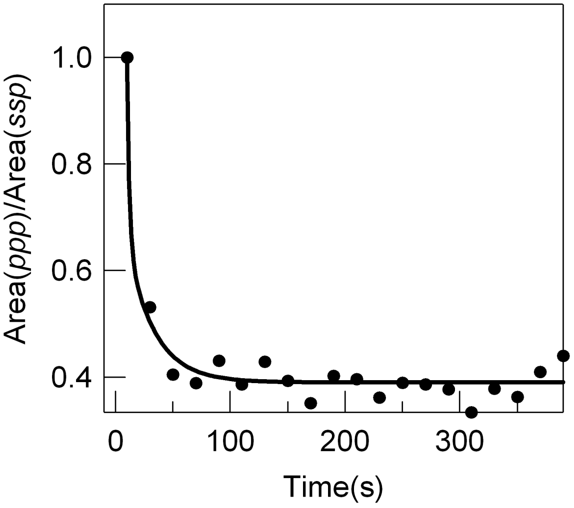

Figure 3.6 The ratio of the peak area *ppp*/*ssp* as a function of time using the values of the peak areas shown in Figure 3.5

Indeed, this ratio shows one fast decay component as a function of time (see Figure 3.6), with a characteristic time of 15 s. This decay time is shorter than the components in the fit of the pressure. The change in the lipid orientation occurs after the release of the barrier and the breakup of the continuous LC phase patches. During the remaining of the monolayer relaxation process, the angles of the chains do not further change, but the lipids respread according to the changes of the peak areas in Figure 3.5.

Further, we present quantitative analyses to determine the lipid orientation in the different stages of the relaxation process. The method to determine the molecular orientation at the surface is described in detail elsewhere [6, 21]. Here, we theoretically calculate the ratio between the antisymmetric CH_3 stretch amplitude in *ppp* spectrum and the symmetric CH_3 stretch amplitude in *ssp* spectrum, $A_{as}(ppp)$ / $A_{ss}(ssp)$, as explained in the Appendix A of this thesis. This ratio is directly correlated with the angle between the transition dipole of the CH_3 group with the surface normal (θ), as shown in Figure 3.7. The amplitude of the CH_3FR is assumed to follow the behavior of CH_3 symmetric stretch (CH_3ss). The observed decrease in the peak ratio *ppp*/*ssp* during the monolayer relaxation indicates that the vertical projection of the component of the dipole moment of the symmetric CH_3 vibration increases. As such, the angle of the lipid tails with the surface normal decreases, indicating a more ordered lipid conformation. Indeed, the theoretical curve of the $A_{as}(ppp)$ / $A_{ss}(ssp)$ ratio shows that the angle θ decreases for smaller ratios. Therefore, we can conclude in correlation with surface pressure measurements that while the pressure increases after the LC domains formation, on a molecular level, the lipid chains relax by reducing their tail angle with respect to the surface. From quantitative analysis using a global fit of the data we find that the ratio

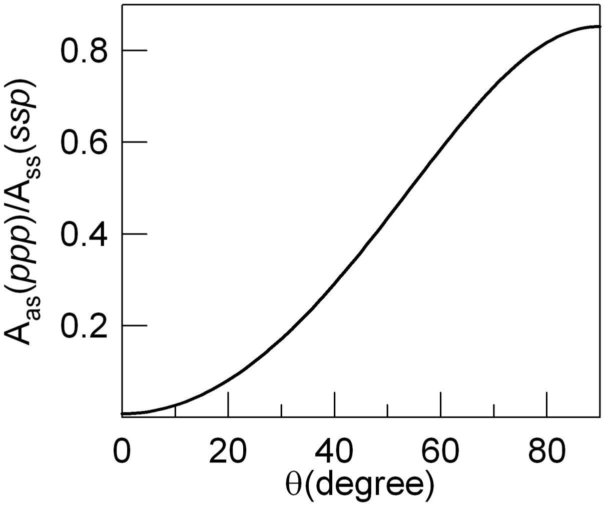

Figure 3.7 The theoretical trend for the ratio of CH_3 vibrational amplitudes $A_{as}(ppp)/A_{ss}(ssp)$ as a function of the angle θ between the symmetric CH_3 dipole moment and the surface normal. This ratio was calculated following the procedure explained in the appendix A of this thesis.

$A_{as}(ppp)$ / $A_{ss}(ssp)$ decreases from a value of 0.81 to 0.75, yielding a change in the angle of the chain from roughly 90° to 70° (see Figure 3.7).

3.4 Conclusions and Outlook

We have presented a novel implementation of broad-bandwidth SFG, which allows simultaneous recording of spectra with different polarization. Our approach circumvents possible problems related to fluctuations in the signal because of instabilities of the laser or changes of the sample in time. As an example of this polarization-resolved technique, we performed a kinetic study of a lipid monolayer during its relaxation process from a compressed phase to an expanded phase. We found that the lipids form first LC domains surrounded by lipids in LE phase and then the lipids respread to form a homogeneous LE monolayer. After the LC domains formation, the order of the lipids increases as the lipids relax back to their initial state.

Finally, we will discuss three further improvements of the polarization-resolved technique that have not been exploited in this study: (1) in this technique either the VIS or the IR beams can be M-polarized. In both situations, the two contributions to the SFG signal can be separated based on the polarization of the SFG beam. When all three distinct polarization combinations have to be obtained (*ssp*, *ppp*, *sps* = *pss*), two independent measurements are still required. By choosing the IR beam instead of the VIS beam to be M-polarized, the *sps* and *pss* spectra are measured in two sequential measurements. The spectra within the first set are measured simultaneously and can be compared directly. The second set contains one spectrum that is equivalent to a spectrum of the first set and can be used to scale the second data set for comparison with the first data set. For the situation where the VIS beam is M-polarized the two equivalent spectra end up in the same data set and hence comparison with the other data set is obscured. (2) The data from kinetic measurements can be improved by combining the polarization-resolved method with time-correlated techniques. The latter approach has been shown for the dilatational properties of DPPC monolayers using the surface pressure response as a function of the frequency of a sinusoidal variation (with period *T*) in surface area [22]. By averaging spectra recorded at different integration times with fixed intervals *T*, the noise in the data presented here can, in principle, be further reduced. (3) If the impurities in the polarization of the VIS and IR beams can be neglected and the separation of the polarization components of the signal is sufficient, the polarization-resolved technique can be used for chiral surfaces to obtain simultaneously the 'normal' and the chiral components of the signal [23]. Hereto, the setup is used in the traditional scheme with pure polarizations. Choosing the polarization of the VIS and IR beams, respectively, *s* and *p*, the normal SFG signal *ssp* and the chiral signal *psp* are measured simultaneously.

References:

[1] F. Hobel, A. Bandara, G. Rupprechter, et al., J. Surf. Sci. **600**, 963 (2006).
[2] J. Liu and J. C. Conboy, Biophys. J. **89**, 2522 (2005).
[3] T. Rasing, T. Stehlin, Y. R. Shen, et al., J. Chem. Phys. **89**, 3386 (1988).
[4] W. G. Roeterdink, O. Berg, and M. Bonn, J. Chem. Phys. **121**, 10174 (2004).
[5] S. Westerberg, C. Wang, and G. A. Somorjai, Surf. Sci. **582**, 137 (2005).
[6] X. Zhuang, P. B. Miranda, D. Kim, et al., Phys. Rev. B **59**, 12632 (1999).
[7] X. Y. Chen, M. L. Clarke, J. Wang, et al., Int. J. Mod. Phys. B **19**, 691 (2005).
[8] J. Wang, X. Y. Chen, M. L. Clarke, et al., Proc. Natl. Acad. Sci. U.S.A. **102**, 4978 (2005).
[9] T. Buffeteau, B. Desbat, and J. M. Turlet, Appl. Spectrosc. **45**, 380 (1991).
[10] I. Estrela-Lopis, G. Brezesinski, and H. Mohwald, Biophys. J. **80**, 749 (2001).
[11] K. Itoh and H. Oguri, Langmuir **22**, 9208 (2006).
[12] J. R. Lakowicz, *Principles of Fluorescence Spectroscopy*; Kluwer Academic: New York (1999).
[13] J. Goerke, J. Biochim. Biophys. Acta **1408**, 79 (1998).
[14] K. B. Chen, C. H. Chang, Y. M. Yang, et al., Colloids Surf. A **216**, 45 (2003).
[15] A. Gopal and K. Y. C. Lee, J. Phys. Chem. B **110**, 22079 (2006).
[16] M. Bonn, S. Roke, O. Berg, et al., J. Phys. Chem. B **108**, 19083 (2004).
[17] S. Roke, J. Schins, M. Muller, et al., Phys. Rev. Lett. **90** (2003).
[18] M. R. Watry, T. L. Tarbuck, and G. I. Richmond, J. Phys. Chem. B **107**, 512 (2003).
[19] G. Ma and H. C. Allen, Langmuir **22**, 5341 (2006).
[20] Y. F. Hu, K. Meleson, and J. Israelachvili, Biophys. J. **91**, 444 (2006).

[21] H. F. Wang, W. Gan, R. Lu, et al., Int. Rev. Phys. Chem. **24**, 191 (2005).
[22] P. Saulnier, F. Boury, A. Malzert, et al., Langmuir **17**, 8104 (2001).
[23] N. Ji, V. Ostroverkhov, M. Belkin, et al., J. Am. Chem. Soc. **128**, 8845 (2006).

Chapter 4

Calcium and sodium ion effects on lipid monolayers

In this chapter, we investigate the effects of sodium and calcium ions on the organization and molecular properties of zwitterionic and anionic phospholipids monolayers on water. These systems are investigated using vibrational sum-frequency generation in conjunction with surface pressure measurements and fluorescence microscopy. Sodium ions only subtly affect the monolayer structure, while the effect of calcium is large and depends strongly on the surface pressure. At low surface pressures (~5 mN/m), the presence of Ca^{2+} results in the unexpected appearance of ordered domains. For pressures between ~5 and ~25 mN/m, Ca^{2+} ions induce molecular disorder in the monolayer. For pressures exceeding 25 mN/m, calcium cations expand the monolayer, while simultaneously ordering the lipid chains. Interestingly, these effects are similar for both zwitterionic lipids and negatively charged lipids. In both vibrational sum-frequency generation and surface tension measurements, the molecular signature of the association of Ca^{2+} with the lipids is evident from Ca^{2+}- induced changes in the signals corresponding to area changes of 4 Å^2/lipid – precisely the surface area of a Ca^{2+} ion, with evidence for a change in lipid:Ca^{2+} complexation at high pressures.

4.1 Introduction

The cell's plasma membrane consists of many different phospholipids that are asymmetrically distributed over the two bilayer leaflets. The cytosolic leaflet is enriched in anionic phosphatidylserine (PS) phospholipids, whereas the outer cellular leaflet contains mostly neutral, zwitterionic lipids. The properties of membrane lipids depend strongly on the environmental conditions such as pH and ionic strength. The interactions between membrane lipids and ions – the subject of this study – play an important role in many biological processes, such as membrane fusion, enzyme regulation and signal transduction [1-4]. Due to its negative charge, PS phospholipids attract cations, such as sodium and calcium. This can be explained by the Gouy-Chapman theory of the electric double layer, which predicts a local increase in ion concentration near the negatively charged surface [5]. The interaction between metal ions and the headgroups of zwitterionic phosphatidylcholine (PC) lipids on the other hand is expected to be relatively weak compared with PS. However, the binding constants of ions to PC and PS were found to be similar, after correcting for the differences in electric surface potential [6], showing that the ion-lipid interaction is purely electrostatic. Moreover, small changes in the PC headgroup orientation can significantly alter the electrical properties of the membrane surface [7, 8].

Apart from a fundamental interest, the binding of cations to PC membranes has received special attention for more practical applications [9, 10]. Recently, it was shown that the interaction between DNA and zwitterionic lipids is strongly enhanced by electrostatic interactions in the presence of Ca^{2+} [9, 10]. Therefore, PC lipid-calcium complexes might serve as suitable vectors for DNA transfection, as zwitterionic lipids are nontoxic and biocompatible - in contrast to most cationic lipids.

Most experimental studies to date have aimed mainly at quantifying intrinsic binding constants between ions and lipids and at the characterization of membrane surface potentials. Apart from molecular dynamics (MD) studies [11-16], insights into the molecular details of the interaction between lipids and ions have remained limited. MD simulations have shown that sodium ions bind to the PC bilayers specifically by interacting with phosphodiester oxygens [15]; upon deeper penetration the ions may coordinate with the carbonyl groups [11]. Divalent cations, such as calcium, on the other hand, do not penetrate so deeply into the anionic PS bilayers, being localized in a narrow region around the phosphate group [16]. When cations bind to the membrane, the lipid headgroups have been suggested to undergo a conformational change followed by an increase in the lipid tail order [11, 15, 16].

Despite intensive efforts using MD simulations, there are still some controversial issues [12-14], originating partially from different simulation times, and presumably the choice of potentials in the different simulations. Moreover, the experimental reports to date are limited to one specific lipid density, i.e. a single area per molecule. Experimental investigations of ion-lipid interactions - in particular at various lipid densities - is therefore desirable, to complement existing theoretical efforts. We address in this chapter the interaction between PC and PS lipids and mono- and divalent cations for different lipid densities and phases. In lipid monolayers at the air-water interface, we study the formation of ion-phospholipid complexes and possible ion-induced lipid re-organization in single composition membranes over a range of lipid densities.

The cation-lipid monolayer systems were investigated using a combination of three complementary techniques that provide information on different length scales: surface pressure measurements, fluorescence microscopy and vibrational sum-frequency generation (VSFG) spectroscopy. The surface pressure-versus-area isotherms provide insights into the phase behavior of the entire monolayer at the macroscopic level. With fluorescence microscopy [17-19] lipid domains can be visualized with ~ 500 nm resolution, while VSFG provides information on the molecular orientation and conformation of the lipids [20-24] , albeit averaged over a probing area of ~ 10^{-2} mm^2. Note that SFG is most sensitive to ordered domains, as these provide a significantly larger signal than disordered regions, owing to the increased symmetry upon ordering.

In order to observe the subtle effects of cations on the monolayer organization, relatively high (1 M) concentrations of cations are used. Previous studies have indicated that such high concentrations are required to obtain a significant effect of the interaction of ions with the majority of lipid molecules [25, 26]. Although we report here results for 1 M concentrations, control experiments indicate that the effects reported here affect the majority of lipids at ion concentrations above 50 mM (data not shown).

Cation-lipid interactions are investigated for both the zwitterionic lipid *L*-1,2-Dipalmitoyl-*sn*-glycerol-3-phosphocholine (DPPC) and the negatively charged lipid *L*-1,2-Dimyristoyl-*sn*-glycerol-3-phosphoserine (DMPS). The structures of the lipids are shown in Figure 4.1. To account for the possible changes in the headgroup region upon calcium binding, we have performed experiments on DPPC monolayers, where the lipid tails and both the tails and the choline group of the headgroups are deuterated (d62-DPPC and d75-DPPC, respectively). DMPS and DPPC monolayers exhibit very similar phase behavior, both displaying distinct coexistence regions [27]. Both DPPC and DMPS have saturated alkyl chains, with slightly different lengths of the hydrocarbon chains. As such, these two different types of lipids present good model systems where cation-lipid interactions can be followed through different phases, and the effect of the lipid headgroup charge can be revealed.

The ion-lipid interactions for DPPC and DMPS monolayers can be meaningfully compared, for the following reasons. The binding constant for calcium with neutral lipids, has been estimated to be $12\ M^{-1} < K < 20\ M^{-1}$ [6]. Thus, on a 1 M $CaCl_2$ solution, more than 90% of the DPPC lipids will be bound to calcium. On DMPS, one needs to account for the negative surface charge, which will attract the cations. However, since for the neutral monolayer already nearly all surface sites are bound, this will not significantly change the fraction of bound lipids. Thus, at high electrolyte concentration (1 M) DPPC and DMPS can be directly compared.

We find that Na^+ does not greatly affect the DPPC monolayers, while calcium perturbs the lipid organization significantly. Surprisingly, the effect of calcium on lipid organization (i.e. inducing order or disorder) depends strongly on surface

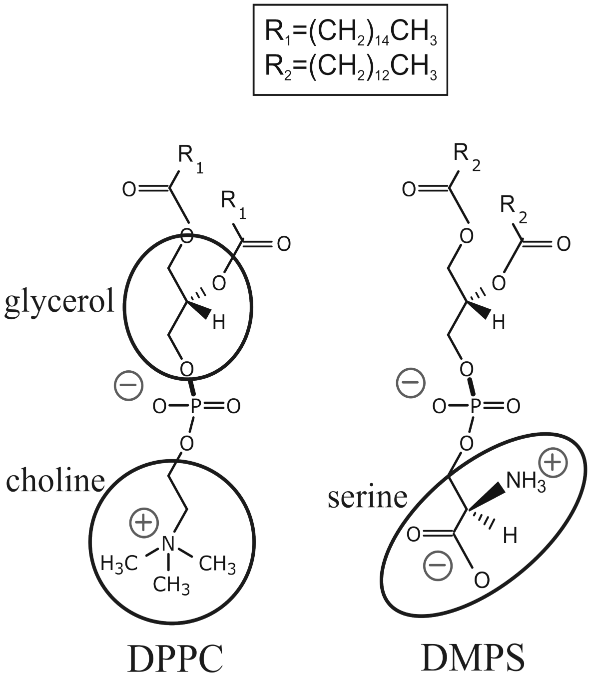

Figure 4.1 The chemical structures of DPPC and DMPS. The glycerol, the choline and the serine groups present in the headgroup region are indicated by the circles.

pressure, π. At low surface pressures (π ~ 5 mN/m), the presence of Ca^{2+} triggers the occurrence of ordered domains; at intermediate pressures Ca^{2+} tends to weakly disorder the monolayer, and at high pressures (π > 20 mN/m) substantial order is induced in the lipid tails through interactions with the headgroup.

These effects are similar for both DPPC and DMPS, which suggests that the Ca^{2+} ion interacts with the same headgroup moiety, most likely the phosphate group (see Figure 4.1). Calcium and phosphate are known to form strong ion pairs in water [28] and the strength of this interaction is likely to be increased in the lipid headgroup region where the dielectric permittivity of the surrounding is reduced. This does not rule out any interactions of Ca^{2+} with the negative charge on the serine group of DMPS, but if this occurs it has no significant influence on the ordering of the lipid tails.

Furthermore, we probe specifically the head group by isotopic substitution of the alkyl chains, so that the alkyl chain C-D stretch vibrations are shifted out of the spectral window of the SFG experiments. We find no significant differences between SFG spectra of d62-DPPC (with deuterated tails) and d75-DPPC (choline group deuterated as well), indicating that the signal arises only from the glycerol group. With calcium ions present in the subphase, the SFG signal did not change significantly, suggesting that the ions do not change the conformation of the DPPC headgroup upon binding.

4.2 Experimental details

The experimental setups and the lipid monolayers preparation are described in detail in chapter 2. Briefly, a commercial Langmuir trough (Kibron Inc, Finland) was used to compress the lipid monolayers at a compression rate of 5 Å^2/chain/min. With this setup the surface pressure of the monolayers can be controlled between 0-40 mN/m. The lipid monolayers were prepared on either a pure water subphase or on a salt solution of 1 M concentration. For the pure water subphase, Millipore water (18.2 MΩ cm resistivity, pH~6) was used for the DPPC monolayers, while for the DMPS monolayers we used Tris buffer (10 mM, pH = 7.1). The fluorescence images were acquired with an exposure of 30 ms using an Electron Multiplier CCD camera (Hamamatsu, Japan). The compression rate of the barriers was 2 Å^2/chain/min. Lipids were doped with 5 mol% fluorescent probe (Rhodamine-PE). Experiments with 1 mol% fluorescent probe revealed identical images with substantially lower contrast. The fluorescence probe partitions into the LE phase, therefore this phase will be seen as brighter regions in the fluorescence images. For sum-frequency generation measurements, DMPS was prepared on D_2O to avoid interference of O-H stretch vibrations with the C-H stretch vibrations. This interference is small for DPPC, as the SFG signal in the O-H stretch vibrations is a factor of 2 lower. The IR wavelength was centered around 2900 cm^{-1} such that the methylene (CH_2) and methyl (CH_3) groups from the lipid tail are within the IR bandwidth. The VSFG spectra were recorded under s-polarized VSFG, s-polarized VIS, and p-polarized IR conditions.

The VSFG spectra obtained are fitted using a Lorentzian model, as described in chapter 2, equation 2.1. This equation was used to globally fit the VSFG spectra, where only the peak amplitudes were allowed to vary, and the central frequency and the line width of every peak were kept fixed as the surface pressure was modified.

4.3 Results and Discussions

First, compression isotherms obtained from the surface pressure measurements are presented, revealing macroscopic differences between lipid monolayers on water, sodium and calcium solutions. Then we visualize the domain formation using fluorescence microscopy along the compression isotherm and we follow how the domains change when Ca^{2+} ions bind to the monolayer. Finally, VSFG is employed to elucidate the cation-lipid interaction at the molecular level.

4.3.1 Compression isotherms

Langmuir isotherms for DPPC and DMPS monolayers on different subphases (neat water, 1 M NaCl and 1 M $CaCl_2$ solution) are shown in Figure 4.2. For the 1 M NaCl and 1 M $CaCl_2$ solutions used here, the concentration of chloride ions in the subphase differs. As the coordination of the chloride anions with the phospholipids is expected to be weak [15], possible effects due to the difference in chloride

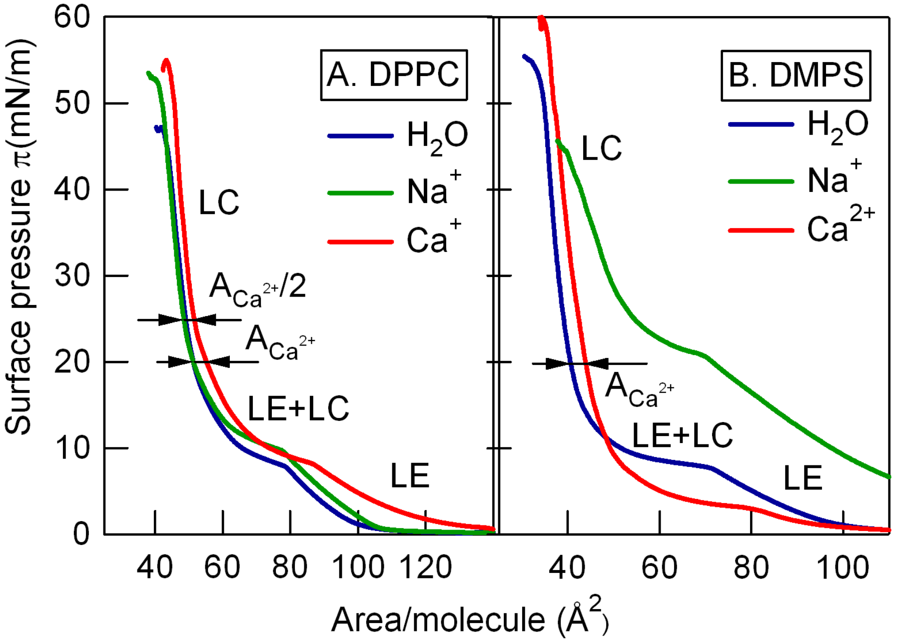

Figure 4.2 Pressure-area (π-A) isotherms of DPPC (A) and DMPS (B) on different subphases: neat water (blue), 1 M NaCl solution (green), 1 M $CaCl_2$ solution (red). The liquid expanded phase (LE), liquid condensed phase (LC) and the coexistence region of the two phases (LE+LC) are indicated along the isotherms. $A_{Ca^{2+}}$ represents the area of a calcium ion.

concentration can be neglected, as confirmed by control experiments using a 0.5 M $CaCl_2$ solution.

On water, the phase behavior of DPPC has been well documented [22, 29]. With decreasing surface area, the following regions have been identified: a gas phase, a liquid expanded (LE) phase, a plateau characteristic of the coexistence of the LE and the liquid condensed (LC) phase, and the pure LC phase.

With sodium ions present in the subphase, the compression isotherm for DPPC shifts to slightly higher surface pressures in the LE and LE+LC regions. The same effect has been observed previously [30] and was explained by disorder of the lipid chains induced by ions binding to the LE phase. At higher surface pressure, sodium has no effect on the compression isotherm, indicating no significant interaction of Na^+ with the LC phase: the ions are probably being “squeezed out” from the headgroup region.

A more dramatic effect is observed for a $CaCl_2$ solution subphase. Here, the surface pressure becomes non-zero at much lower densities (~140 Å^2/molecule), while the transition from the LE phase to the LE+LC coexistence region is less pronounced. In the LC region ($\pi > 20$ mN/m), the presence of calcium causes the lipid to take up 4 Å^2/lipid additional room– precisely the footprint of a Ca^{2+} ion (ionic radius of Ca^{2+} ion is r = 1.14 Å, therefore its area is ~ 4 Å^2). This indicates that at surface pressures exceeding 20 mN/m, the water hydrating the headgroups is partially replaced by calcium ions. At still higher surface pressures (>25 mN/m), the additional area drops by approximately 2 Å^2/lipid. The changes in molecular area difference can be interpreted in two ways: (1) a transition from a 1:1 to a 2:1 lipid:Ca^{2+} complex, as proposed previously from MD simulations [15] and/or (2) a change in the conformation of the lipid headgroup [6, 31].

For DMPS the compression isotherm on water (Figure 4.2B) shows the same phase behavior as DPPC, with a LE, LE+LC and LC region. However, upon compression, a smaller area per molecule can be reached. This indicates that PS is more compressible than PC, in contrast to the intuitive notation that Coulombic repulsive interactions between neighboring charged headgroups should expand the area per PS molecule. It was shown that strong intermolecular coordination of charged moieties of the neighboring PS headgroups plays a role in the area reduction [12].

When sodium ions are present in the subphase, the DMPS compression isotherms shift to higher surface pressure, the LE+LC plateau is less pronounced and the monolayer collapses at lower surface pressures (~ 45 mN/m). On a $CaCl_2$ solution, the LE+LC plateau is lowered to a pressure of $\pi = 5$ mN/m compared to the $\pi = 10$ mN/m pressure for coexistence region observed for pure water. At higher surface pressures ($\pi > 20$ mN/m) the displacement of the two isotherms remains equal to the Ca^{2+} footprint, 4 Å^2/lipid, and no apparent transition to a 2:1 lipid:Ca^{2+} complex is observed.

4.3.2 Fluorescence Microscopy

Coexisting phases within lipid monolayers can be visualized using fluorescence microscopy. Fluorescence images obtained for DPPC and DMPS monolayers - labeled with a fluorescent probe –along the isotherm, are displayed for three typical surface pressures in Figure 4.3. The dark areas correspond to ordered (LC) domains and the bright areas to disordered (LE) domains. For the neat water subphase (left column in Figure 4.3), the LC domains at low surface pressure are “bean”-shaped for DPPC (Figure 4.3a) [17] and “flower”-shaped for DMPS (Figure 4.3d). As the surface area decreases, the LC domains become interconnected by narrow regions of ordered lipids (Figure 4.3b) [32], before coalescing into a continuous LC phase (Figure 4.3c). The normalized area of the ordered dark regions, A_{dark}, obtained from an analysis of the fluorescence images (Figure 4.4), shows that the LC phase increases upon monolayer compression, and covers the entire monolayer for $\pi > 10$ mN/m. When calcium is present in the subphase, small ordered domains are observed at low surface pressure for both PC and PS monolayers (see Figure 4.3a). A much larger area of the monolayer is covered by these ~3.5 μm ordered domains for Ca^{2+} when compared to water (see Figure 4.4). These small domains at low surface pressure are thus calcium-induced and they occupy ~30 % (for PC) and 20% (for PS) of the surface. The presence of these domains is also evident from VSFG measurements presented below. Such Ca^{2+}-induced domains have thus far only been

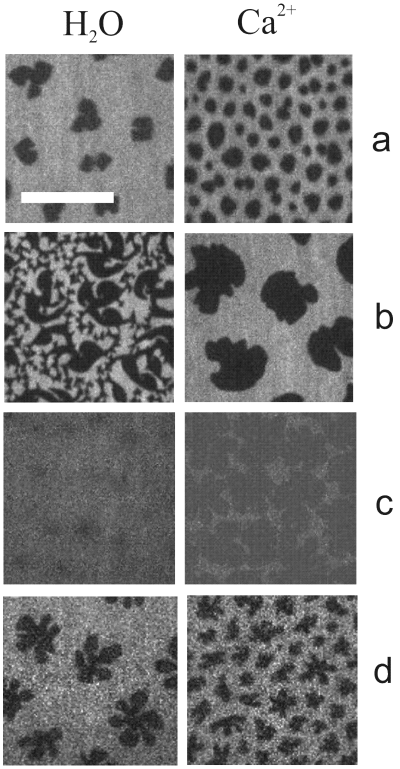

Figure 4.3 Fluorescence images for a DPPC (a,b,c) and DMPS (d) monolayer on water (left images) and 1 M CaCl2 solution (right images) for π = 4 mN/m (a), π = 6.5 mN/m (b), π = 35 mN/m (c), and π = 2 mN/m (d). Monolayers were labeled with 5 mol% Rhodamine-PE: the light regions correspond to the LE phase, and the dark regions are LC domains. The scale bar represents 15 μm. The contrast is the same for all images.

observed in mixed monolayer systems [33, 34]. At intermediate surface pressures (5 mN/m < π < 25 mN/m), it is evident from Figure 4.4 that the effect of Ca^{2+} is to reduce the density of ordered domains.

4.3.3 Vibrational Sum-Frequency Generation Spectroscopy

The molecular origin of this altered phase behavior in the presence of Ca^{2+} was further investigated with VSFG, a nonlinear vibrational spectroscopic technique that provides surface specific information on conformational order and orientation of interfacial molecules [21, 24]. In order to quantify the effect of ions on the conformation of the lipid tails, VSFG spectra were collected in the C-H stretch region. Spectra were measured for several surface pressures along the isotherms; spectra for the three different subphases are displayed in Figure 4.5 and 4.6 for the DPPC monolayer (at 20 mN/m and 35 mN/m) and DMPS monolayers (at 25 mN/m

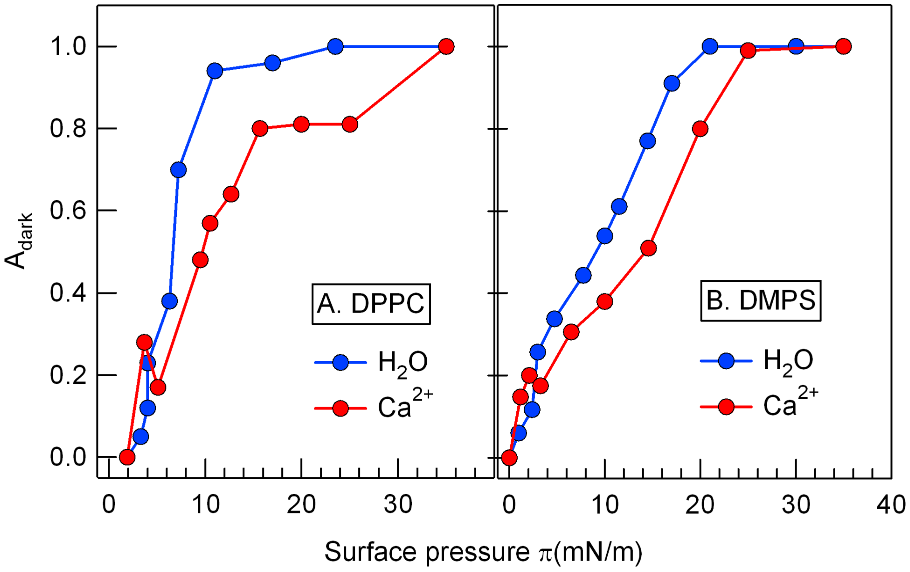

Figure 4.4 The fractional area of dark, ordered LC domains, A_{dark}, from the fluorescence images as a function of surface pressure for DPPC (A) and DMPS (B) monolayers on neat water (blue) and on 1 M $CaCl_2$ solution (red). Note the local maximum in A_{dark} around ~ 3 mN/m for both lipids in the presence of Ca^{2+} ions.

and 35 mN/m), respectively. Five vibrational modes can be observed: the peaks centered at 2876, 2938 and 2970 cm^{-1} have been assigned to the CH_3 symmetric stretch, CH_3 Fermi resonance and CH_3 anti-symmetric stretch, respectively [24]. The CH_2 symmetric and anti-symmetric stretch frequencies are found around 2846 and 2920 cm^{-1}. The choline C-H stretches for deuterated DPPC lipid monolayers (d62 and d75 DPPC) show very low signals and will be described below.

Upon compression of the monolayer, a marked decrease of the CH_2 intensities is observed. This can be understood from symmetry arguments: when the methylene groups in an alkyl chain change from cis- to trans-conformation, a local center of inversion appears which renders the CH_2 modes SFG inactive. The CH_3 intensities on the other hand, increase sharply as the monolayer is compressed, which is due to a narrowing of the angular distributions of chain tilt angles. The CH_3 and CH_2 symmetric stretch oscillator strengths can be obtained from fits to the data. Given the preceding arguments, the ratio *R* of the CH_3 and CH_2 symmetric stretch oscillator strengths provides a sensitive, empirical measure for the order of the lipid chains [20]. To reliably extract *R*, the data are analyzed globally using a Lorentzian multi-peak model (see eq.2.1, chapter 2), allowing only the peak amplitudes to vary as the surface pressure is modified. Ratio *R* for DPPC and DMPS is plotted in Figure 4.7 as a function of surface pressure (left panel) and as a function of area per molecule (right panel).

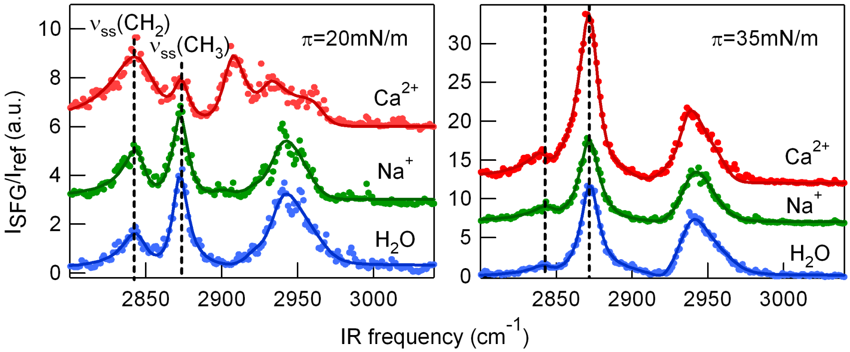

Figure 4.5 VSFG spectra of DPPC at π = 20 mN/m (left panel) and π = 35 mN/m (right panel). The vertical lines indicate the positions of methylene symmetric stretch ($\nu_{ss}CH_2$) and methyl symmetric stretch ($\nu_{ss}CH_3$). All spectra are normalized to a reference signal from *z*-cut quartz. The solid curves represent fits to the data using a Lorentzian model.

For DPPC monolayers on pure water and on a NaCl subphase, *R* varies in a similar fashion with pressure, with slightly, but reproducibly, smaller values of *R* in the presence of sodium. This indicates, as the pressure-area isotherms also show, that DPPC monolayers are slightly less ordered in the presence of Na^+, in agreement with previous reports pertaining to high concentration of NaCl in the subphase [30], but at odds with molecular dynamic simulations [11, 15], which indicate an ordering effect at ~10 mN/m surface pressure.

For DPPC on a subphase containing Ca^{2+} ions, *R* exhibits a small but reproducible peak at 5 mN/m, followed by a slight decrease between 10 and 20 mN/m and then increases sharply around 25 mN/m. The brief increase in order at low surface tension (~5 mN/m) is in good agreement with the results from fluorescence microscopy, which indicate an increase in order at these pressures as well (Figure 4.4).

For DMPS monolayers, the ratio *R* varies in a similar fashion as for DPPC monolayers as a function of surface pressure. However, as the surface pressure reaches 30 mN/m, the *R* values on water and on $CaCl_2$ solution subphases reach the same values (see Figure 4.7B), but lower values are found on a NaCl solution. This indicates that Na^+ ions induce disorder in the DMPS monolayers, this effect being similar for DPPC monolayers.

Further, the changes in orientation of the lipid head group are investigated upon calcium binding to the monolayer. Under most circumstances the average orientation of the phosphotidylcholine head group has been concluded to be parallel to the monolayer surface [21]. The way the cations affect the head group conformation is still not precisely known: a structural change was detected using magnetic resonance technique [22], indicating that the head group dipoles move away from the membrane surface, while molecular dynamics simulations established no significant reorientation [15]. An SFG investigation can offer more insights from a spectroscopic view. For this purpose, DPPC with deuterated tails was investigated,

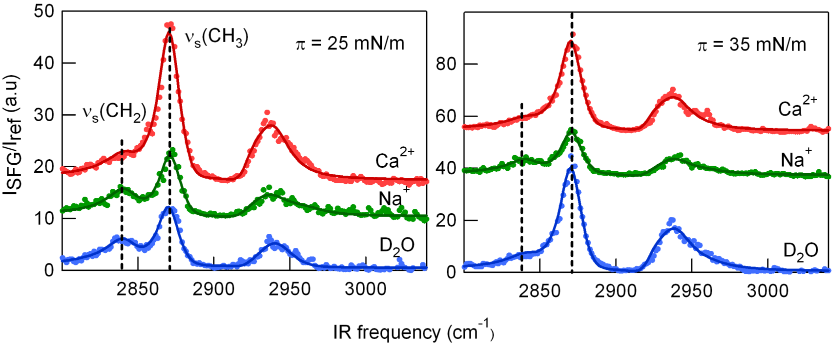

Figure 4.6 VSFG spectra of DMPS at π = 25 mN/m (left panel) and π = 35 mN/m (right panel). The vertical lines indicate the positions of methylene symmetric stretch (ν_sCH_2) and methyl symmetric stretch (ν_sCH_3). All spectra are normalized to a reference signal from z-cut quartz. The solid curves represent fits to the data using a Lorentzian model.

so that selectively the CH_2 and CH_3 vibrations from choline and glycerol groups can be probed. The deuterated DPPC monolayers were prepared at a surface pressure of 30 mN/m. As Figure 4.8 shows, we find no significant differences between SFG spectra of d62-DPPC and d75-DPPC (choline group deuterated as well), indicating that the signal arises only from the glycerol group. The ν_sCH_3 from the choline group is absent, revealing that the methyl group orientation must be close to 90° with respect to the surface normal. Upon addition of calcium ions, the signal from the CH_2 groups of glycerol does not change. Apparently the ions induce no conformational change in the glycerol backbone. Changes in the head group configuration in the choline region could not be observed, as the ν_sCH_3 remained invisible.

In the following, we will attempt to provide a unified picture of the monolayer phase behavior, using the results from surface tension measurement, fluorescence microscopy and VSFG measurements. We will first discuss the specific results for DPPC, followed by DMPS.

For DPPC, the ordered domains induced by Ca^{2+} - observed around 3 mN/m in the fluorescence images (see Figure 4.3 and 4.4) - are averaged out in the VSFG measurement as the probing area is ~10^{-2} mm^2, but give rise to a peak in the *R* value, as the average order in the monolayer is increased. Compressing further, the induced domains coalesce into larger ones. Simultaneously A_{dark} increases, but remains 20% lower for Ca^{2+} than for water (Figure 4.4A, 10 mN/m < π < 25 mN/m). This is again in good agreement with the VSFG spectra that indicate more disorder in the lipid tails for these surface pressures, as the CH_2 symmetric and anti-symmetric stretches at 20 mN/m are more prominent with Ca^{2+} in the subphase (Figure 4.5).

As the surface pressure reaches 25 mN/m, *R* increases sharply to reach a constant, large value. Interestingly, this sharp increase of *R* concurs with the position in the isotherm at which the lipid area decreases by 2 Å^2/lipid (see Figure 4.2), which we attribute (see above) to the transition from 1:1 lipid: Ca^{2+} complex in a 2:1 complex.

This implies that the increase of order, signified by the increase in *R*, involves a rearrangement of the headgroups, caused by a distinct change in the Ca^{2+} -lipid interaction. The 4 Å^2/lipid surface areas associated with the Ca^{2+} ion footprint is also evident from the different points at which the increase in *R* values occurs, when comparing Ca^{2+}-solution with pure water. The increase in *R* is shifted by precisely one unit of $A_{Ca^{2+}}$ when *R* is plotted versus area per lipid (Figure 4.7C).

At the point where the ratio *R* increases sharply for the Ca^{2+}-DPPC system (π = 25 mN/m), 20% of the monolayer area is still covered by the LE phase. The increase in the ratio *R* obtained from VSFG is not due to the disappearance of gauche-defects in the lipid tails, but can be attributed to the reorientation of alkyl chains in the LC phase towards smaller angles θ between the chains and the surface normal. This can be concluded (details in appendix A) from the ratio between the amplitudes of the ν_sCH_3 and methyl anti-symmetric stretch [21] which reveal that θ is 10° smaller for DPPC on Ca^{2+}- solution than for DPPC on pure water. At these pressures the presence of calcium ions causes a cooperative tilting of lipids towards the surface normal.

For DMPS, the results are remarkably similar to those observed for DPPC, for both Na^+ and Ca^{2+} ions, despite its different headgroup structure and charge. As the length of the apolar hydrocarbon chain is slightly shorter for DMPS (14 carbons for DMPS and 16 carbons for DPPC), lower *R* values are found for a compressed monolayer of DMPS when compared to DPPC. A direct correlation between the length of the alkyl chain and the relative order of the monolayer has been reported previously [35].

With Ca^{2+}, the ratio *R* shows a similar trend for the DMPS monolayer as for the DPPC monolayer: a peak is present at low surface pressure (~ 3 mN/m), and a sharp increase occurs at higher surface pressure (π = 20 mN/m), with an onset of $A_{Ca^{2+}}$towards higher areas per molecule (Figure 4.7D). Again, this is in good agreement with the isotherm data and fluorescence images. For DMPS at high surface pressures ($\pi > 30$ mN/m), *R* is found to be independent of the presence of calcium in the subphase, suggesting a similar acyl chain ordering at high pressures. Three differences between the two lipids may be noted: first of all, in the region 5 mN/m $< \pi <$ 25 mN/m, the Ca^{2+}-induced disorder observed for DPPC is also apparent for DMPS in the fluorescence results (see Figure 4.4), but less apparent from the VSFG results (Figure 4.7). Second, the transition from a 1:1 to a 2:1 lipid:Ca^{2+} complex observed for DPPC is not apparent for DMPS, although $A_{Ca^{2+}}$ appears in both the fluorescence and the VSFG data. Third, whereas Na^+ induces disorder in both lipids at high pressure (π >25 mN/m), this effect is significantly larger for DMPS- as observed from the compression isotherm and VSFG measurements (Figure 4.2 and 4.7). At present, we do not have a satisfactory explanation for these observations, other than that the difference must originate from differences in the headgroup structure. Despite these differences in some of the details of the ion-lipid interactions between DPPC and DMPS, it is evident that Ca^{2+} induces ordered domain formation in both lipids at low surface pressure, disorder at

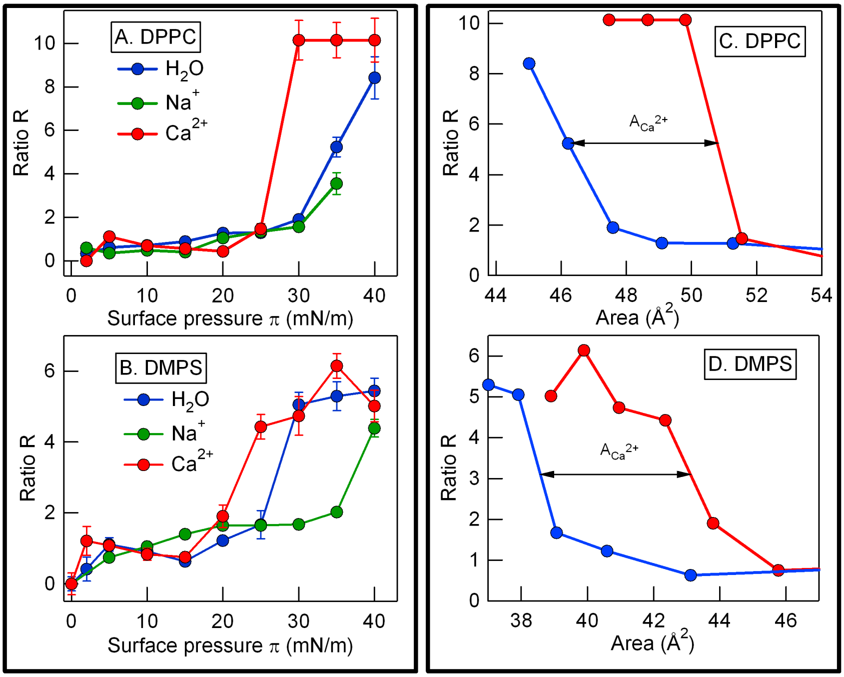

Figure 4.7 Left panel: the ratio R of the CH_3 and CH_2 symmetric stretch oscillator strengths (a measure for the lipid molecular order) as a function of surface pressure for DPPC (A) and DMPS (B) monolayers: pure water (blue), 1 M NaCl solution (green) and 1 M $CaCl_2$ solution (red). The ratio R could not be determined for Na^+-DPPC at $\pi = 40$ mN/m, due to collapse of the monolayer. The error bars are larger at higher pressures due to uncertainties in the amplitude of $\nu_s CH_2$ for a compressed monolayer. Right panel: the ratio R displayed as a function of area per lipid for DPPC (C) and DMPS (D) monolayers. Note the ~ 4 Å^2/lipid displacement (interpreted as the Ca^{2+} footprint), in agreement with the isotherms in Figure 4.2.

intermediate surface pressures (for DPPC), and high degree of order at the highest surface pressures. For both lipids, clear evidence is observed for complex formation between the lipids and Ca^{2+}, not present for Na^+. Sodium affects the lipid monolayers to a much lesser extent, mostly inducing disorder at high surface pressures (most notably for DMPS). Additional similarities between the two lipids are observed when investigating the orientation of water molecules near the headgroups. VSFG spectra for DPPC and DMPS on D_2O subphase in the O-D stretch vibrations (see chapter 7) indicate that hydrating water molecules are oriented in the same manner near anionic and zwitterionic headgroups. This indicates that PC behaves as an anionic lipid as the headgroup of DPPC is oriented with its choline group towards the interface [31]. Therefore, it is not surprising that calcium interacts similarly with PC and PS phospholipids, most probably coordinated with the phosphate moiety.

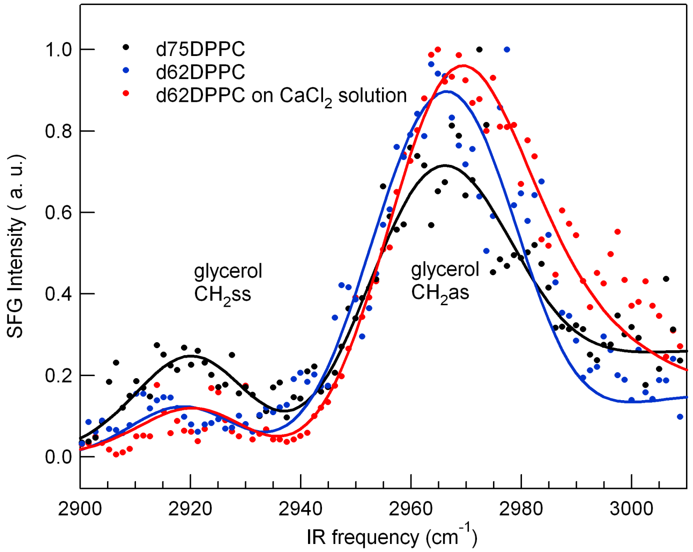

Figure 4.8 Normalized SFG spectra of deuterated DPPC: d75DPPC (black), d62DPPC on water (blue), d62DPPC on 1M $CaCl_2$ solution (red). The lipid monolayers were prepared at $\pi = 30$ mN/m. Solid lines are data fits. The peaks are assigned to the CH_2 symmetric stretch ($2920cm^{-1}$) and CH_2 antisymmetric stretch ($2965cm^{-1}$) vibrations from the glycerol backbone.

4.4 Conclusions

Summarizing, we use a combination of three complementary techniques to investigate the effect of cations on PC and PS monolayers. Our results indicate that sodium ions have very little effect on DPPC monolayers, mainly expanding the lipid monolayer. On the other hand, calcium has a pronounced effect, depending strongly on the surface pressure. At low surface pressures calcium ions induce the formation of small, ordered lipid domains, which coalesce into larger ones as the surface pressure increases. At high surface pressures, Ca^{2+} induces a “condensation effect” on both zwitterionic lipid and on anionic lipid monolayers, indicating that ions preferentially interact with the phosphate moiety in the lipid headgroup. In both VSFG and surface tension measurements, the molecular signature of the association of Ca^{2+} with the lipids is evident from changes in the signals between monolayers on water and Ca-solution corresponding to area changes of 4 $Å^2$/lipid – precisely the surface area of a Ca^{2+} ion.

References

[1] J. Zicha, J. Kunes, and M. A. Devynck, Am. J. Hypertens. **12**, 315 (1999).

[2] B. J. Ravoo, W. D. Weringa, and J. Engberts, Biophys. J. **76**, 374 (1999).

[3] W. D. Niles, J. R. Silvius, and F. S. Cohen, J. Gen. Physiol. **107**, 329 (1996).

[4] C. Chung Peng, S. J. F. Laudederkind, and L. R. Ballou, J. Biol. Chem. **269**, 5849 (1994).

[5] S. McLaughlin, S. N. Mulrine, T. Gresalfi, et al., J. Gen. Physiol. **77**, 445 (1981).

[6] J. Seelig, Cell Biol. Int. Rep. **14**, 353 (1990).

[7] H. Akutsu and J. Seelig, Biochemistry **20**, 7366 (1981).

[8] A. A. Gurtovenko, M. Miettinen, M. Karttunen, et al., J. Phys. Chem. B **109**, 21126 (2005).

[9] S. Gromelski and G. Brezesinski, Langmuir **22**, 6293 (2006).

[10] J. J. McManus, J. O. Radler, and K. A. Dawson, J. Phys. Chem. B **107**, 9869 (2003).

[11] R. A. Bockmann, A. Hac, T. Heimburg, et al., Biophys. J. **85**, 1647 (2003).

[12] J. J. L. Cascales, J. G. delaTorre, S. J. Marrink, et al., J. Chem. Phys. **104**, 2713 (1996).

[13] P. Mukhopadhyay, L. Monticelli, and D. P. Tieleman, Biophys. J. **86**, 1601 (2004).

[14] S. A. Pandit and M. L. Berkowitz, Biophys. J. **82**, 1818 (2002).

[15] S. A. Pandit, D. Bostick, and M. L. Berkowitz, Biophys. J. **84**, 3743 (2003).

[16] U. R. Pedersen, C. Leidy, P. Westh, et al., Biochim. Biophys. Acta **1758**, 573 (2006).

[17] C. W. McConlogue and T. K. Vanderlick, Langmuir **13**, 7158 (1997).

[18] V. T. Moy, D. J. Keller, H. E. Gaub, et al., J. Phys. Chem. **90**, 3198 (1986).

[19] V. Von Tscharner and H. M. McConnell, Biophys. J. **36**, 409 (1981).

[20] M. C. Gurau, S. M. Lim, E. T. Castellana, et al., J. Am. Chem. Soc. **126**, 10522 (2004).

[21] G. Ma and H. C. Allen, Langmuir **22**, 5341 (2006).

[22] S. Roke, J. Schins, M. Muller, et al., Phys. Rev. Lett. **90**, 128101 (2003).

[23] Y. R. Shen, Nature **337**, 519 (1989).

[24] X. Zhuang, P. B. Miranda, D. Kim, et al., Phys. Rev. B **59**, 12632 (1999).

[25] C. R. Flach, J. W. Brauner, and R. Mendelsohn, Biophys. J. **65**, 1994 (1993).

[26] G. W. H. Wurpel, M. Sovago, and M. Bonn, J. Am. Chem. Soc. **129**, 8420 (2007).

[27] J. Mattai, H. Hauser, R. A. Demel, et al., Biochemistry **28**, 2322 (1989).

[28] J. W. Zhang, A. Ebrahimpour, and G. H. Nancollas, J. Sol. Chem. **20**, 455 (1991).

[29] V. M. Kaganer, H. Mohwald, and P. Dutta, Rev. Mod. Phys. **71**, 779 (1999).

[30] A. Aroti, E. Leontidis, E. Maltseva, et al., J. Phys. Chem. B **108**, 15238 (2004).

[31] K. Makino, T. Yamada, M. Kimura, et al., Biophys. Chem. **41**, 175 (1991).

[32] G. Weidemann and D. Vollhardt, Biophys. J. **70**, 2758 (1996).

[33] D. M. Haverstick and M. Glaser, Proc. Natl. Acad. Sci. **84**, 4475 (1987).

[34] D. M. Haverstick and M. Glaser, J. Cell Biol. **106**, 1885 (1988).

[35] M. R. Watry, T. L. Tarbuck, and G. L. Richmond, J. Phys. Chem. B **107**, 512 (2003).

Chapter 5

Vibrational response of hydrogen-bonded interfacial water

In this chapter, the origin of the interfacial water vibrational response is investigated. We study here the sum-frequency generation response of water at different interfaces: water-air, water-glass and water-lipid. We reveal that the double-peak structure that appears in the vibrational spectrum of water molecules at the three interfaces originates from vibrational coupling between the stretch and bending overtone, rather than from structural effects. This is demonstrated by isotopic dilution experiments, which reveal a smooth transition from two peaks to one peak, as D_2O is converted into HDO. Our results show that the water interface is structurally more homogeneous than previously thought. Furthermore, the average hydrogen bond strength and its distribution are inferred through the center frequency and width, respectively, of the O-D stretch vibration of isotopically diluted HDO in H_2O. At the water-air interface, the SFG spectrum in the hydrogen-bonded region strongly resembles the Raman spectrum, indicating that at this interface the interfacial hydrogen bonding properties are very similar to those in bulk water. In contrast, for silica-water and lipid-water interfaces, interfacial hydrogen bonding is substantially stronger and also shows a larger degree of heterogeneity.

5.1 Introduction

Knowledge of the details of the water interfacial structure is essential both for a fundamental understanding of this ubiquitous liquid, and for the many technological applications where aqueous interfaces are relevant [1-4]. Water interfaces are characterized by the interruption of the bulk hydrogen bonded network, which gives interfacial water its unique properties (e.g. high surface tension). When a water OH group forms a hydrogen bond, the OH stretch frequency of this group decreases by an amount determined by the H-bond strength. Figure 5.1 shows the empirical relationship between the ν_{OD} vibrational frequency of a hydrogen bond donor as a function of the hydrogen bond length [5]. As a result, the vibrational spectrum in principle contains detailed information on the distribution of hydrogen bond strengths and the modulation thereof by intermolecular dynamics.

A distinct challenge in the study of interfacial water lies in the specific investigation of the water molecules that participate in forming the interface. For the majority of experimental approaches the response of the minor fraction of interfacial water molecules remains buried beneath the bulk response. As explained in chapter 1, vibrational sum-frequency generation (VSFG) technique provides a solution to this problem, as its selection rule result in the suppression of the signal from the isotropic bulk (see chapters 1 and 2). Indeed, SFG spectroscopy has been shown to be a very versatile tool in the study of interfacial water [6-14]. In the H-bonded region of the interfacial water response, two peaks have been identified (see Figure 5.2); however, the assignment of the two prominent peaks has been much debated. In one explanation, the two prominent peaks have been attributed to two distinct sub-structures of interfacial O-D groups with strong and weak hydrogen-bonds, and have been referred to as 'ice-like' and 'liquid-like', respectively [6-11, 15, 16]. Alternatively, the double-peak structure has been attributed to vibrational coupling between the two O-H (O-D) oscillators within one water molecule giving rise to the symmetric and the asymmetric water stretch modes [14, 17, 18]. Yet other approaches have considered the combined effects of the symmetric-asymmetric splitting and the structural inhomogeneities in the hydrogen-bond interaction strength on the vibrational SFG spectral response of the water-air interface [17, 18].

In this chapter, we provide a completely new assignment of the double-peak structure of the vibrational spectrum of the interfacial water. Our results reveal that the vibrational response does not originate from inter-molecular coupling (e.g. strong and weak H-bonded water species) [6-11, 15, 16], nor from symmetric and asymmetric water modes [14, 17, 18], but from symmetric stretch vibrations split by a Fermi resonance (FR) with the overtone of the water bending mode. This assignment is general for interfacial water, demonstrated here for different interfaces, and shows that the interfacial water structure is structurally more homogeneous and simpler than previously thought.

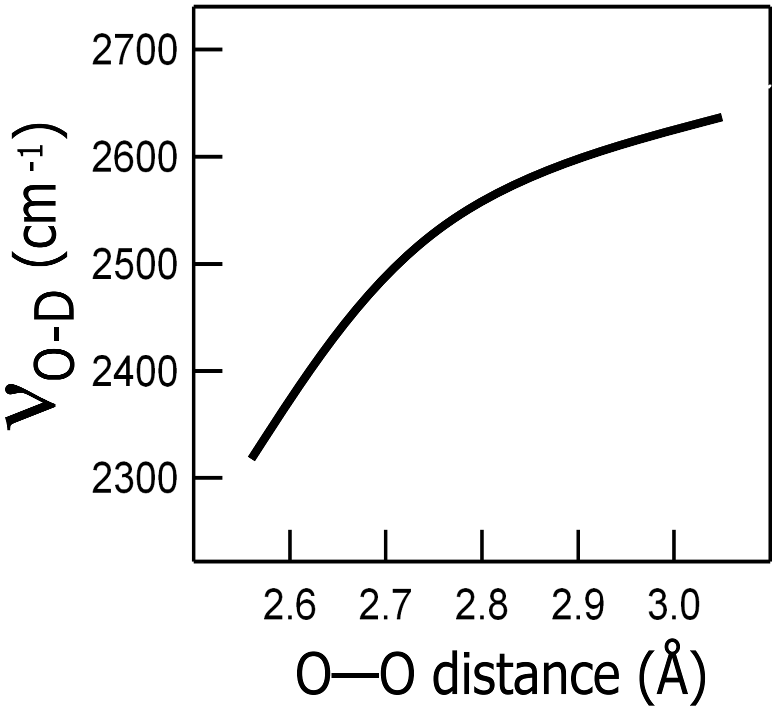

Figure 5.1 The frequency of the O-D stretch mode as a function of distance between two neighboring water molecules. As the distance O-O increases, the frequency of the O-D stretch mode increases. Therefore, $\nu_{O\text{-}D}$ can be used as a marker of the local hydrogen-bonding environment.

5.2 Experimental details

VSFG experiments

VSFG spectra were recorded under *ssp* and *pss* (SFG, VIS, IR) polarization conditions, in the 2000-2900 cm^{-1} region, while scanning the wavelength of the IR laser (see chapter 2). The incident angles for the VIS and IR beams were 35° and 40°, respectively, with respect to the surface normal for all interfaces. In addition, for the water-air interface, we have measured also SFG spectra for incident angles of 50° and 55° for VIS and IR, respectively. Using more grazing incident angles, the two peaks apparent in the H-bonded region are probed more efficiently [14]. In the experiments presented here, the O-D, rather than the O-H, stretch vibrations are probed, as our tunable infrared source works more effectively in this frequency range. Spectra in the O-H region differ only by a scaling of the frequency axis. This

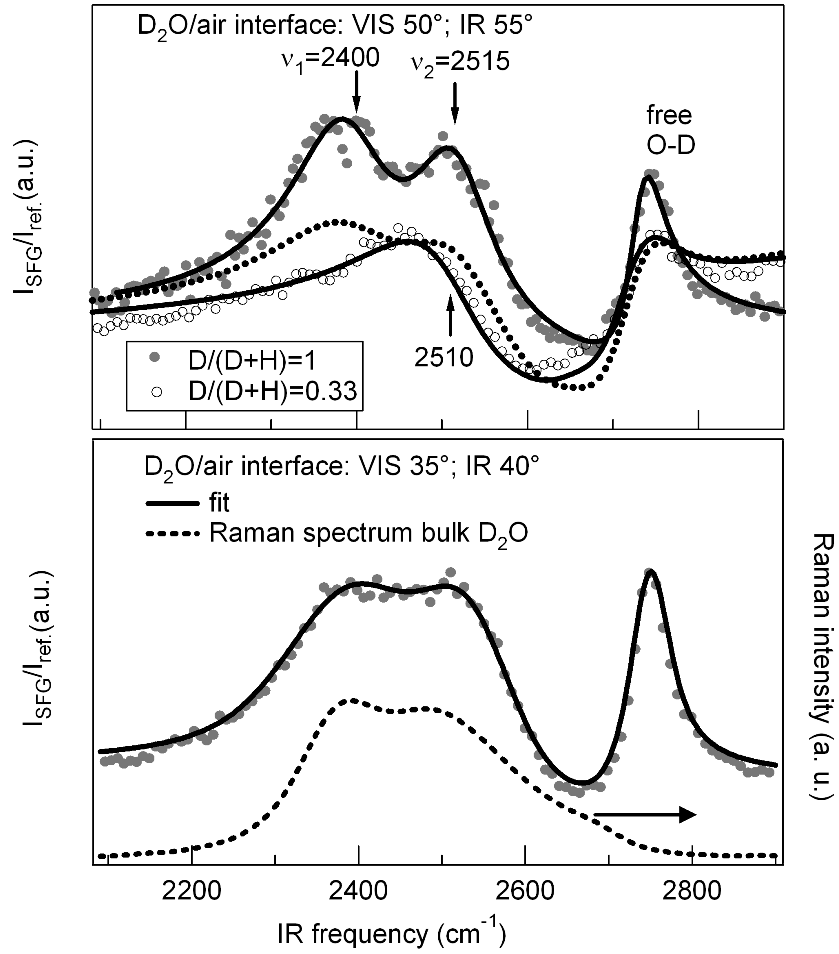

Figure 5.2 Top panel: VSFG spectra of the heavy water-air interface for *ssp* polarization. Fits to the data are shown by the thin solid lines. Simulated data for the 'ice-like' and 'liquid-like' hypothesis is shown by the dotted line. Peak positions are indicated in the graph. For pure D_2O (ratio D/(D+H) =1, closed circles), two resonances are clearly identified in the O-D stretch region, centered at ~2400 and ~2500 cm^{-1}. In addition, the 'dangling' OD peak is observed at ~2740 cm^{-1}. For a sample with D/(D+H) = 0.33 (open circles), a single resonance is observed centered at 2510 cm^{-1}. Here, the contribution from D_2O modes is less than 10%, and HDO modes dominate the spectrum. Bottom panel: SFG spectrum recorded under different incident angles of the IR and VIS beam. The solid lines are fits to the data; the dashed line represents the Raman spectrum of bulk D_2O, which bears a remarkable resemblance to the SFG spectrum. The Raman spectrum was recorded in parallel polarization geometry.

scaling suggests that there are no significant differences in water structure at interfaces for either pure H_2O or D_2O, and therefore for HDO. Isotopic dilution experiments are well suited for simplifying the complex vibrational response of water, as going from D_2O to HDO, the two O-D stretch modes are decoupled and the fundamental O-D vibration of HDO can be detected (see Figure 5.4).

Sample preparation

Lpid monolayers of L-1,2-dipalmitoyl-3-trimethylammonium-propane (DPTAP) were prepared at a surface pressure of 25±3 mN/m as described in chapter 2. For the SiO_2-water interface, a SiO_2 plate (150 μm thickness) was kept in chromosulfuric acid for one day, rinsed with ethanol and Millipore water, and dried using nitrogen. The SiO_2-heavy water interface was investigated at pD=11.5. At this pD, the surface is negatively charged, thus enhancing the OH stretch amplitude relative to that observed at neutral interfaces (water-air interface [7, 8, 19], water-quartz interface at low pH [20, 21]).

Data analysis

After normalizing the SFG spectra with a reference signal from a *z*-cut quartz to account for the IR profile, the spectra were fitted following the procedure described in chapter 2, using the expression:

$$I_{SFG} \propto \left|\left(\chi_{NR}^{(2)} + \sum_n \left[A_n / (\omega_{IR} - \omega_n + i\Gamma_n)\right]\right) * G_n(\omega)\right|^2 \qquad (5.1)$$

The convolution (*) with the Gaussian function $G_n(\omega)$ accounts for the instrument response, originating from the bandwidth of the VIS beam (full width at half maximum, fwhm = 28 cm^{-1}).

5.3 Results and discussions

5.3.1 Vibrational response of interfacial water

The VSFG spectrum of the heavy water-air interface (Figure 5.2) contains spectral features originating from specific interfacial water molecules: the 'free-OD' from water molecules with an O-D bond protruding from the surface ($\nu_{free} \approx 2740$ cm^{-1}), as its frequency is similar to the O-D stretch vibration in gas phase [6-11], and two peaks in the H-bonded frequency region ($\nu_1 \approx 2400$ and $\nu_2 \approx 2500$ cm^{-1}). We will focus here on the two peaks present in the hydrogen-bonded region of the water interfacial spectrum, from 2100-2500 cm^{-1}. The two peaks appear for many different aqueous interfaces (e.g. the water-air interface, the glass-water interface or the water lipid interface, see Figures 5.2 and 5.3). The relative intensities of the two peaks depend on the details of the interface. The presence of the two peaks for the D_2O-air interface becomes more clearly apparent from SFG experiments under more grazing incidence of IR and VIS beams (Figure 5.2 top and bottom panel): the two prominent peaks with symmetric character (as described below) are then probed more efficiently [14].

From the fit, the peak positions (and widths) for the pure water-air interface are found to be 2400 (140) and 2515 (120) cm^{-1}, respectively. The isolated O-D stretch frequency of HDO water molecule is 2510 (140) cm^{-1} (for D/D+H=0.33). For the water-lipid interface and SiO_2-water interface, the peaks are red-shifted and broadened (see Table 5.1) due to the interaction of the interfacial water with the lipids or the silica surface. Note that the SFG lineshape is distorted due to interference between nonresonant and resonant contributions in the SFG spectrum (Figures 5.2 and 5.3): the peak positions observed in the SFG spectrum are shifted from the resonance frequency by an amount depending on the relative amplitudes of χ_{NR} and χ_{RES} and their relative phase.

	ν_1	Γ_1	ν_2	Γ_2	ν_{HDO}	Γ_{HDO}
water-air	2400	140	2515	120	2510	150
water-lipid	2370	140	2520	180	2470	240
water- SiO_2	2330	205	2515	110	2420	270

Table 5.1 Central frequencies and linewidths (in cm^{-1}) of the O-D stretch vibrations inferred from SFG spectra at three different interfaces. Corresponding spectra are shown in Figure 5.2.

5.3.2 A smooth transition from D_2O to HDO spectra

Upon isotopic dilution of the water, the double-peak feature vanishes for all three interfaces (Figures 5.2 and 5.3). As opposed to previous reports [10, 11] the spectrum in the OD-stretch region clearly appears as a *single* resonance. Note that for D/(D+H)=0.33, HDO molecules are 4 times more abundant than D_2O molecules. This means that there will still be a small contribution from D_2O molecules to the signal. The D_2O contribution is most apparent in the SFG spectrum of the SiO_2-water interface, where a shoulder at 2520 cm^{-1} is still evident (see Figure 5.3). To quantify the individual contributions to the SFG spectra from HDO and D_2O molecules, we measured a complete set of data for varying isotopic ratio for the water-lipid interface, as shown in Figure 5.4. We choose the water-lipid interface, as the SFG signal is larger here than for the water-air interface due to the presence of interfacial charges. These experiments reveal a smooth transition from the D_2O to the pure HDO spectrum upon the isotopic dilution of D_2O. Figure 5.4B shows the amplitudes of the nonlinear susceptibilities of the three different modes obtained from a global fit to the data, using equation 5.1. The amplitude values follow closely the concentrations of D_2O and HDO in the samples (dashed lines in Figure 5.4B).

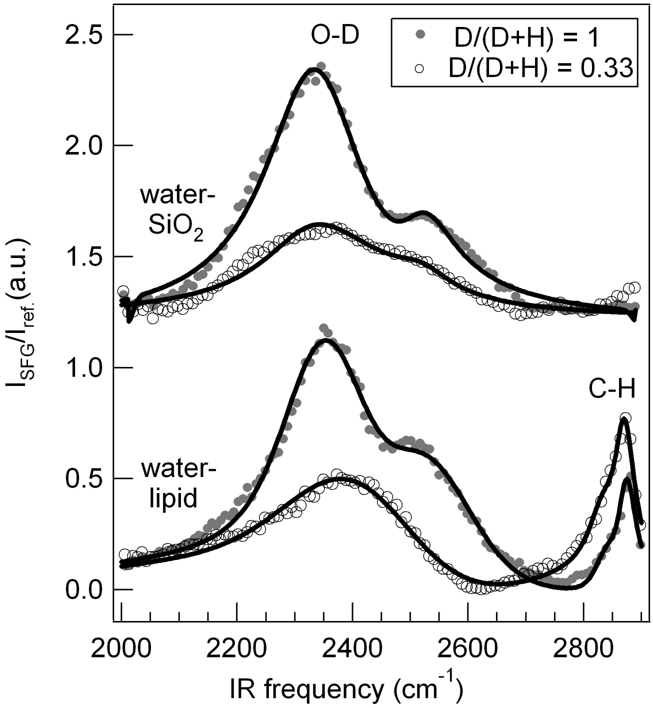

Figure 5.3 SFG spectra at different isotopic ratios of D/H for two different aqueous interfaces: the water-lipid (DPTAP) and the water-silica (pD=11.5) interface. For these interfaces, as for water-air interface, the double-peak structure disappears upon isotopic dilution. Lines are fits to the spectra, as explain in the text. Spectra from water-silica are offset for clarity. The isotopically diluted spectrum for the water-silica interface is multiplied by a factor of 2.

5.3.3 No ice/liquid-like interfacial water structures

The observation that the two O-D stretch peaks merge into one upon isotopic dilution of D_2O directly demonstrates that the double-peak structure observed for the isotopically pure water does not originate from weakly and strongly H-bonded water molecules. If the ‘ice-like/water-like’ hypothesis had been correct, the structure of the VSFG spectrum should have remained identical and only the amplitudes of the overall spectrum should have decreased upon isotopic dilution (see the simulated, dotted spectrum in Figure 5.2). The appearance of a new spectral feature in the SFG spectrum, as the molecular symmetry is broken in going from D_2O to HDO, suggests that the two O-D stretch peaks of interfacial D_2O originate from intra-molecular coupling, which is ‘switched off’ upon going from D_2O to HDO. The two peaks may

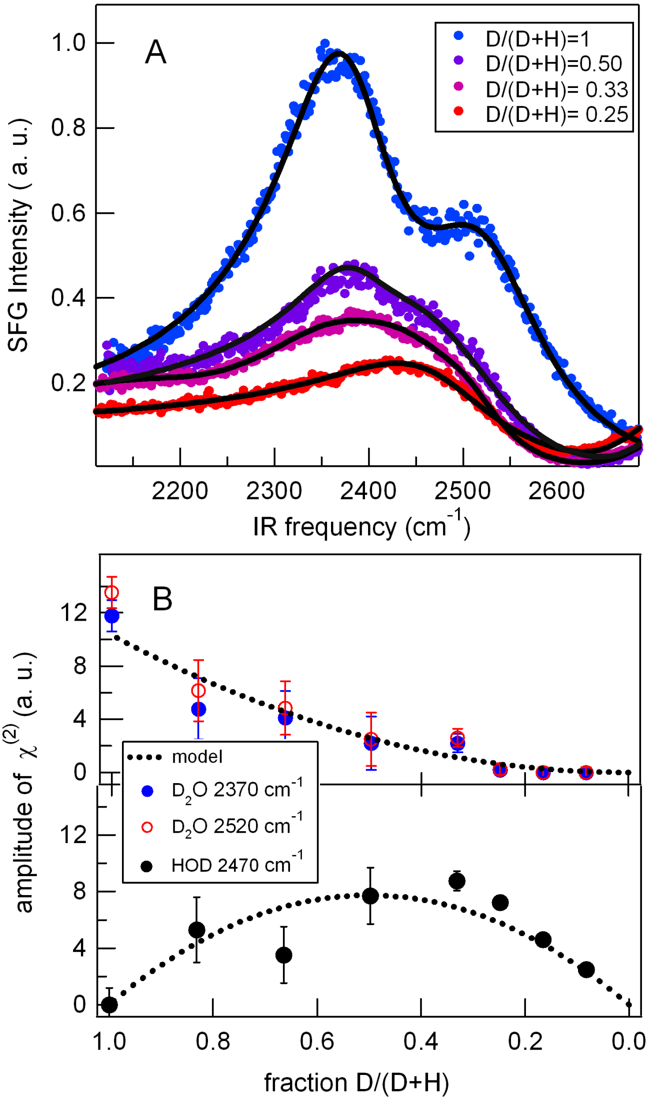

Figure 5.4 A: SFG spectra for different degrees of isotopic dilutions illustrate the gradual disappearance of the double-peak structure with decreasing D_2O content, for the water-DPTAP interface. B: amplitudes of the three different contributions to the overall spectra (two contributions from D_2O and one from HDO). Dotted lines depict the statistical D_2O and HDO concentrations. It is evident that the amplitudes of the different $\chi^{(2)}$ components simply follow the trend predicted from the concentration.

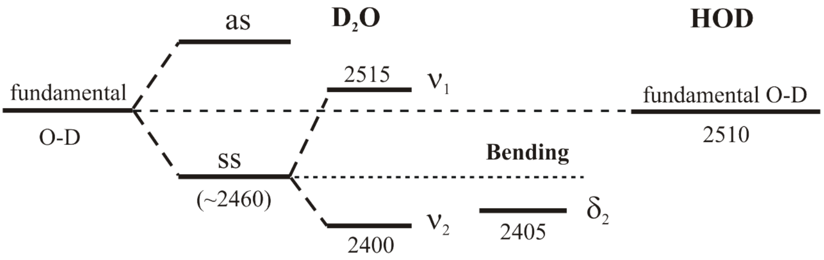

Figure 5.5 Energy level diagram for D_2O and HDO water molecules. The fundamental O-D stretch vibration is coupled intra-molecularly, giving rise to symmetric (*ss*) and asymmetric (*as*) modes. Due to Fermi resonance with the overtone of the bending mode (δ_2), the *ss* mode is further split into a low and a high frequency band (labeled here ν_1 and ν_2). For an HDO water molecule, the intra-molecular modes are decoupled, allowing the determination of the fundamental O-D stretch vibration. The corresponding frequency of each energy level is specified, except for the *as* mode, in cm^{-1}.

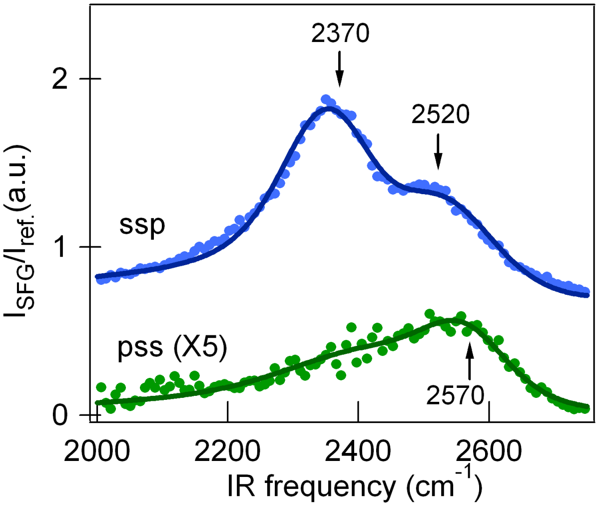

Figure 5.6 VSFG spectra of the lipid/water interface for *ssp* and *pss* polarization combination. The *ssp* spectra have been offset for clarity. Fits to the data are shown by the thin solid lines. The positions of the peaks are indicated, in cm^{-1}.

originate, for instance, from coupling between the two O-D stretches in D_2O, leading to symmetric (*ss*, low frequency) and asymmetric (*as*, high frequency) modes, as has been suggested previously [17, 18]. However, an interpretation of the spectrum in terms of *ss* and *as* modes can be ruled out on the following grounds: If the $\nu_1 = 2400$ and $\nu_2 = 2515$ cm^{-1} correspond to the *ss* and the *as* modes, respectively, then the frequency of the fundamental O-D vibration of the HDO water molecule would be expected at ν(O-D) $\approx [\nu_1 + \nu_2]/2 = 2460$ cm^{-1} (see Figure 5.5), in the approximation $m_D \ll m_O$. However, the observed OD stretch frequency in HDO for the water-air interface is found at 2510 ± 20 cm^{-1}. Secondly, if the $\nu_2 = 2515$ cm^{-1} peak originates from the *as* mode, then it should appear more markedly in the *ppp* and *pss* spectra, as stated by SFG polarization selection rules [14]. This is not observed experimentally (Figure 5.6): both peaks have vanishingly small intensities for *pss* polarization combination, and a new spectral feature appears at 2570 cm^{-1}. This peak was previously assigned to the other O-D bond of the interfacial water molecule which has a free O-D bond [14], but may also have a contribution from the *as* mode.

This new assignment of the two spectral features in the SFG spectrum of interfacial water implies that the two peaks originate from one mode. As such, the properties of the contributions to $\chi^{(2)}$ should be similar. To check their similar properties, we calculate the Im[$\chi^{(2)}$] spectra using Maximum Entropy Method (MEM) (see details in chapter 6). The Im[$\chi^{(2)}$] spectrum is particularly sensitive to neighbouring resonances with opposite sign, whereas the SFG intensity spectrum ($|\chi^{(2)}|^2$) is sensitive to neighboring peaks with equal sign. The results of the MEM analysis are displayed in Figure 5.7. For the water-air interface, we used the SFG spectrum of HDO water molecules (with the deuterium ratio D/(D+H)=0.33) as for pure D_2O the Im[$\chi^{(2)}$] spectrum cannot be reliable obtained from MEM analysis (see chapter 6). For water-SiO_2 and water-lipid interfaces, the two prominent peaks ν_1 and ν_2 have the same sign, which confirm once more that the two peaks cannot be assigned to the *ss* and the *as* modes. In addition, a new spectral feature appears at low frequency range, centered around 2200 cm^{-1}, with an opposite amplitude than the two main peaks, ν_1 and ν_2. This peak has been recently assigned to a collective, delocalized water mode [22]. For the water-lipid interface, the two prominent peaks present in the Im[$\chi^{(2)}$] spectrum also merge into one peak when going when the D_2O subphase is exchanged with the HDO subphase (see Figure 5.7). Similar result was observed for the Im[$\chi^{(2)}$] spectrum of the water-air interface, using phase-sensitive measurements [32].

The three arguments presented above show that the two prominent peaks (2400 cm^{-1} and 2515 cm^{-1} in the air-water spectrum) cannot be assigned to *ss* and *as* modes, and that, in fact, both have symmetric character, as both peaks are most prominent in *ssp* polarization conditions [14].

5.3.4 Fermi resonance coupling

In this section, we provide a consistent explanation for why the symmetric mode appears as a double-peak structure for D_2O, but not for HDO water molecules. Our observations described in the previous sections, indicate in fact that the symmetric mode is split by an anharmonic intra-molecular interaction. Indeed for bulk water, the symmetric stretch vibration is known to be affected by a Fermi resonance (FR) with the overtone of the water bending mode [23-25]. Such a resonance can occur when two states have similar energy. For bulk D_2O, the bending mode frequency is centered around 1210 cm^{-1} [26] which places the overtone of the bending mode in the vicinity of the symmetric stretch mode (Figure 5.5). The anharmonic interaction with the bend overtone splits the continuum of states associated with the symmetric mode into a low and a high frequency band, giving rise to the double peaked

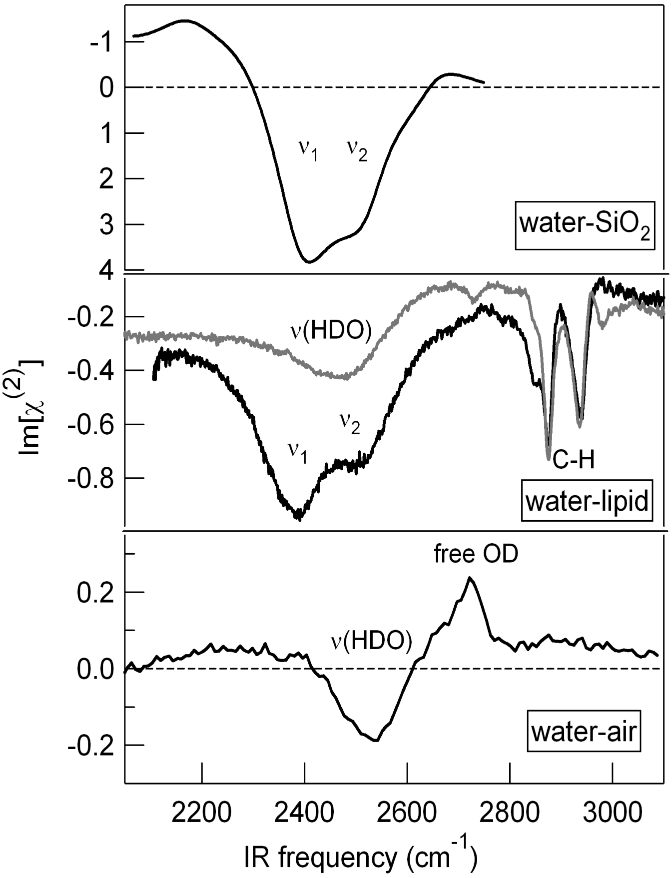

Figure 5.7 Imaginary spectra obtained from MEM analysis for water-SiO$_2$ (upper panel), water-lipid (middle panel) and water-air (lower panel) interfaces, respectively. Note the reverse axis for the water-SiO$_2$ interface. For the water-lipid interface, the HDO spectrum with the deuterium ratio D/(D+H)=0.33 is also shown in gray. For the water-air interface, the MEM analysis was applied to the mixture with the deuterium ratio D/(D+H)=0.33, as for D/(D+H)=1 the Im[$\chi^{(2)}$] spectrum cannot be reliable obtained from MEM analysis, as the phase changes more than 2π over the spectral window (see chapter 6). For the water-SiO$_2$ and water-lipid interfaces, the two prominent peaks ν_1 and ν_2 have the same sign, which further confirms our new assignment. The delocalized water mode at the red side of the spectrum is apparent for the water-SiO$_2$ and water-air, where the Im[$\chi^{(2)}$] flips sign.

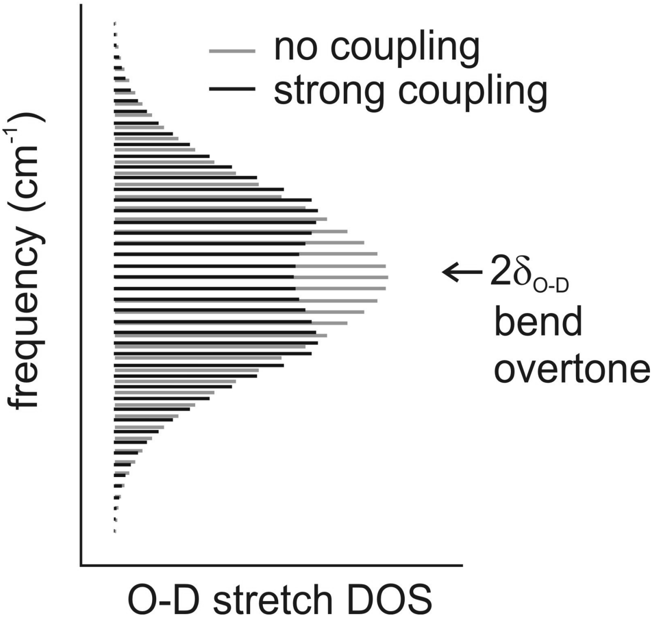

Figure 5.8 Formation of an Evans window due to anharmonic interaction between a continuum of stretch states with the overtone of the bend mode. At the bend overtone frequency, vibrational intensity of the stretch mode is transferred to lower, respective higher frequencies, giving rise to the Evans window. DOS stands for density of states.

structure in the SFG spectrum. The dip in SFG intensity between the peaks is therefore a so-called Evans window in the O-D stretching band reflecting the loss of spectral intensity in the middle of the stretch band [23-25], as schematically demonstrated in Figure 5.8. This FR-induced splitting has previously been used to explain the vibrational water response in Raman spectroscopy [24] (although this has been debated [27]) and ultrafast energy flow between OH stretch and bend modes, as observed in pump/probe IR experiments in bulk water [23]. The FR between the *ss* and bend overtone explains why, upon isotopic dilution the double-peak structure collapses into one resonance: for HDO, the bend fundamental is located at ~1450 cm^{-1} [28], so that the overtone is at ~ 2900 cm^{-1}, at much higher frequency than the *ss* mode. As a result, the Evans window does not appear for HDO. It also explains why the HDO frequency does not lie in between the two peaks, but rather at 2510 cm^{-1}: this is precisely the frequency of the decoupled O-D stretch in HDO in bulk water [28].

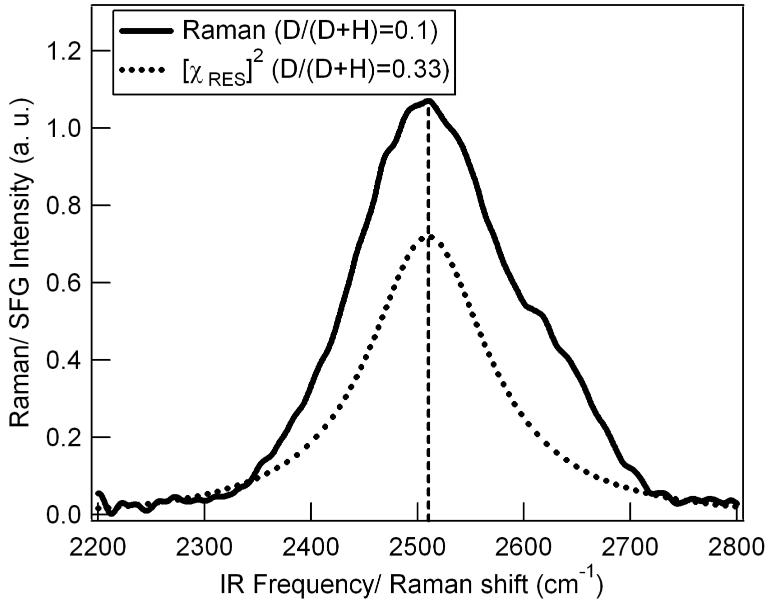

Figure 5.9 Illustration of the similarities between the bulk Raman and surface SFG response of isotopically diluted water. Solid line: Raman spectrum of isotopically diluted HDO in H_2O, revealing a peak at 2510 cm^{-1}. Dashed line: SFG response in the hydrogen-bonded part of the spectrum inferred from the fit in Figure 5.2 for the water-air interface reveals a very similar resonance at 2510 cm^{-1}. The Raman spectrum was recorded in parallel polarization geometry.

5.3.5 Implications in interpreting VSFG spectra

Our new assignment of the SFG water spectrum has implications in understanding the interfacial water response as a function of temperature and water ion content. When the temperature is increased, a decrease in the 3200 cm^{-1} peak and an increase in the 3400 cm^{-1} peak have been reported [7]. These changes in the spectrum have been interpreted as an increase in the disorder of the surface structure. However, no significant shift in the central frequency of either of the two peaks was observed, as one would expect when the hydrogen bonds become weaker with increasing temperature. With the new assignment of the spectral features presented here, we can explain the temperature dependence of water SFG spectra: the continuum of the symmetric stretch vibrations shifts to the blue upon an increase in temperature due to the weakened H-bonding structure. The positions of the maxima that appear due to coupling to the bend overtone are determined by the Evans window, which remains nearly at the same frequency due to the insensitivity of the bending mode to temperature (~0.05 cm^{-1}/K vs. ~1 cm^{-1}/K for the stretch mode) [26, 29]. The change in relative intensities of the two peaks therefore reflects the overall weakening of H-bonds, but do not point to a conversion of water species.

The same argumentation explains the effect of different hydrogen-bond making (F^- and SO_4^{2-}) and breaking (Cl^-, Br^-, I^-) ions on interfacial water spectra [11, 14, 17, 30]. A relative increase of the 3200 cm^{-1} peak and a relative decrease of the 3400 cm^{-1} peak was observed for ions that strengthen the H-bonds, while ions that weaken the H-bonds have the opposite effect. Similarly to the temperature dependence spectra, the peak positions (central frequencies of each peak) were not observed to change. With our new assignment the observed changes in relative peak amplitudes result from a constant frequency Evans window, with a redistribution of the symmetric stretching states toward lower or higher frequency for H-bond strengthening and H-bond weakening ions, respectively.

5.3.6 A new way of characterizing the interfacial water structure

The new assignment of the spectral features presented here explains many previously observed spectroscopic features of interfacial water, and has significant implications for interpreting water VSFG spectra. Most importantly, the intra-molecular coupling with the bend overtone makes the frequency of the symmetric stretch doublet relatively insensitive to the local H-bonding strength (see Table 5.1). This can be understood as follows: owing to the multitude of H-bonding states, there is a (dynamic) distribution of vibrational frequencies for the stretch vibration. The overtone of the pure bending mode (which is a forbidden transition and has a very low vibrational cross section compared to the stretch mode) interacts most strongly with those frequencies within the stretch manifold that are resonant with the bend overtone. The Evans window therefore appears at approximately the frequency of the overtone. The bend overtone is much less affected by the H-bonding interactions than the stretch [26]. Variations in the stretch mode central frequency therefore only give rise to changes in the spectral weight on both sides of the window, while the Evans window appear at the same frequency (see Figures 5.2 and 5.3). As a result, the D_2O interfacial water spectrum is relatively insensitive to the details of local environment, as the intra-molecular coupling dominates the vibrational response.

To characterize the hydrogen bonding, one should therefore rely on changes in the HDO frequency. The systems studied here serve as an excellent example. It is apparent from the analysis of the HDO spectra (Table 5.1) that the interfacial hydrogen bonding strength increases (ν_{HDO} decreases) when going from the water-air to the water-lipid to the water-glass interface. The linewidth – a measure for the distribution of hydrogen bond strengths – increases in the same order. It seems intuitive that hydrogen bonding would be strongest with the highly polar and negatively charged SiO_2 interface, with the water O-D groups pointing towards the SiO_2 surface. It is also not surprising that this interface would exhibit the most heterogeneity, given the inherent surface roughness of glass. The lipid DPTAP interface is also charged, but of opposite sign. This will induce a strong interaction with the electronegative oxygen end of the water molecules, but presumably less so with the deuterium atoms. Because the principal interaction of water with DPTAP is expected to be as a hydrogen bond acceptor (not donor) we expect, as we have indeed observed, that the shift of the OD center frequency on hydrogen bonding should be less than that for HDO at the SiO_2 surface.

Remarkably, for the air-water interface, the central frequency of the inferred resonance obtained from a simple fitting procedure (2510 cm^{-1}) corresponds very closely to the peak frequency of the Raman spectrum of HDO in H_2O. This implies that the hydrogen bond strength of water at the water-air interface closely resembles that of water in the bulk. To illustrate the similarities between the bulk Raman and interfacial SFG spectra for pure D_2O, we directly compared the Raman and the SFG spectra shown in Figure 5.2. It has previously been shown that SFG spectra resemble more to Raman spectra than to IR spectra [17, 31]. However, for the diluted HDO SFG signal, we cannot compare the Raman spectrum to the raw SFG spectrum, as the SFG peak position appears shifted due to interference with the non-resonant background; therefore, we use the $[\chi_{RES}]^2$ spectrum for comparison with the Raman response of HDO (Figure 5.9). The $[\chi_{RES}]^2$ spectrum shown here comes from the (single-resonance) fit to the hydrogen-bonded part of the HDO spectrum presented in Figure 5.2. The similarity between the hydrogen-bonded contribution to the SFG spectrum and the Raman spectrum is clearly evident from Figure 5.9, suggesting a close resemblance between the hydrogen-bonded structure of water at the water-air interface and that in bulk water.

5.4 Conclusions

In conclusion, our results show that the interfacial water response in the H-bonded region originates from intra-molecular coupling of vibrational modes, rather than from the existence of distinct water substructures. The two prominent peaks observed at aqueous interfaces are assigned to the symmetric stretch mode split by the Fermi resonance with the overtone of the bending mode. This coupling obscures the information on interfacial hydrogen bonding interactions contained in vibrational frequencies and linewidths of the O-D stretch mode. The intra-molecular coupling can be ‘switched off’ by investigating HDO rather than D_2O. The single predominant resonance that appears then in the SFG spectrum in the H-bonded region contains information about hydrogen bond strength and heterogeneity, through the central frequency and linewidth, respectively. Our results indicate that the interfacial hydrogen-bond strength varies at different interfaces. For the air-water interface, it is remarkably similar to the bulk, whereas for water-lipid and water-glass interfaces hydrogen bonding is significantly enhanced.

References

[1] M. A. Henderson, Surf. Science Rep. **46**, 1 (2002).
[2] S. K. Shaw and A. A. Gewirth, J. Electroanal. Chem. **609**, 94 (2007).
[3] A. Verdaguer, G. M. Sacha, H. Bluhm, et al., Chem. Rev. **106**, 1478 (2006).
[4] J. Milhaud, Biochim. Biophys. Acta **1663**, 19 (2004).
[5] S. Bratos, J.-C. Leicknam, G. Gallot, et al., (Eds.) Ultrafast Hydrogen Bonding dynamics and Proton Transfer Processes in the Condensed Phase. Kluwer Academic Publishers, Dordrecht, 2002, p. 5.
[6] Q. Du, E. Freysz, and Y. R. Shen, Science **264**, 826 (1994).
[7] Q. Du, R. Superfine, E. Freysz, et al., Phys. Rev. Lett. **70**, 2313 (1993).
[8] D. E. Gragson and G. L. Richmond, J. Phys. Chem. B **102**, 3847 (1998).
[9] M. J. Shultz, S. Baldelli, C. Schnitzer, et al., J. Phys. Chem. B **106**, 5313 (2002).
[10] E. A. Raymond, T. L. Tarbuck, M. G. Brown, et al., J. Phys. Chem. B **107**, 546 (2003).
[11] E. A. Raymond and G. L. Richmond, J. Phys. Chem. B **108**, 5051 (2004).
[12] A. V. Benderskii, J. Henzie, S. Basu, et al., J. Phys. Chem. B **108**, 14017 (2004).
[13] S. Gopalakrishnan, D. F. Liu, H. C. Allen, et al., Chem. Rev. **106**, 1155 (2006).
[14] W. Gan, D. Wu, Z. Zhang, et al., J. Chem. Phys. **124**, 114705 (2006).
[15] V. Buch, J. Phys. Chem. B **109**, 17771 (2005).
[16] D. S. Walker, D. K. Hore, and G. L. Richmond, J. Phys. Chem. B **110**, 20451 (2006).
[17] D. F. Liu, G. Ma, L. M. Levering, et al., J. Phys. Chem. B **108**, 2252 (2004).
[18] A. Morita and J. T. Hynes, Chem. Phys. **258**, 371 (2000).
[19] A. Ghosh, M. Sovago, R. K. Campen, et al., Faraday Discuss. **141**, 1 (2008).
[20] V. Ostroverkhov, G. A. Waychunas, and Y. R. Shen, Chem. Phys. Lett. **386**, 144 (2004).
[21] V. Ostroverkhov, G. A. Waychunas, and Y. R. Shen, Phys. Rev. Lett. **94**, 46102 (2005).
[22] B. M. Auer and J. L. Skinner, J. Chem. Phys. **128** (2008).
[23] S. Ashihara, N. Huse, A. Espagne, et al., Chem. Phys. Lett. **424**, 66 (2006).
[24] A. Sokolowska, J. Raman Spectrosc. **22**, 281 (1991).
[25] O. Henri-Rousseau, P. Blaise, and D. Chamma, Adv. Chem. Phys. **121**, 241 (2002)
[26] M. Falk, J. Raman Spectrosc. **21**, 563 (1990).
[27] D. E. Hare and C. M. Sorensen, J. Chem. Phys. **93**, 6954 (1990).
[28] P. Bodis, O. F. A. Larsen, and S. Woutersen, J. Phys. Chem. A **109**, 5303 (2005).
[29] A. J. Lock and H. J. Bakker, J. Chem. Phys. **117**, 1708 (2002).
[30] C. Schnitzer, S. Baldelli, and M. J. Shultz, J. Phys. Chem. B **104**, 585 (2000).
[31] R. N. Ward, D. C. Duffy, P. B. Davies, et al., J. Phys. Chem. **98**, 8536 (1994).
[32] C-S. Tian and Y. R. Shen, J. Am. Chem. Soc. **131**, 2890 (2009).

Chapter 6

Determining the absolute molecular orientation at interfaces

Here we report a numerical algorithm, Maximum Entropy Method (MEM), to obtain the absolute phase of the sum-frequency signal from Vibrational Sum-Frequency Generation (VSFG) spectra, without the need of phase-sensitive measurements. From the phase of the second-order susceptibility, we are able to determine the molecular orientation – i.e. whether molecular groups are pointing ‘up’ or ‘down’ – with respect to the interface. The phase retrieval algorithm is successfully applied to spectra obtained from three distinct samples: the water vibrations of the SiO_2-water interface, the methyl vibrations of a dodecanol monolayer on water, and the methyl vibrations of a self-assembled dodecanethiol monolayers on a gold substrate. Our results demonstrate that the approach is applicable to a wide range of spectra, with varying resonance widths and nonresonant background levels. For the SiO_2-water interface at high pH, we find that the water molecules are oriented with their hydrogen atoms toward the surface, and we show that the procedure demonstrated here provides information on interfacial vibrations that cannot be obtained from a multiresonance fit. For the surfactant monolayers we find, as expected, that the methyl groups point away from the substrate. We also discuss possible complications and limitations in determining the phase spectrum of the non-linear susceptibility using the Maximum Entropy Method.

6.1 Introduction

In chapter 5 of this thesis, it was shown that Vibrational Sum-Frequency Generation (VSFG) can be used to gain information about the structure of the molecules at the interface. In this chapter, we will prove that this technique can also provide information about the molecular orientation at the surface, e.g. the orientation of the transition dipole moment associated with a probed vibrational mode. The angle of the molecular transition dipole moment with the surface normal is typically provided by comparing the SFG intensities measured for a specific mode using different polarization combinations for SFG, VIS and IR [1]. It has been challenging, however, to determine whether the dipole is pointing up or down with respect to the surface. An approach to solving this problem is to find the resonant contributions to the second-order susceptibility, $\chi^{(2)}$, as the sign of the resonant amplitude is directly correlated with the absolute orientation of the transition dipole moment associated with a vibrational mode (see equation 2.3, chapter 2) [2, 3]. The sign and magnitude of the resonant amplitude are typically inferred indirectly from spectral fits using a Lorentzian model (as described in detail in chapter 2). However, it is challenging to accurately determine its absolute sign, as the shape of the overall SFG spectrum depends critically on the interference between the individual resonant contributions and the nonresonant background. In other words, knowledge about the phase of the SFG signal is required in order to unambiguously determine the absolute sign of the resonant amplitudes. This phase information is lost in VSFG, as the intensity spectrum detected is proportional with the modulus squared of $\chi^{(2)}$ [4]. To determine the molecular orientation at the interface without any *a priori* assumptions, it is therefore essential to access both the modulus and the phase of the nonlinear susceptibility.

As a result, there has been much interest recently in experimentally determining the phase of $\chi^{(2)}$ from interferometric measurements, employing a phase-sensitive SFG method developed in the group of Shen [5-7]. We demonstrate here an alternative approach using the Maximum Entropy Method (MEM) that can be used directly on SFG spectra. MEM is a method that allows one to extract the phase information from intensity spectra without any *a priori* knowledge of the physical processes involved. By maximizing the entropy of a probability distribution using MEM, the most probable result of this distribution is the measured data. Indeed, MEM is a proven method to retrieve the phase information from intensity spectra in several optical spectroscopies [8-13]. It has been successfully employed in third-harmonic generation spectroscopy [8], coherent anti-stokes Raman scattering (CARS) [9-11], and narrow-band VSFG spectroscopy [12, 13].

Here we present the MEM procedure applied for the first time to broad-bandwidth SFG spectra, which are ideally suited for MEM analyses, as those spectra contain a large number of data points. Broad-bandwidth SFG relies on mixing a femtosecond IR laser with a picosecond VIS pulse, as opposed to SFG spectroscopy using two picosecond lasers, in which the frequency of the picosecond IR laser is scanned. The latter mode of operation- which will be referred to as 'picosecond SFG' in the following - optimizes signal generation efficiency at one particular IR frequency. A clear advantage of this approach is that it results in high numbers of SFG photons being generated on resonance, owing to the high spectral brightness of the picosecond IR pulses. To obtain a full SFG spectrum, however, the IR laser has to be tuned. Not only is this method of acquiring spectral information relatively time consuming, but also power, pulse duration and spectral fluctuations, as well as timing jitter between the pulses from the two lasers, are negatively affecting the signal-to-noise ratio (SNR) of the SFG spectrum acquired in picosecond mode. In contrast, broad-bandwidth SFG spectroscopy [14-16] allows measurement of a significant part of the vibrational spectrum simultaneously, by using a combination of a broad-band and a narrow-band laser. Because in this mode of operation every pair of laser pulses contributes to the whole spectrum, the SNR of the acquired multiplex spectra is inherently not limited by the aforementioned laser fluctuations, generally leading to improved SFG spectra. Moreover, the broad-band spectra inherently contain a large number of data points N, which is beneficial for MEM, because larger N results in noise with higher frequency. This will be advantageous for MEM, as the higher frequency noise is more easily removed in MEM, without distorting the data, when compared with the low frequency noise (see section 6.2).

MEM is successfully applied here to retrieve the phase from SFG spectra with various nonresonant backgrounds and resonant peak widths. Previous applications of MEM to picosecond SFG data has shown that the background and peak widths affect the results of the phase-retrieval method [12, 13]. More specifically, MEM has a greater success rate in calculating the phase values from spectra containing large nonresonant backgrounds and narrow resonant peaks. Self-assembled monolayers (SAM) on a metal substrate are known to give rise to large nonresonant background; we analyze here the SFG spectra of a SAM of dodecanethiol on gold in the C-H stretch region. In addition, we demonstrate the successful application of MEM to two systems with low nonresonant background signal levels: a dodecanol monolayer on a water subphase in the C-H stretch region, a case for which the vibrational resonances are relatively narrow, and the O-D stretch vibrations of heavy water at the SiO_2-D_2O interface. For the latter interface, the SFG spectrum contains broad resonant peaks that cover the whole spectral range, making the unraveling of the interference between the background signal and the resonant contributions more difficult. We show in this chapter that the phase retrieval is successful for all three systems. In addition, we will discuss the limitations of this approach.

6.2 Theory

In this section, we discuss challenges in extracting the correct interfacial orientation using VSFG, as the phase information is lost in nonlinear optical spectroscopy. Furthermore we will show how MEM can be used to retrieve the phase from the VSFG intensity spectrum.

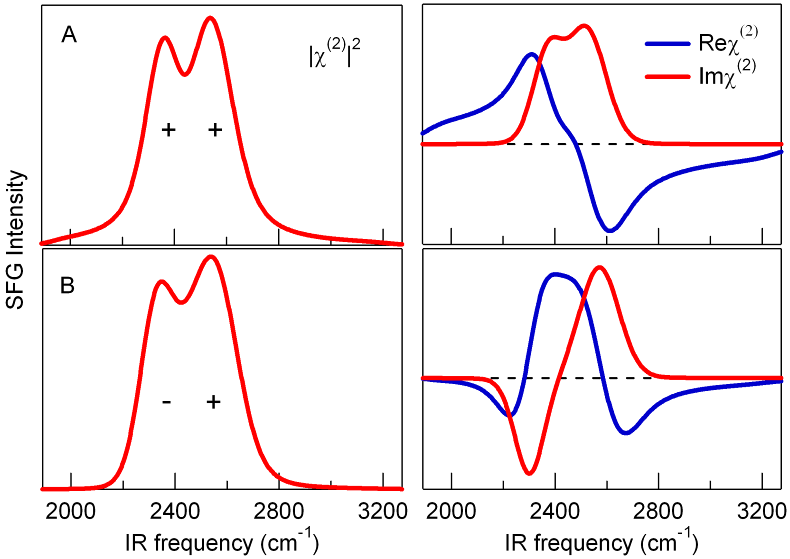

Figure 6.1 Left panels: simulated spectra ($|\chi^{(2)}|^2$) of two overlapping peaks having amplitudes with the same sign (A) and opposite signs (B). Right panel: the corresponding real (blue) and imaginary (red) parts of the $\chi^{(2)}$.

As mentioned in chapter 2, the second order susceptibility $\chi^{(2)}$ can be expressed as [1]:

$$\chi^{(2)} = A_{NR} e^{i\phi_{NR}} + \sum_n \frac{A_n}{\omega_n - \omega_{IR} - i\Gamma_n} = |\chi^{(2)}| e^{i\theta} \qquad (6.1)$$

Here, the first term of the sum represents the nonresonant susceptibility with the amplitude A_{NR} and its phase ϕ_{NR}. The second term is the resonant contribution to the susceptibility, with A_n the amplitude of the nth vibrational mode, ω_n the resonant frequency, ω_{IR} the infrared frequency tuned over the resonant frequencies and Γ_n the line width of the transition. θ represents the phase of $\chi^{(2)}$.

Equation 6.1 is normally used to fit the spectral features present in the VSFG spectrum, as described in chapter 2. The sign of A_n depends on the direction of the transition dipole moment [2, 3]. When two resonances have the same sign of A_n, the transition dipole moments of the two transitions are oriented in the same direction, while opposite signs of A_n shows that the transition dipole moments point in opposite directions. Using spectral fits to determine the signs of the resonant amplitudes with no *a priori* knowledge about molecular orientation can lead to the wrong interpretation of the spectrum. One such example is shown in Figure 6.1, where simulated SFG spectra are displayed, with $\phi_{NR} = 0$, $A_{RES}/A_{NR} \approx 250$, $\omega_1 = 2350$ cm^{-1} ($\Gamma_1 = 135$ cm^{-1}) and $\omega_2 = 2550$ cm^{-1} ($\Gamma_2 = 175$ cm^{-1}). These parameters are typical for the OD stretch vibration of heavy water. While the SFG spectra appear hardly distinguishable (left panel), they were generated using amplitudes with the same signs (Figure 6.1a) or with opposite signs (Figure 6.1b). This illustrated that a spectral fit may lead to an incorrect interpretation of the SFG intensity spectra.

To retrieve the absolute phase from VSFG spectra, we apply MEM, a method that maximizes the entropy *h* for a power spectrum S(ω) (i.e. the VSFG intensity spectrum). For the frequency interval (ω_1,ω_2), the entropy is defined as:

$$h \propto \int_{\omega_1}^{\omega_2} \log S(\omega) d\omega \tag{6.2}$$

Using variational calculus, we can express the spectral intensity for 2M+1 spectral points as:

$$S(v) = \frac{|\beta|^2}{|1+\sum_{k=1}^{M} a_k \exp(i2\pi kv)|^2},$$

where $v = (\omega - \omega_1)/(\omega_2 - \omega_1)$, with $\omega \in [\omega_1, \omega_2]$ and k=0,1,...,M. The coefficients a_k and β are determined from:

$$\begin{bmatrix} R(0) & R(-1) & \dots & R(-M) \\ R(1) & R(0) & \dots & R(1-M) \\ \vdots & \vdots & \ddots & \vdots \\ R(M) & R(M-1) & \dots & R(0) \end{bmatrix} \begin{pmatrix} 1 \\ a_1 \\ \vdots \\ a_M \end{pmatrix} = \begin{pmatrix} |\beta|^2 \\ 0 \\ \vdots \\ 0 \end{pmatrix} \tag{6.3}$$

Here *R*(*k*) is the autocorrelation of the time domain response, which is the Fourier transform of the power spectrum *S*(*v*):

$$R(k) = \int_0^1 S(v) \exp(i2\pi kv) dv$$

Then the solution of equation 6.3 maximizes the entropy, giving:

$$\chi^{(2)}(v) = \frac{|\beta| \exp[i\varphi(v)]}{1+\sum_{k=1}^{M} a_k \exp(i2\pi kv)} = \frac{|\beta| \exp[i\varphi(v)]}{A_M(v)}, \tag{6.4}$$

where $\phi(\nu)$ is the so-called error phase and A_M can be written as:

$$A_M(\nu)=1+\sum_{k=1}^{M} a_k \exp(i2\pi k\nu)=|A_M(\nu)|\exp[-i\psi(\nu)].$$

Then the frequency-dependent absolute phase θ associated with the vibrational transitions can be defined as:

$$\theta(\nu)=\psi(\nu)+\varphi(\nu), \tag{6.5}$$

where $\psi(\nu)$ is the phase of A_M, also called the MEM phase. $\psi(\nu)$ is the frequency-dependent quantity returned by the phase retrieval analysis as the most likely phase associated with the SFG intensity spectrum. The absolute phase, $\theta(\nu)$, is the frequency dependent phase associated with the surface vibrational resonances and represents our quantity of interest. It contains, in addition to the MEM phase, two additional contributions: the error phase $\phi(\nu)$ (as evident from equation 6.5) and the nonresonant phase ϕ_{NR} (see below). Further, we will discuss the physical meaning and the origin of those two phases and their contributions to the $\theta(\nu)$.

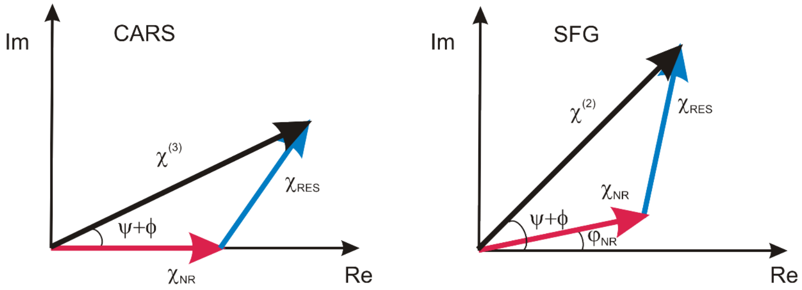

Figure 6.2 χ_{NR}, χ_{RES} and $\chi^{(2)}$ represented as vectors in the complex plane for CARS (left panel) and for SFG (right panel). For CARS, the absolute phase is equal with the sum between the MEM phase and the error phase. For SFG, the absolute phase contains an additional term: ϕ_{NR}.

The error phase $\phi(\nu)$ is a quantity contained in the MEM phase that may originate from a number of sources, but is most generally due to the presence of other (e.g. electronic) resonances that are distinct from the resonances under interest. As we will show below, $\phi(\nu)$ is very small in SFG. The nonresonant phase ϕ_{NR} is the phase associated with the nonresonant SFG intensity. It is important to note that this is not a frequency dependent quantity, and therefore the MEM routine is insensitive to the phase offset induced by this phase. As such, the frequency dependence of the retrieved $\psi(\nu)$ will directly reflect the resonant phase $\theta(\nu)$. We will make use of this property below.

The additional nonresonant phase term ϕ_{NR} in the calculated $\theta(\nu)$ phase was not accounted for in coherent anti-stokes Raman scattering (CARS) spectra, where the MEM procedure was previously successfully applied [9-11]. For CARS, the returned $\psi(\nu)$ phase from the MEM analysis could be directly used to determine the absolute resonant phase (see equation 6.5), with no additional correction for ϕ_{NR}. We can explain this difference between the two techniques by drawing the χ_{NR} and χ_{RES} as vectors in the complex plane (Figure 6.2). As CARS is a third-order process, χ_{NR} is a real number and therefore the Im[$\chi^{(3)}$] is simply equal to Im[χ_{RES}]. Hence the absolute phase will be equal to the sum between the MEM phase and the error phase. When χ_{NR} is complex, as for SFG, Im[$\chi^{(2)}$] contains contributions from both χ_{NR} and χ_{RES}, and the absolute phase will be obtained from correcting the MEM phase with two additional terms: the error phase, $\phi(\nu)$, and the nonresonant phase, ϕ_{NR}. These two phases are the only quantities that MEM cannot determine from the power spectrum $S(\nu)$, but they can be estimated or determined independently. The error phase has values close to zero and it is typically estimated with a slowly varying function over the frequency range, while the nonresonant phase can be obtained from interferometric measurements. For interfaces with no electronic resonances near the VIS or SFG frequencies, the nonresonant part of $\chi^{(2)}$ is expected to be real, therefore the nonresonant phase is equal to zero or π. [5, 7]

The absolute phase given by equation 6.5 and the retrieved phase $\psi(\nu)$ will allow us to calculate the imaginary spectrum of the resonant part of $\chi^{(2)}$ and of the overall $\chi^{(2)}$ as:

$$\mathrm{Im}[\chi_{RES}^{(2)}]=\sqrt{S(\nu)}\sin[\theta(\nu)] \tag{6.6}$$

$$\mathrm{Im}[\chi^{(2)}]=\sqrt{S(\nu)}\sin[\psi(\nu)+\varphi(\nu)+\phi_{NR}] \tag{6.7}$$

Therefore, the Im[$\chi^{(2)}$] spectrum can be obtained from the MEM phase, but only after correcting for the error phase and the nonresonant phase, as described above. To illustrate this correction procedure, we apply the phase retrieval method to simulated SFG spectra with known NR phase. We simulated two data sets with identical resonant peaks, centered at 2400 and 2600 cm^{-1}, with positive amplitudes and widths of 150 cm^{-1} (full width at half maximum). The two sets differ in the magnitude of the NR phase, set at ϕ_{NR} = 0.3 (as observed for the SiO$_2$-water interface [5]) and ϕ_{NR} = π/2 (as for a SAM on gold) . The true phase[$\chi^{(2)}$] and Im[$\chi^{(2)}$] spectra obtained from the simulation and those obtained from the ME procedure are displayed in Figure 6.3. The results show that the MEM phase and the MEM Im[$\chi^{(2)}$] spectra do not coincide with the simulated, true values, however the *shape* of the MEM phase is identical to the true phase. In fact, the MEM phase differs from the true phase (absolute phase) by exactly the nonresonant phase, as the retrieved phase is simply offset by ϕ_{NR}. Hence, by performing a correction of ϕ_{NR} to the MEM phase, the Im[$\chi^{(2)}$] spectrum is recalculated using equation 6.7. The corrected MEM Im[$\chi^{(2)}$] spectrum is now in good agreement with the spectrum from simulations (see

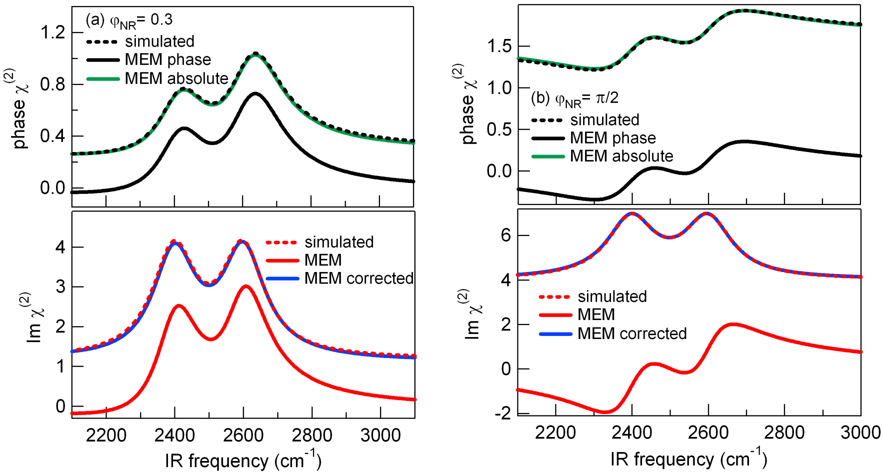

Figure 6.3 Phase (black) and imaginary part (red) obtained from simulated data (dashed lines) and retrieved by MEM (solid lines) for NR phase 0.3 (left panel) and π/2 (right panel). The green and blue curves indicate the MEM phase and the MEM imaginary spectra, respectively, after correcting for the nonresonant phase.

Figure 6.3). For the SFG spectra shown here, only a correction for ϕ_{NR} is necessary, as the error phase for the simulated data is zero. The correction procedure for the non-zero error phase is shown below in the results section.

6.3 Experimental section

VSFG setup

For SiO_2-water interface, the IR center frequency was continuously varied between 2050 cm^{-1} and 2750 cm^{-1} and the spectra were collected for 6 minutes. For the dodecanol monolayer on water and SAM on Au, the IR central frequency was set at 2900 cm^{-1} and spectra were collected for 3 minutes. All spectra were taken under *s*-polarized SFG, *s*-polarized VIS, and *p*-polarized IR conditions (denoted as: *ssp*). The obtained spectra were normalized using a reference signal from a *z*-cut quartz plate for SiO_2-water and dodecanol-water interface, while for SAM on Au the reference was taken from a bare Au substrate.

Samples preparation

SAMs on gold were prepared by immersing the gold substrates in a 1 mM solution of dodecanethiol in ethanol for 24 hours. The samples were then rinsed thoroughly with ethanol and ultra pure water (Millipore, 18 MΩ cm resistivity) and subsequently dried under a nitrogen flow. For the SiO_2-water interface, the SiO_2 plate (150 μm thickness) was kept for one day in chromosulfuric acid, rinsed with ethanol and

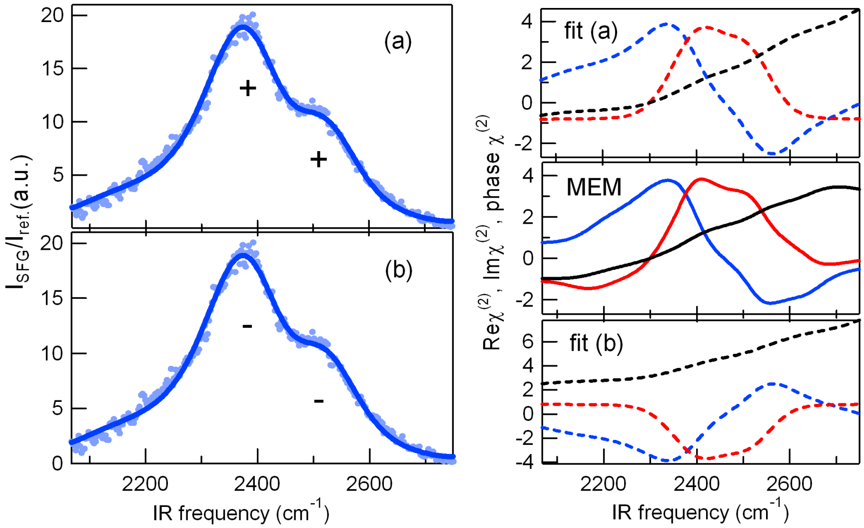

Figure 6.4 SFG spectra of glass-heavy water interface at pD=11.5. Left panel: fits using positive (a) and negative (b) amplitudes for the two peaks, respectively. Right panel: the corresponding real (blue), imaginary (red), and phase (black) obtained from the fits (dashed lines) and from MEM procedure (solid lines).

Millipore water, and dried using nitrogen. Dodecanol monolayers were prepared on Millipore water at a surface pressure of 25±3 mN/m.

6.4 Results and discussion

6.4.1 MEM for SFG spectra with broad resonant peaks

Figure 6.4 displays the SFG spectrum obtained from the SiO$_2$-heavy water interface at pD=11.5. At this pD, the surface is negatively charged, which further enhances the SFG signal when compared with neutral interfaces (water-air interface [2, 17, 18], water-quartz interface at low pH [5, 19]). The two prominent peaks are centered at ~2400 cm^{-1} and ~2510 cm^{-1}, respectively, and assigned to the water symmetric stretch vibration split by Fermi Resonance with the overtone of the bending mode (as explained in chapter 5).

Two fits are possible using equation 6.1, having the same signs of A_1 and A_2 (as expected from the spectral assignment, see chapter 5), but positive for $\phi_{NR} = 0.3$ (Figure 6.4, fit a) and negative for $\phi_{NR} = \pi$ (Figure 6.4, fit b). As it can be observed, the fits obtained from fit (a) and fit (b) are identical, although the signs of the resonant amplitudes are opposite. However, the two cases describe two mutually exclusive water orientations: positive resonant amplitudes imply that the symmetric stretch water dipole moment orients toward the surface, while negative values imply an opposite orientation. The Re[$\chi^{(2)}$], Im[$\chi^{(2)}$] and the phase of $\chi^{(2)}$ are clearly different in the two cases (see figure 6.4). To differentiate between the two cases, MEM can be applied to retrieve the phase and find the interfacial water orientation. The MEM phase presented in Figure 6.4 (middle right panel) matches the phase values obtained from fit (a), where A_1 and A_2 were positive and the nonresonant phase is close to zero. In fact, this result is not surprising: at pD=11.5, the interface is negatively charged and water molecules will orient with their electropositive deuterium atoms towards the surface, which will give rise to positive resonant amplitudes.

Further, we will focus on the spectrum of Im[$\chi^{(2)}$] because it may contain additional information about the molecular structure and orientation that are not easily captured from the phase spectrum. More specific, the Im[$\chi^{(2)}$] spectrum is particularly sensitive to neighbouring resonances with opposite sign, whereas the SFG intensity spectrum ($|\chi^{(2)}|^2$) is not; the $|\chi^{(2)}|^2$ is very sensitive to neighbouring peaks with equal sign. The Im[$\chi^{(2)}$] spectrum from the MEM procedure is obtained from equation 6.7, as described in the theory section. Because the nonresonant phase was found here to be close to zero [5] (ϕ_{NR} = 0.3), the Im[$\chi^{(2)}$] spectrum obtained with MEM needs only a small correction before its absolute value is determined. In fact, the MEM spectrum for Im[$\chi^{(2)}$)] (Figure 6.4) is in good agreement with the results from interferometric measurements on a negatively charged quartz-water interface [5]. We find that Im[$\chi^{(2)}$] has two positive peaks in the 2300-2700 cm^{-1} region (corresponding to the two prominent peaks in the $|\chi^{(2)}|^2$ spectrum) and an additional negative peak in the 2100-2300 cm^{-1} region. This negative peak was not captured in the Im[$\chi^{(2)}$] spectrum obtained from fit (a), and further shows the MEM ability to identify spectral features which are not easily observed in the SFG spectra or deduced from spectral fits. The flip in the sign of the Im[$\chi^{(2)}$] shows that there exist additional interfacial water species that have opposite orientation than the water molecules oriented by the local electric field created by the charged interface. In fact, the presence of those water species has also been observed for other aqueous interfaces (e.g. quartz-water interface [5] and water-air interface [7]).

6.4.2 Error phase correction for monolayers on an H_2O subphase

Next we will apply MEM to SFG spectra where the error phase has to be taken into account when calculating the imaginary part of $\chi^{(2)}$. Typically, the error phase correction is needed when the data contains wings of resonances not centered in the spectral observation window. This is not a common situation in SFG, but an example where those contributions do become significant is the SFG spectrum obtained from a dodecanol monolayer on an H_2O subphase in the C-H region (Figure 6.5). The main peaks present in the spectrum are assigned to the symmetric CH_3 stretch (~2875 cm^{-1}), the symmetric CH_3 Fermi resonance (~2945 cm^{-1}) and to the asymmetric CH_3 mode (~ 2960 cm^{-1}) [20-23].

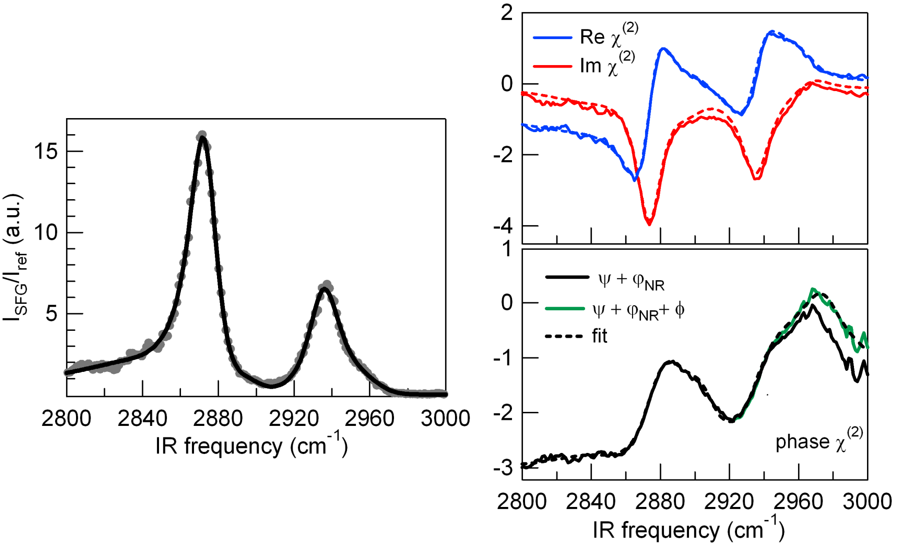

Figure 6.5 Left panel: the SFG spectrum of dodecanol monolayers. The fit to the data using a Lorentzian model is shown by the solid line. Right panel: the corresponding real (blue), imaginary (red) contributions to the resonant susceptibility obtained from the fit (dashed lines) and from MEM procedure (solid lines), using the retrieved phase that is corrected for both the nonresonant and the error phase. The corrected MEM phase for only nonresonant phase and for both nonresonant phase and the error phase is shown by the black and green solid lines, respectively.

We performed a spectral fit that contain these resonances, with negative amplitudes - corresponding to an orientation of the CH_3 symmetric stretch dipole moment away from the interface. [24] The nonresonant phase was found to be $\phi_{NR} = \pi$. This π shift in the nonresonant phase value when compared with the SiO_2-water interface is surprising, as the same ϕ_{NR} values are expected for all aqueous interfaces, since no electronic resonances are present. The imaginary part, the real part and the phase of $\chi^{(2)}$ found from the fit are displayed in the right panel of Figure 6.5, together with the results from MEM procedure. Here we have corrected the MEM phase spectrum for a contribution from ϕ_{NR}, allowing us to directly compare the results with the phase obtained from the fit (see Figure 6.5). After correcting for the nonresonant phase, the result is still not in agreement with the fitted values: a small but significant discrepancy remains between $\psi+\phi_{NR}$ and the phase obtained from the fit in the 2950-3000 cm^{-1} region. This is a clear indication that the absolute phase contains an additional term: the error phase. In fact, this additional term will include the change in the phase due to the presence of the OH stretch vibration at ~3200 cm^{-1}. It is the tail of this OH resonance that is centered outside the spectral range measured which

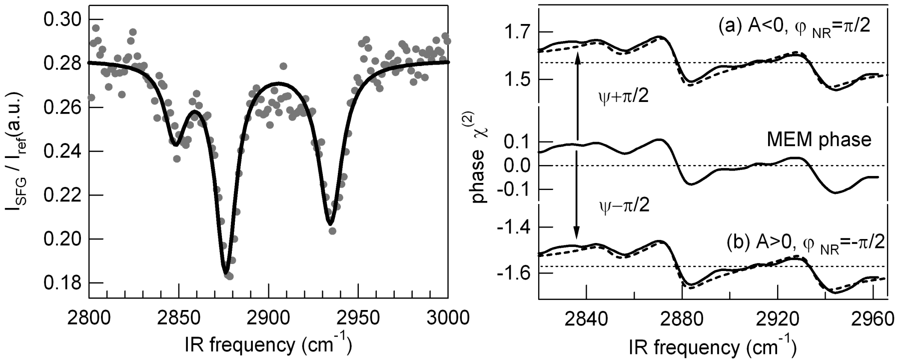

Figure 6.6 Left panel: SFG spectra of self-assembled monolayers (SAM) of dodecanethiol on gold surface. The spectrum was normalized using a reference signal from gold substrate. The fit to the data is shown by the solid line. Right panel: the dashed lines represent the phases corresponding to a spectral fit with (a) negative resonant amplitudes and $\phi_{NR} = \pi/2$ and (b) positive resonant amplitudes and $\phi_{NR} = -\pi/2$. The MEM phase is shown by the solid line. By correcting the MEM phase with either $\pi/2$ or $-\pi/2$, the phases obtained from the two possible fits are well reproduced.

is causing the discrepancy. By approximating the error phase with a slowly varying function, as previously estimated [8, 9], we can now recalculate the phase[$\chi^{(2)}$], Re[$\chi^{(2)}$] and Im[$\chi^{(2)}$] spectra from the MEM phase. The results show good agreement with the values obtained from the fit. Thus, for SFG spectra with additional resonances not present in the measured spectral window, the Im[$\chi^{(2)}$] spectrum can be accurately determined from the MEM phase by performing a correction that includes not only the nonresonant phase, but also the error phase.

6.4.3 MEM for SFG spectra with large nonresonant background

We have shown in the above sections that MEM can be successfully applied for SFG spectra where the nonresonant phase is very small or equal to π (in this case, the Im[$\chi^{(2)}$] only changes sign). In the following, we will discuss the possible complications when the nonresonant phase has large values (i.e. close to $\pi/2$ or $3\pi/2$). It is known that metal surfaces can give rise to a large nonresonant contribution with a non-zero phase in the SFG spectrum, as the sum frequency is near the resonances of surface electronic states. Here, we present the SFG spectrum of a SAM of dodecanethiol on a gold substrate. The spectrum, normalized to a spectrum from bare gold, obtained in the C-H stretch region is displayed in Figure 6.6. The spectral features present here are the same as those for the dodecanol monolayer on water described above. In addition, a peak at ~2845 cm^{-1} is observed, assigned to the symmetric CH_2 stretch vibration. The presence of this peak indicates the existence of a substantial number of gauche defects along the surfactant tails [23].

Two possible fits can be applied to this spectrum: one with negative resonant amplitudes and $\phi_{NR} = \pi/2$ and the other with positive resonant amplitudes and $\phi_{NR} = -\pi/2$. The phases obtained from the two fits are displayed in the right panel of Figure 6.6. The phases shows small variations around the value $\pi/2$ (fit a) or $-\pi/2$ (fit b) as a function of frequency (horizontal dotted line, Figure 6.6). When applying MEM to the spectrum, the returned phase contains the same spectral features as the fitted phase, but varying around zero. To obtain the absolute phase, the MEM phase needs to be corrected for the nonresonant phase, which in this case can be either $\pi/2$ or $-\pi/2$, as determined from the two fits. By adding or subtracting $\pi/2$, the MEM phase matches perfectly with the fitted phase and it cannot distinguish between the two fits. Without a priori knowledge about the nonresonant phase or about the interfacial molecular orientation, the MEM procedure cannot select the correct fit and therefore, determine the absolute phase. In fact, for our sample, we know that the monolayers will assemble on a gold substrate with their tails pointing away from the interface, into the air [25]. This will give rise to resonant amplitudes with negative values (similar to the dodecanol monolayers on water), pointing to the fit with positive nonresonant phase ($\phi_{NR} = \pi/2$). If the molecular orientation would not be known, knowledge of the nonresonant phase is required, which has to be obtained from independent measurements (e.g. phase-sensitive experiments). Thus, for SFG spectra that contain large nonresonant phases, the MEM procedure can be applied to determine the absolute phase only when *a priori* information about the nonresonant phase and/or when additional information on the molecular orientation is known.

6.4.4 MEM for water-air interface

Another distinct limitation of MEM analysis we found for the SFG spectrum of water-air interface (Figure 6.7). Here, the MEM procedure returned a phase spectrum different from interferometric measurements reported recently [7], and therefore predicts a different molecular orientation. From MEM, we inferred the orientation of the water molecules that give rise to the two peaks in the H-bonded region (2200-2600 cm^{-1}) to be the same as for the free O-D peak, while phase-sensitive measurements indicate an opposite orientation. For the MEM phase correction we used only the nonresonant phase correction $\phi_{NR} = 4$, as found from the Lorentzian fit corresponding to positive amplitude for the free O-D and negative amplitudes for the main two peaks in the H-bonded region (according to the phase sensitive measurements [7]). Note the π shift in the nonresonant phase as going from SiO_2-water interface to water-air interface. For SFG processes where no electronic transitions are present, the nonresonant is expected to be close to zero, which is not the value measured for the water-air interface or the lipid-water interface (see section 6.4.2 and chapter 7) [7]. The reason for the π shift in this case is not fully understood, but it could originate from the additional contributions to the

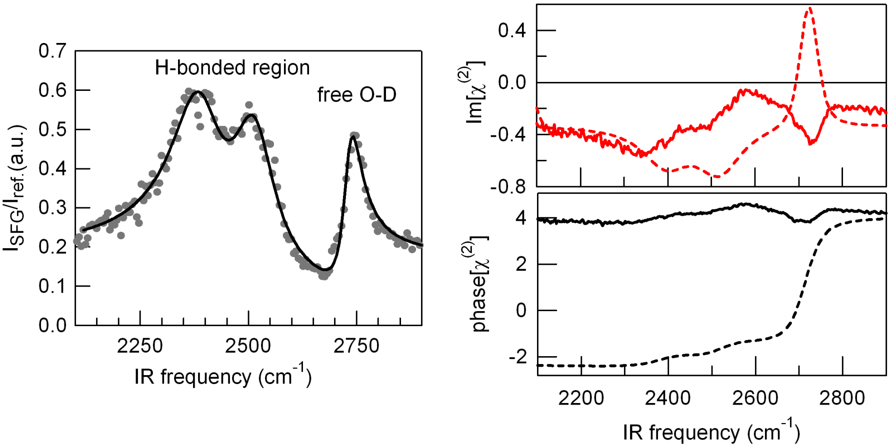

Figure 6.7 Left panel: the SFG spectrum for water-air interface. The fit to the data using a Lorentzian model is shown by the solid line with negative amplitudes for the two main peaks in the H-bonded region, and positive for the free O-D peak. Right panel: the corresponding imaginary part of $\chi(2)$ (red) and the phase obtained from the fit (dashed lines) and from MEM procedure (solid lines), using the retrieved phase that is corrected for the nonresonant phase $\phi_{NR} = 4$ obtained from the Lorentzian fit.

nonresonant background of the third-order susceptibility, $\chi^{(3)}$, as it will be explained in detail in chapter 7. The contributions of $\chi^{(3)}$ to the overall SFG signal become significant for charged interfaces, as a local electric field is created that interacts with the fields of the incoming beams. The contribution of $\chi^{(3)}$ to the signal depends therefore on the electric field, which is large for SiO_2-water interface and absent for the water-air interface. This additional term can change the nonresonant background and might be responsible for the change of the nonresonant phase when going from SiO_2-water to water-air interface.

For the case of water-air interface, MEM clearly fails in calculating the phase spectrum. This failure can be easily understood, and its occurrence can readily be recognized in other cases. Fits to the data along with the results from interferometric measurements [7] show that the frequency-dependent phase of $\chi^{(2)}$ changes by more than 2π over the frequency window of the experiment (see Figure 6.7). In this case the MEM procedure is no longer applicable, because a true phase of $(2\pi+x)$ cannot be recognized by MEM, as the MEM procedure will return phase x. Indeed, it is evident from equation 6.4 that these situations will be indistinguishable, whereas the underlying physics is different. As a result, the MEM procedure becomes inapplicable for spectra where the phase changes more than 2π. Hence, for all practical purposes, the MEM analysis should be applied most cautiously when one possible fit to the data reveals that the phase may vary in excess of 2π over the frequency window under investigation.

6.5 Conclusions

To conclude, we have used the Maximum Entropy Method to retrieve the phase information from SFG spectra. We show that the absolute phase can be determined accurately using the MEM analysis for different types of SFG spectra: with large or small nonresonant background and with large or small nonresonant phase. From the obtained phase spectrum we determined the absolute molecular orientation at the interface. Relating the phase to the orientation is straightforward for SFG spectra where the background phase is small (close to zero) or close to π, such as aqueous interfaces. We found that for dodecanol monolayers on a water subphase, the terminal groups of the alkyl chains point away from the surface, as expected. For the SiO_2-water interface at high pH, MEM shows that water molecules are oriented with their oxygen away from the surface. Furthermore, for the SiO_2-water interface at high pH, a new spectral feature at low frequencies was identified from the imaginary part of $\chi^{(2)}$, which was not apparent from the spectral fits. For systems with large nonresonant phase (around π/2 or 3π/2), exemplified here by the self assembled monolayers of dodecanethiol on gold, independent information on either the sign of the nonresonant phase, or some *a priori* information on the molecular arrangement is required to convert the retrieved phase into the phase of the resonant vibrations. Our results demonstrate that MEM is widely applicable and is a useful tool for the interpretation of SFG spectra. It can be applied not only to spectra with narrow resonant peaks, but also to spectra containing broad peaks where the spectrum away from the resonances is not known, and can be used for a wide range of nonresonant background strengths.

References

[1] X. Zhuang, P. B. Miranda, D. Kim, et al., Phys. Rev. B **59**, 12632 (1999).

[2] Q. Du, R. Superfine, E. Freysz, et al., Phys. Rev. Lett. **70**, 2313 (1993).

[3] D. K. Hore, D. K. Beaman, D. H. Parks, et al., J. Phys. Chem. B **109**, 16846 (2005).

[4] W. Gan, D. Wu, Z. Zhang, et al., J. Chem. Phys. **124**, 114705 (2006).

[5] V. Ostroverkhov, G. A. Waychunas, and Y. R. Shen, Phys. Rev. Lett. **94** (2005).

[6] N. Ji, V. Ostroverkhov, C. Y. Chen, et al., J. Am. Chem. Soc. **129**, 10056 (2007).

[7] N. Ji, V. Ostroverkhov, C. S. Tian, et al., Phys. Rev. Lett. **1**, 96102 (2008).

[8] E. M. Vartiainen, K. E. Peiponen, H. Kishida, et al., J. Opt. Soc. Am. B: Opt. Phys. **13**, 2106 (1996).

[9] H. A. Rinia, M. Bonn, M. Muller, et al., Chem. Phys. Chem. **8**, 279 (2007).

[10] E. M. Vartiainen, J. Opt. Soc. Am. B: Opt. Phys. **9**, 1209 (1992).

[11] E. M. Vartiainen, H. A. Rinia, M. Muller, et al., Opt. Express **14**, 3622 (2006).

[12] P. K. Yang and J. Y. Huang, J. Opt. Soc. Am. B: Opt. Phys. **14**, 2443 (1997).

[13] P. K. Yang and J. Y. Huang, J. Opt. Soc. Am. B: Opt. Phys. **17**, 1216 (2000).

[14] J. Liu and J. C. Conboy, Biophys. J. **89**, 2522 (2005).

[15] W. G. Roeterdink, O. Berg, and M. Bonn, J. Chem. Phys. **121**, 10174 (2004).

[16] T. Rasing, T. Stehlin, Y. R. Shen, et al., J. Chem. Phys. **89**, 3386 (1988).

[17] D. E. Gragson and G. L. Richmond, J. Phys. Chem. B **102**, 3847 (1998).

[18] M. Sovago, R. K. Campen, G. W. H. Wurpel, et al., Phys. Rev. Lett. **100** (2008).

[19] V. Ostroverkhov, G. A. Waychunas, and Y. R. Shen, Chem. Phys. Lett. **386**, 144 (2004).

[20] G. Ma and H. C. Allen, Langmuir **22**, 5341 (2006).

[21] S. Roke, J. Schins, M. Muller, et al., Phys. Rev. Lett. **90** (2003).

[22] M. R. Watry, T. L. Tarbuck, and G. L. Richmond, J. Phys. Chem. B **107**, 512 (2003).

[23] P. Guyot-Sionnest, J. H. Hunt, and Y. R. Shen, Phys. Rev. Lett. **59**, 1597 (1987).

[24] M. Oh-e, A. I. Lvovsky, X. Wei, et al., J. Chem. Phys. **113**, 8827 (2000).

[25] C. D. Bain, J. Am. Chem. Soc. **111**, 321 (1989).

Chapter 7

Buried water molecules in phospholipid monolayers

In this chapter, Vibrational Sum-Frequency Generation (VSFG) Spectroscopy in conjunction with the Maximum Entropy Method (MEM) is employed to determine the absolute water orientation at the interface of a phospholipid monolayer in contact with air. Our results demonstrate that water molecules interacting with a classical cationic surfactant are oriented intuitively with their O-H groups pointing down, i.e. with their oxygen towards the surfactant charge, and that the orientation is inverted when the surfactant charge becomes negative. Remarkably, at the negatively charged phosholipid-water interface and at the zwitterionic lipid-water interface, water orients counterintuitively with its oxygen up, towards the air phase. The orientation of water at phospholipid interfaces is therefore opposite to those of simple surfactants, which is due to the penetration of water into the lipid headgroup region, as is also predicted by MD simulations. We reveal, therefore, the existence of interstitial water molecules, localized between the lipid headgroup and its apolar alkyl chain, that have an 'upside down' orientation. Furthermore, the water structure near different types of lipid headgroups is determined from isotopic dilution experiments (HDO in H_2O). From the peak postion and peak width of the HDO spectrum, we determine that water molecules located below the lipid headgroup form stronger H-bonds than 'buried' water molecules present above the phospholipids headgroup. Additionally, we find that charged lipid headgroups induce a larger heterogeneity of the water structure.

7.1 Introduction

Biological membranes are the barrier between the interior and the exterior of the cell, and support many proteins involved in important cell functions. Although the biological membrane is mainly formed of hydrophobic parts (e.g. phospholipids), water plays an important role in the structure, stability, function and dynamics of biological membranes [1, 2]. More explicit, the water structure and orientation in the phospholipid vicinity strongly influence the lipid behavior: molecular organization, fluidity, etc [3, 4]. Therefore, the membrane-bound water is of particular interest. Despite the importance of membrane-bound water, many questions have remained open regarding its structure near cell membranes; in particular in relation to the charge of lipid headgroups. The presence of charge on lipid headgroups will cause water molecules to align in the electric or dipolar field. Changes in lipid headgroup structure are expected to alter the interfacial water structure, namely to disrupt the hydrogen bonding within the water. This disruption may extend several molecular layers from the surface [5, 6], but it is challenging to observe this effect directly.

We employ Vibrational Sum-Frequency Generation (VSFG) [7-9] Spectroscopy to probe membrane-bound water. Owing to its unique selection rules, VSFG is able to probe the outermost few molecular layers at the surface. As such, VSFG is an ideal tool to investigate water molecules near lipid headgroups. VSFG can provide information about both the structure and the orientation of the interfacial water molecules. The water structure can be found by probing the water OH stretch modes, as its frequency strongly depends on the water hydrogen-bond strength, and therefore on the local environment. The water orientation determines the sign of the non-linear optical susceptibility $\chi^{(2)}$ which governs the VSFG process [7-10], as explained in chapter 2 and 6 of this thesis. We retrieve the sign of $\chi^{(2)}$ from the interference of the resonant contribution with the nonresonant background using the Maximum Entropy Method (MEM) [9, 11], as explained in detail in chapter 6.

We demonstrate here that the interfacial ordering of water depends intricately on details of the lipid headgroup. We compare water at different phospholipids monolayers with water at simple surfactants. We find that for simple surfactants the water orientation flips when the surface charge is inverted. Surprisingly, this change in water orientation is not observed for the lipid-water interface when the surface charge is inverted. For both a cationic and an anionic lipid monolayer, the water molecules orient with their oxygens towards the surface. The counter-intuitive water orientation for anionic lipids demonstrates the existence of ‘buried’ water molecules, located between the phospholipid headgroups and their alkyl chains, while for classical surfactants we find no evidence for such buried water molecules. The existence of these water molecules is revealed also for zwitterionic lipids with a complex headgroup structure. Furthermore, we show using isotopic dilution experiments that ‘buried’ water molecules, present near the phospholipids headgroup, form weaker H-bonds in comparison to water molecules terminating the bulk.

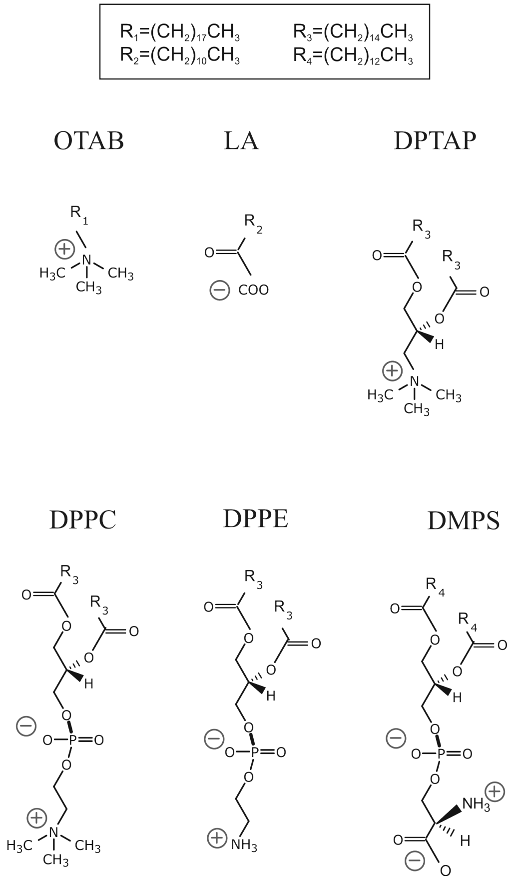

Figure 7.1 The chemical structures of OTAB, LA, DPTAP, DPPC, DPPE and DMPS.

7.2 Experimental section

The SFG setup used to record the spectra presented here is described in detail in chapter 2 and used here with only one modification. To record the spectra, an Electron-Multiplied CCD (Newton EMCCD, Andor Technologies) was used instead of an intensified CCD camera, that was used in the experiments presented in the other chapters of this thesis.

Monolayers of simple surfactants or lipids were formed on D_2O subphase (Cambridge Isotope Laboratories, 99.93% purity) or on isotopic mixtures D2O:H2O 1:3 at a surface pressure of ~20 mN/m. The surfactants used were lauric acid (LA, anionic) and octadecyl trimethyl ammonium bromide (OTAB, cationic) and they were purchased from Sigma-Aldrich. The lipids used in this study are: *L*-1,2-Dipamitoyl-3-trimethylammonium-propane (DPTAP, cationic),

lipid	ϕ_{NR}
LA	2.8
OTAB	-2.5
DPTAP	-2.3
DMPS	-1.4
DPPC	-1.2
DPPE	-1.1

Table 7.1 The values of the NR phase used to correct the MEM phase spectra for the surfactants and lipids, respectively.

1,2-Myristoyl-*sn*-glycerol-3-phosphoserine (DMPS, anionic), *L*-1,2-Dipalmitoyl-*sn*-glycerol-3-phosphocholine (DPPC, zwitterionic) and *L*-1,2-Dipalmitoyl-*sn*-Glycero-3-Phosphoethanolamine (DPPE, zwitterionic). The lipids were purchased from Avanti Polar Lipids.

7.3 Maximum Entropy Method

The Maximum Entropy Method is used to infer the sign of the water contribution to the resonant part of $\chi^{(2)}$, which contains information about the orientation. The method of calculating the imaginary part of $\chi^{(2)}$, Im[$\chi^{(2)}$], is explained in detail in chapter 6. Briefly, the phase spectrum obtained from MEM analysis, $\psi(\nu)$, is used to calculate the absolute phase spectrum, $\theta(\nu)$, and the Im[$\chi^{(2)}$] spectrum:

$$\theta(\nu)=\psi(\nu)+\varphi(\nu)$$

$$\mathrm{Im}[\chi^{(2)}]=\sqrt{I_{SFG}(\nu)}\sin[\psi(\nu)+\varphi(\nu)+\phi_{NR}]$$

Here, $\nu = (\omega-\omega_1)/(\omega_2-\omega_1)$, is the normalized frequency in the frequency interval $[\omega_1, \omega_2]$ (with $\omega \in [\omega_1, \omega_2]$) and $\phi(\nu)$ represent the error phase. For the spectra analyzed here, the error phase is negligible [9]. Therefore, only a correction for the NR phase is necessary. The ϕ_{NR} used to calculate the absolute phase for the surfactants and lipids are listed in Table 7.1. The ϕ_{NR} was chosen in the interval $[0,2\pi]$ in such a way that the following conditions are satisfied. First, the Im[$\chi^{(2)}$] should be negative in the C-H stretch region, as has been shown previously using phase-resolved measurements [12]. Second, Im[$\chi^{(2)}$] ≈ 0 in the regions without resonances [13]. Third, the C-H resonances must appear as (negative) peaks in the Im[$\chi^{(2)}$] at frequencies known with an accuracy of a few cm^{-1}, e.g. for CH_3 symmetric stretch (ss) the peak position is around 2875 cm^{-1} [14]. If ϕ_{NR} is not chosen corectly, the peaks will appear to be dispersive. Furthermore, for the VSFG spectra analyzed

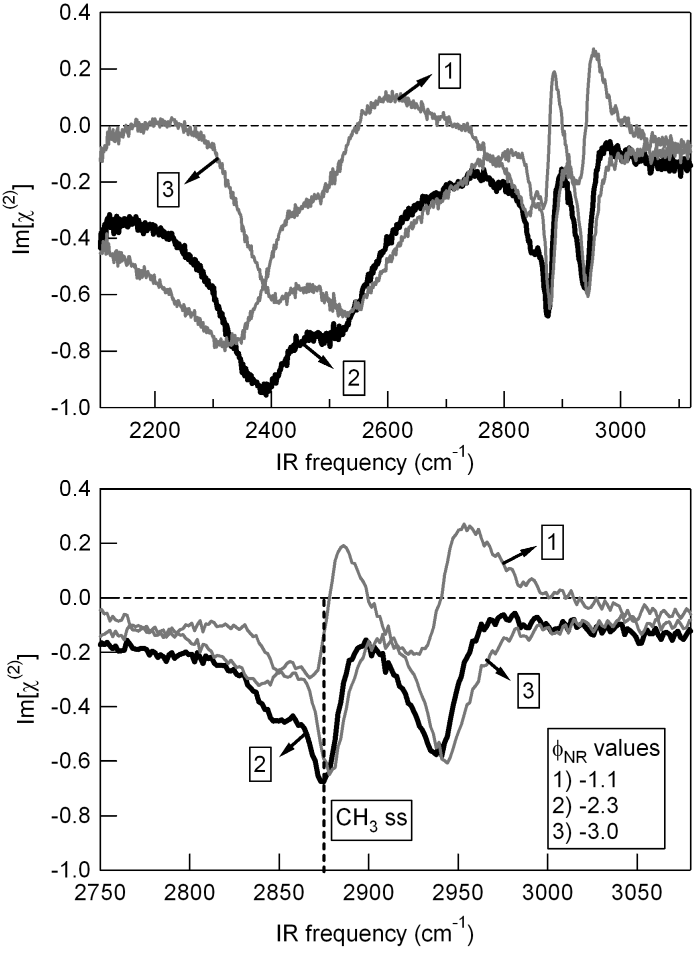

Figure 7.2 Top panel: the recalculated Im[$\chi^{(2)}$] spectra from MEM analyses for DPTAP monolayer with various NR phase around the chosen NR phase, ϕ_{NR} = -2.3. The ϕ_{NR} was chosen in such a way that the C-H modes have negative values and Im[$\chi^{(2)}$] ≈ 0 in the regions without resonances. Bottom panel: the same curves in the C-H stretch region. The vertical dotted line shows the position of the CH_3 symmetric stretch (2875 cm^{-1}).

here we used an additional restriction for ϕ_{NR}. For the surfactants we used the NR phase value close to the values found from the phase-sensitive measurements for the cationic and anionic surfactants [12]. There, $\phi_{NR} \approx -2$ for cationic surfactant and $\phi_{NR} \approx 2$ for anionic surfactant, respectively, in good agreement with the criteria sketched in the preceding paragraph. Hence, the NR phase value changes by a little over π, as the local electric field E_0 changes sign as going from a positively charged to a

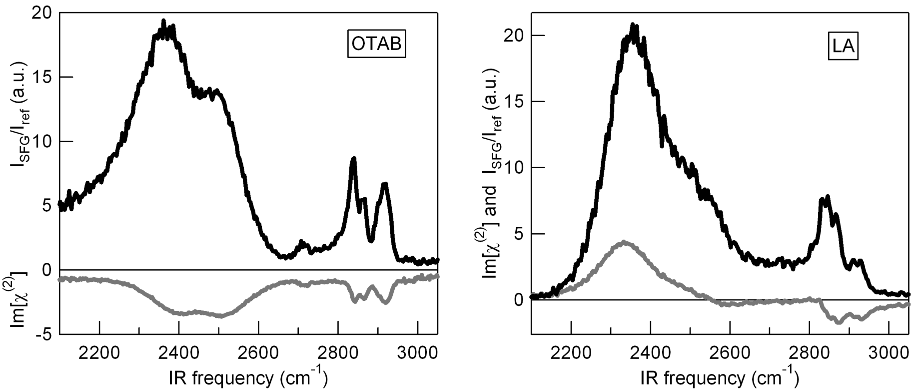

Figure 7.3 The SFG spectra (black) and the corresponding imaginary part of the nonlinear susceptibility (grey), $\mathrm{Im}[\chi^{(2)}]$, obtained from MEM analysis for charged surfactants on D_2O subphase: OTAB (left panel) and LA (right panel), respectively.

negatively charged interface. The obtained $\mathrm{Im}[\chi^{(2)}]$ has negative values in the C-H stretch region, as expected [12], while the values in the O-D stretch region are opposite for TOA and all lipids. This observation indicates that for these systems the water molecules are oriented oppositely to the CH_3 groups.

To illustrate the sensitivity of the obtained $\mathrm{Im}[\chi^{(2)}]$ spectrum to the NR phase correction, we calculated the $\mathrm{Im}[\chi^{(2)}]$ for DPTAP monolayers for ϕ_{NR} in the interval [-1.1, -3.0], around the chosen NR phase value $\phi_{NR} = -2.3$ (see Table 7.1). The results are displayed in Figure 7.2. For $\phi_{NR} = -1.1$, the peaks in the C-H stretch region have positive amplitudes and have a dispersive shape. On the contrary, those peaks have negative values for $\phi_{NR} = -3.0$, and the $\mathrm{Im}[\chi^{(2)}]$ spectrum is very similar to the one obtained for $\phi_{NR} = -2.3$. Therefore we conclude that we can determine ϕ_{NR} with an accuracy of ~ 0.7. Within this error in the ϕ_{NR}, there is significant uncertainty regarding the details of the *shape* of the spectrum, but we can indisputably determine the *sign* of the O-D stretch vibrations and determine the orientation of the water dipoles.

As the shape of the $\mathrm{Im}[\chi^{(2)}]$ spectrum depends on the nonresonant phase, direct conclusions about the change in the water structure near the different lipid headgroups based on changes in the vibrational response are not warranted. In principle, the change of the water structure can be determined from the change of the central frequencies of the peaks appearing in the $\mathrm{Im}[\chi^{(2)}]$ spectrum for the different monolayers studied here: as the frequency of the O-D stretch increases, the strength of the H-bonds decreases. However, due to the sensitivity of the spectral shape of $\mathrm{Im}[\chi^{(2)}]$ to the details of the non-resonant background we cannot make reliable statements about the water structure. In contrast, from isotopic dilution experiments, where the D_2O water molecules are replaced with HDO water molecules, we can determine the change in the water structure when comparing different interfaces (see chapter 5).

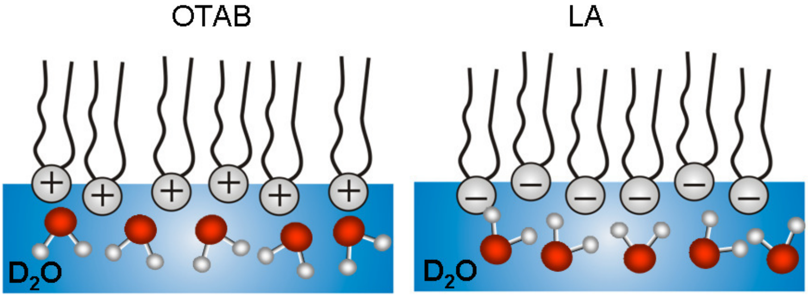

Figure 7.4 Schematic representation of the water orientation at surfactant-water interface. For the cationic OTAB monolayer, the water molecule orient with their oxygen towards the surface, while for the anionic LA monolayer, the water orientation is inverted.

The central frequency and the width of the single peak that appears in the SFG spectrum of the HDO water molecules are determined from a spectral fit using a Lorentzian model, as described in chapter 2. We will use this procedure below to determine the water structure near different lipid headgroup (see section 7.5).

7.4 Results and Discussion

7.4.1 Water orientation near simple surfactants monolayers

The SFG spectra obtained for the simple surfactants lauric acid (LA, anionic) and octadecyl trimethyl ammonium bromide (OTAB, cationic) monolayers on D_2O subphase are displayed in Figure 7.3. For both surfactants, the charge of the surfactant headgroups gives rise to an enhanced SFG signal when compared with neutral interfaces (e.g. the water-air interface [7, 15]) presumably due to the alignment of water molecules induced by the surfactant charge. The sharp peaks observed at the blue side of the spectra originate from the C-H stretch vibrations of the hydrocarbon chains: the CH_3 symmetric stretch, Fermi resonance and asymmetric stretch at 2875, 2945 and 2960 cm^{-1} [9, 14]. The amplitudes of the CH_3 symmetric stretch (CH_3-*ss*) obtained from the MEM analysis are negative for both surfactants - corresponding to an orientation of the CH_3 symmetric stretch dipole moment away from the interface, in good agreement with literature [12, 16]. In the O-D stretch region, however, the values of $\text{Im}[\chi^{(2)}]$ change sign - corresponding to an inversion of the interfacial water orientation. For the anionic LA monolayers, the water orients with their positively charged hydrogen atoms toward the surface (as shown in Figure 7.4), while for the cationic OTAB monolayers the orientation is opposite, as expected from simple electrostatics.

7.4.2 Water orientation near lipid monolayers

Figure 7.5 and 7.6 display the VSFG spectra for four lipids: DPTAP (cationic), DMPS (anionic), DPPC (zwitterionic) and DPPE (zwitterionic). The corresponding Im[$\chi^{(2)}$] spectra are calculated from the absolute phase after the correcting the MEM phase with the nonresonant phase, as described in section 7.3. Remarkably, the MEM results show that the spectra have negative values in the O-D stretch region for all four lipid monolayers. For all lipids, the water molecules are oriented as for cationic OTAB monolayer (with their oxygen towards the surface), although the surface charge is very different. This observation is remarkable, as one would expect that the electric field created by the charged interface would orient the water molecules in opposite direction when going from DPTAP (cationic) to DMPS (anionic) monolayers. For DPTAP monolayers, the water molecules are oriented as for OTAB monolayers, as expected; while for DMPS water molecules have a counter-intuitive orientation. These observations can be explained as follows. DPTAP is not a phospholipid (as opposed to the other three lipids) and has a relatively simple headgroup structure, much like the surfactants LA and OTAB. For LA, OTAB and DPTAP, we detect the water molecules situated ‘beneath’ the headgroup. In contrast, phospholipids like DMPS have a more complex head group structure, and previous studies have demonstrated that water penetrates the headgroup region up to the lipid chains, i.e. above the phosphate group. [17] The orientation of water will therefore change going from bulk to water near the alkyl chain, [18] and for DMPS we detect the ’buried’ water between the headgroup and the lipid tail (see Figure 7.7).

This interpretation is consistent with the observation that water in contact with zwitterionic lipids DPPC and DPPE (Figure 7.6), is oriented in the same fashion as DMPS, because the headgroups are identical between the phosphate group and the alkyl chains (see Figure 7.1). Water situated above the phosphate region is therefore expected to behave similarly, for PC, PE and PS lipids.

Our findings show that for the phospholipid monolayers ’buried’ water molecules exist. VSFG is very sensitive to this type of water; more sensitive, apparently, than to the water underneath the headgroup region. One might expect a larger contribution from the latter, as the water density below the headgroup is larger, when compared to water above the headgroup [19]. However, the charge-induced alignment of water molecules is strongly dependent on the local relative dielectric permittivity ε_r [20]. It has been shown that the dielectric permittivity has very large values in the region right below the lipid headgroup, reaching several 100’s compared to the value of 80 for bulk water. This high local dielectric response is caused by the dipoles associated with the headgroup charges, and results in efficient screening of these charges, giving rise to less oriented water molecules below the headgroup. Above the headgroup, in the region of the alkyl chains, the dielectric function is low (ε_r=3) [20], and water will be strongly oriented.

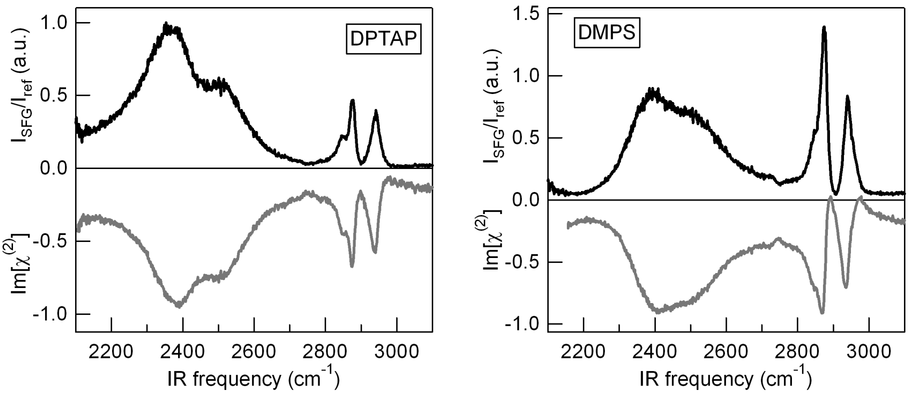

Figure 7.5 The SFG spectra (black) and the corresponding imaginary part of the nonlinear susceptibility (grey), Im[$\chi^{(2)}$], obtained from MEM analysis for the charged lipids on D_2O subphase: DPTAP (left panel) and DMPS (right panel), respectively.

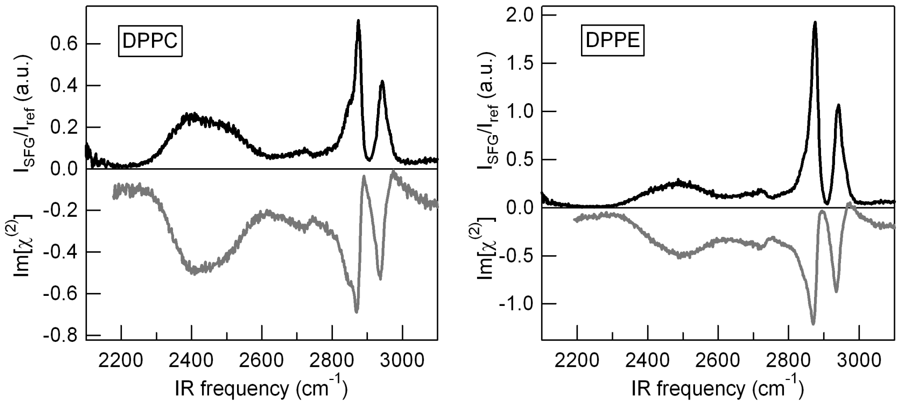

Figure 7.6 The SFG spectra (black) and the corresponding imaginary part of the nonlinear susceptibility (grey), Im[$\chi^{(2)}$], obtained from MEM analysis for the zwitterionic lipids on D_2O subphase: DPPC (left panel) and DPPE (right panel), respectively.

The existence of 'buried' water molecules revealed here furthermore can explain the results obtained from a recent time-resolved SFG experiment by Ghosh *et al.* [21]. There, it was demonstrated that the energy transfer between the water molecules at the phospholipid-water interface is slower when compared with water-air interface. These results can now be easily explained by the existence of water molecules sitting between the lipid headgroup and its apolar alkyl chain that are isolated from the water bulk. As such, the energy transfer between these isolated water molecules and the bulk will be slower.

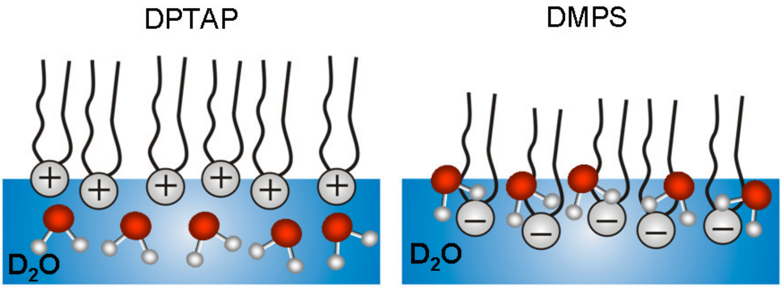

Figure 7.7 Schematic representation of the water orientation at lipid-water interface. For both DPTAP and DMPS monolayers, the water molecules orient in the same fashion, with their oxygen towards the surface. This orientation is counter-intuitive for the anionic DMPS monolayer, revealing the existence of ‘buried’ water molecules between the headgroup and the lipid tails.

7.4.3 Water structure at water-lipid interface

In order to quantify the change in the water structure near the different lipid headgroups, we compare the spectra obtained for the different lipid monolayers on isotopically diluted water subphase (D_2O:H_2O 1:3). On such subphase, the SFG spectra are simpler, as the intra- and possible the inter-molecular couplings are decoupled. The obtained spectra for the isotopically diluted sample are displayed in Figures 7.8 and 7.9 for the charged and for the zwitterionic lipids, respectively. The data is analyzed using both the Maximum Entropy Method and a spectral fit. From the MEM analyses, we find that the Im[$\chi^{(2)}$] spectra has negative values in both C-H and O-D stretch region. These results indicate that HDO water molecules orient in the same way as the D_2O water molecules for all lipid monolayers, as expected. Further, the SFG spectra are fitted using a Lorentzian model, as described in chapter 2. The fit results in conjunction with the MEM results are used to infer the water structure near the different lipid monolayer. More specific, the central frequency of the peak appearing in the HDO spectrum can be used as an indication of the H-bond strength: for a weaker H-bond strength, the central frequency shift to higher frequencies. Furthermore, the peak width is a marker of the water heterogeneity: for a more heterogeneous structure of water molecule, a broader peak is observed.

The MEM results indicate that, in contrast to the water-air interface, there are no peaks at low frequency that are not directly apparent form the intensity spectrum. The MEM results further provide us with the sign of the amplitudes of the susceptibility contributions, and with a physically realistic range for non-resonant phase. The data are readily modeled using these constraints, and the fitting results are listed in table 7.2. Our results show that water molecules near the DPTAP headgroups have stronger H-bonds when compared with the water near the phospholipids headgroup. This observation indicate that the water molecules situated

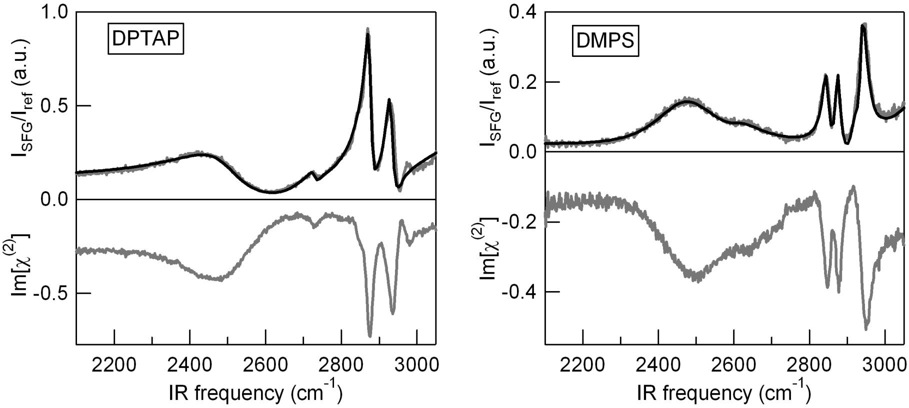

Figure 7.5 The SFG spectra for isotopic mixture D_2O:H_2O 1:3 (D/(D+H)=0.25) and the corresponding imaginary part of the nonlinear susceptibility, Im[$\chi^{(2)}$], obtained from MEM analysis for the charged lipids: DPTAP (left panel) and DMPS (right panel), respectively. The solid black lines represent fits to the data using a Lorentzian model, as described in chapter 2.

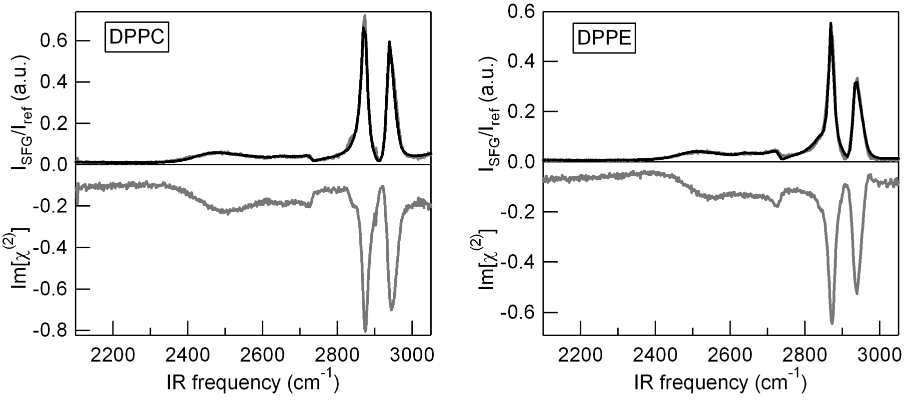

Figure 7.6 The SFG spectra for isotopic mixture D_2O:H_2O 1:3 (D/(D+H)=0.25) and the corresponding imaginary part of the nonlinear susceptibility, Im[$\chi^{(2)}$], obtained from MEM analysis for the zwitterionic lipids: DPPC (left panel) and DPPE (right panel), respectively. The solid black lines represent fits to the data using a Lorentzian model, as described in chapter 2.

Lipid	ν_{HDO}(cm^{-1})	Γ_{HDO}(cm^{-1})
DPTAP	2470	240
DMPS	2500	200
DPPC	2510	150
DPPE	2540	130

Table 7.2 The values of the peak positions and widths for the DPTAP, DMPS, DPPC and DPPE monolayers, respectively.

below the lipid headgroup where the water density is large (as for DPTAP) have stronger H-bonds with the neighboring water molecules than the 'buried' water situated above the headgroup where the water density decreases (as it is the case for the phospholipids). The existence of water molecules above the phospholipid headgroup with weaker H-bonds is further corroborated by the appearance of the high frequency peak centered around 2650 cm^{-1}.

This peak is present only for the phospholipids (being more pronounced for DMPS) and is absent for DPTAP monolayer (see Figures 7.5 and 7.6). A similar peak has been observed for neutral lipid monolayers that contains phenyl groups in the headgroup [22]. The presence of this high frequency peak indicates once more that the 'buried' water molecules detected for the phospholipid monolayers form a weaker H-bond network when compared with the water situated below the lipid headgroup, in the vicinity of the bulk water.

We can now also compare the widths of the HDO peak. As seen in table 7.2, the HDO peak is broader for the charged lipids when compared with the zwitterionic lipids. Increased broadening upon stronger hydrogen bonding is a general phenomenon in hydrogen bonded systems, and is an indication that the water vibrational dynamics is faster and/or that the water structure is more heterogeneous in the vicinity of the charged headgroups, presumably a combination of both. Further, when the zwitterionic lipids are compared, the width of the HDO peak increases from 130 cm^{-1} for DPPE to 150 cm^{-1} for DPPC, indicating an increase in the heterogeneity of water structure near DPPC monolayer when compared with DPPE monolayer. This observation is in good qualitative agreement with the literature, where it was demonstrated that PC headgroups are more hydrated when compared with PE headgroups; it seems intuitive that the range of possible hydrogen bonding conformations increases with increasing hydration.

7.5 Conclusions

In conclusion, we used Sum-Frequency Generation Spectroscopy in conjunction with Maximum Entropy Method to determine the absolute water orientation near surfactant-water and lipid-water interfaces. We have investigated the water orientation for monolayers prepared on D_2O and on isotopically diluted water subphase. Our results show that water molecules reverse their orientation when going from negative to positive surfactant-water interface. For phospholipid monolayers, we experimentally reveal the existence of 'buried' water molecules, situated between the lipid headgroups and their alkyl chains. Those interfacial water molecules do not simply terminate the bulk and illustrate the complexity of biological aqueous interfaces. Furthermore, from isotopic dilution experiments, we have determined the water structure near different types of lipid headgroups. We found that water molecules situated below the simple lipid headgroup has stronger H-bonds with the neighboring water molecules when compared with the 'buried' water molecules detected near the phospholipids headgroup. In addition, the water structure is more heterogeneous near charged lipid interfaces, due to a larger amount of water molecules that are aligned by the local electric field created at the surface.

References

[1] P. M. Wiggins, Microbiol. Rev. **54**, 432 (1990).

[2] M. S. Cheung, A. E. Garcia, and J. N. Onuchic, Proc. Nat. Acad. Sci. U.S.A. **99**, 685 (2002).

[3] H. Bursing, S. Kundu, and P. Vohringer, J. Phys. Chem. B **107**, 2404 (2003).

[4] G. L. Jendrasiak and R. L. Smith, Cell. Mol. Biol. Lett. **5**, 35 (2000).

[5] M. J. Higgins, M. Polcik, T. Fukuma, et al., Biophys. J. **91**, 2532 (2006).

[6] J. Milhaud, Biochim. Biophys. Acta **1663**, 19 (2004).

[7] Q. Du, R. Superfine, E. Freysz, et al., Phys. Rev. Lett. **70**, 2313 (1993).

[8] E. A. Raymond and G. L. Richmond, J. Phys. Chem. B **108**, 5051 (2004).

[9] M. Sovago, E. Vartiainen, and M. Bonn, J. Phys. Chem. C **113**, 6100 (2009).

[10] D. K. Hore, D. K. Beaman, D. H. Parks, et al., J. Phys. Chem. B **109**, 16846 (2005).

[11] P. K. Yang and J. Y. Huang, J. Opt. Soc. Am. B: Opt. Phys. **14**, 2443 (1997).

[12] S. Nihonyanagi, S. Yamaguchi, and T. Tahara, J. Chem. Phys. **in press** (2009).

[13] H. A. Rinia, M. Bonn, M. Muller, et al., Chem. Phys. Chem. **8**, 279 (2007).

[14] P. Guyot-Sionnest, J. H. Hunt, and Y. R. Shen, Phys. Rev. Lett. **59**, 1597 (1987).

[15] M. Sovago, R. K. Campen, G. W. H. Wurpel, et al., Phys. Rev. Lett. **100**, 173901 (2008).

[16] M. Oh-e, A. I. Lvovsky, X. Wei, et al., J. Chem. Phys. **113**, 8827 (2000).

[17] F. Zhou and K. Schulten, J. Phys. Chem. **99**, 2194 (1995).

[18] G. A. Yeghiazaryan, A. H. Poghosyan, and A. A. Shahinyan, Physica A **362**, 197 (2006).

[19] R. A. Bockmann, A. Hac, T. Heimburg, et al., Biophys. J. **85**, 1647 (2003).

[20] H. A. Stern and S. E. Feller, J. Chem. Phys. **118**, 3401 (2003).

[21] A. Ghosh, M. Smits, J. Bredenbeck, et al., J. Am. Chem. Soc. **129**, 9608 (2007).

[22] Z. Zhang, D. Zheng, Y. Guo, et al., Phys. Chem. Chem. Phys. **11**, 991 (2008).

Appendix A

Determining the molecular orientation from Sum-Frequency Generation spectra

In this appendix, the basic theory used to determine the molecular orientation from Sum-Frequency Generation (SFG) spectra is presented. In order to find the molecular orientation from SFG spectra, we need to relate the macroscopically generated SFG field to the properties of the interfacial molecules. We will treat the interface as a three layer system (as shown by Figure A.1), with two centrosymmetric media (with the refractive index n_1 and n_2, respectively) and an interfacial layer (characterized by the refractive index n’). The incident fields, E_{VIS} and E_{IR}, will generate a second-order nonlinear polarization in the interfacial layer, given by:

$$P^{(2)}(\omega_{SFG}=\omega_{VIS}+\omega_{IR})=\chi_{eff}^{(2)}(\omega_{SFG})E_{VIS}(\omega_{VIS})E_{IR}(\omega_{IR}) \qquad \text{(A.1)}$$

where $\chi_{eff}^{(2)}(\omega_{SFG}=\omega_{VIS}+\omega_{IR})$ is the effective second-order susceptibility.

Under the electric-dipole approximation, the nonlinear polarization generated in medium 1 and 2 are zero due to the inversion symmetry. Then the interfacial polarization generated in the reflected direction is the dominating source of radiation for SFG. From the radiated electric field, the SFG intensity can be determined:

$$I(\omega_{SFG})=\frac{8\pi^3\omega_{SFG}^2\sec^2\beta_{SFG}}{c^3 n_1(\omega_{SFG})n_1(\omega_{VIS})n_1(\omega_{IR})}|\chi_{eff}^{(2)}|I_{VIS}I_{IR}\ , \qquad \text{(A.2)}$$

where $n_1(\omega_i)$ is the refractive index of medium 1 at frequency ω_i, $I_{VIS}(\omega_{VIS})$ and $I_{IR}(\omega_{IR})$ are the intensities of the two incoming beams.

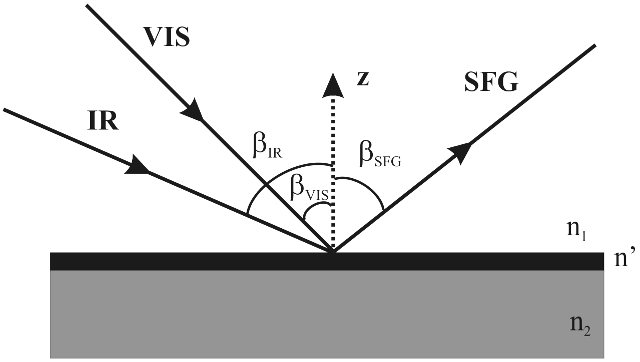

Figure A.1 Geometry of the SFG experiment. The incident angles of the VIS and IR beams on the surface are β_{VIS} and β_{IR}, respectively. The reflection angle of the sum-frequency field is β_{SFG}. The *z* axis of the lab coordinates id along the surface normal, while *x* and *y* in the plane of the surface.

The SFG electric field is not only dependent on the second-order susceptibility, but also on the linear interactions between the incoming fields and the surrounding media. The effective susceptibility can take into account both this effects, and will be given by:

$$\chi_{eff}^{(2)}=\left[u_{SFG}L(\omega_{SFG})\right]\chi^{(2)}\left[u_{VIS}L(\omega_{VIS})\right]\left[u_{IR}L(\omega_{IR})\right] . \qquad \text{(A.3)}$$

Here $\boldsymbol{u}_i$ is the unit polarization vector and $L(\omega_i)$ is the Fresnel factor at frequency ω_i.

For an azimuthally isotropic interface, only four independent elements of the non-linear susceptibility are non-zero, namely $\chi_{xxz}=\chi_{yyz}$, $\chi_{xzx}=\chi_{yzy}$, $\chi_{zxx}=\chi_{zyy}$ and χ_{zzz}. Note that the *x* and *y* directions are interchangeable for such a medium. These four components can be determined from measuring the effective susceptibility under different polarization combinations of the SFG, VIS and IR beams, respectively. Those polarization combinations are *ssp* (with *s*-polarized SFG, *s*-polarized VIS and *p*-polarized IR), *sps*, *pss* and *ppp*. The effective susceptibilities under these polarization conditions can be calculated from equation A.3:

$$\chi_{eff,ssp}^{(2)}=L_{yy}(\omega_{SFG})L_{yy}(\omega_{VIS})L_{zz}(\omega_{IR})\sin\beta_{IR}\chi_{yyz} ,$$

$$\chi_{eff,sps}^{(2)}=L_{yy}(\omega_{SFG})L_{zz}(\omega_{VIS})L_{yy}(\omega_{IR})\sin\beta_{VIS}\chi_{yzy} ,$$

$$\chi_{eff,pss}^{(2)}=L_{zz}(\omega_{SFG})L_{yy}(\omega_{VIS})L_{yy}(\omega_{IR})\sin\beta_{SFG}\chi_{zyy} , \qquad \text{(A.4)}$$

$$\begin{aligned}\chi_{eff,ppp}^{(2)}=&-L_{xx}(\omega_{SFG})L_{xx}(\omega_{VIS})L_{zz}(\omega_{IR})\cos\beta_{SFG}\cos\beta_{VIS}\sin\beta_{IR}\chi_{xxz}\\&-L_{xx}(\omega_{SFG})L_{zz}(\omega_{VIS})L_{xx}(\omega_{IR})\cos\beta_{SFG}\sin\beta_{VIS}\cos\beta_{IR}\chi_{xzx}\\&+L_{zz}(\omega_{SFG})L_{xx}(\omega_{VIS})L_{xx}(\omega_{IR})\sin\beta_{SFG}\cos\beta_{VIS}\cos\beta_{IR}\chi_{zxx}\\&+L_{zz}(\omega_{SFG})L_{zz}(\omega_{VIS})L_{zz}(\omega_{IR})\sin\beta_{SFG}\sin\beta_{VIS}\sin\beta_{IR}\chi_{zzz} ,\end{aligned}$$

where $L_{xx}(\omega_i)$, $L_{yy}(\omega_i)$ and $L_{zz}(\omega_i)$ are the diagonal elements of $L(\omega_i)$, given by:

$$L_{xx}(\omega_i)=\frac{2\mathrm{n}_1(\omega_i)\cos\gamma_{SFG}}{n_1(\omega_i)\cos\gamma_{SFG}+n_2(\omega_i)\cos\beta_{SFG}} ,$$

$$L_{yy}(\omega_i)=\frac{2\mathrm{n}_1(\omega_i)\cos\beta_{SFG}}{n_1(\omega_i)\cos\beta_{SFG}+n_2(\omega_i)\cos\gamma_{SFG}} ,$$

$$L_{xx}(\omega_i)=\frac{2\mathrm{n}_2(\omega_i)\cos\beta_{SFG}}{n_1(\omega_i)\cos\gamma_{SFG}+n_2(\omega_i)\cos\beta_{SFG}}\left(\frac{n_1(\omega_i)}{n'(\omega_i)}\right)^2 .$$

Here γ_{SFG} is the refracted angle of the SFG beam.

The macroscopic sum frequency susceptibility tensors, χ_{ijk}, in the equations A.4 are related to the microscopic hyperpolarizability tensor elements, α_{lmn}, through a coordinate transformation from the molecular coordinates system (*a*, *b*, *c*) to the lab frame (*x*, *y*, *z*):

$$\chi_{ijk}^{(2)}=N_S\sum_{lmn}\langle(\hat{i}\,\hat{l})(\hat{j}\,\hat{m})(\hat{k}\,\hat{n})\rangle\,\alpha_{lmn}^{(2)} \qquad \text{(A.5)}$$

Here N_S is the number of molecules at the surface and subindices *i*, *j*, *k* refer to the lab reference frame (*x*, *y*, *z*) and *l*, *m*, *n* to the molecular reference frame (*a*, *b*, *c*). The angular brackets denote orientational average over the molecules.

In calculating the expression connecting the χ_{ijk} tensor elements to the α_{lmn} tensor elements, one needs to take into consideration the transformation of the all Euler angles (θ, ϕ, ψ) and the appropriate molecular symmetry [1]. We are interested in determining the molecular orientation for a lipid monolayer, which is cylindrically symmetric along the *c* axis. The terminal methyl CH_3 mode belongs to the $\boldsymbol{C_{3v}}$ symmetry group. In such a case, there are 11 non-vanishing microscopic hyperpolarizability elements, namely: $\alpha_{aac}=\alpha_{bbc}$, α_{ccc}, $\alpha_{aca}=\alpha_{bcb}$, $\alpha_{caa}=\alpha_{cbb}$, $\alpha_{aaa}=-\alpha_{bba}=-\alpha_{abb}=-\alpha_{bab}$. The first three terms are symmetric terms, corresponding to the symmetric stretch, and the last terms are asymmetric terms, corresponding to the asymmetric stretch mode. When both the SFG and the VIS frequencies are off resonance, then $\alpha_{aca}=\alpha_{caa}$. Then for an azimuthally isotropic surface, the tensor elements of χ_{ijk} are obtain from equation A.5 through integration over the two Euler angles, ϕ and ψ.

For the symmetric stretch (ss), it was obtained [2, 3]:

$$\chi_{xxz}^{ss}=\chi_{yyz}^{ss}=\frac{1}{2}N_S\alpha_{ccc}\left[(1+r)\langle\cos\theta\rangle-(1-r)\langle\cos^3\theta\rangle\right] \qquad \text{(A.6)}$$

$$\chi_{xzx}^{ss}=\chi_{yzy}^{ss}=\chi_{zxx}^{ss}=\chi_{zyy}^{ss}=\frac{1}{2}N_S\alpha_{ccc}(1-r)\left[\langle\cos\theta\rangle-\langle\cos^3\theta\rangle\right]$$

$$\chi_{zzz}^{ss}=N_S\alpha_{ccc}\left[r\langle\cos\theta\rangle+(1-r)\langle\cos^3\theta\rangle\right]$$

where the hyperpolarizability ratio is $r=\alpha_{aac}/\alpha_{ccc}$ and θ is the polar angle of the molecular axis *c* with respect to the lab axis *z*.

The same relations were obtained for the asymmetric stretch (as) mode:

$$\chi^{as}_{xxz} = \chi^{as}_{yyz} = -N_S \alpha_{aca} \left(\langle \cos\theta \rangle - \langle \cos^3\theta \rangle \right)$$

$$\chi^{as}_{xzx} = \chi^{as}_{yzy} = \chi^{as}_{zxx} = \chi^{as}_{zyy} = N_S \alpha_{aca} \langle \cos^3\theta \rangle \qquad \text{(A.7)}$$

$$\chi^{as}_{zzz} = 2\mathrm{N}_S \alpha_{aca} \left(\langle \cos\theta \rangle - \langle \cos^3\theta \rangle \right)$$

To calculate the orientation angle of the methyl group at the end of the lipid tail, we first determine the amplitudes of the CH_3 symmetric mode under different polarizations combinations from a spectral fit using equation A.2. As the value of the hyperpolarizability ratio r is known from literature for a lipid monolayer ($r = 2.3$) [4], only two polarization combinations measurements are necessary. We used the amplitudes of the effective second-order susceptibility from *ssp* and *ppp* SFG spectra for the symmetric CH_3 mode: $\chi_{eff,ssp}$ and $\chi_{eff,\ ppp}$. The effective susceptibilities are related to the angle θ, our quantity of interest, via equations A.4 and A.6. This procedure of calculating the molecular orientation was used in chapter 3.

A similar way of determining the angle is to use amplitudes of the symmetric and asymmetric modes of the CH_3 measured under the same polarization combination. We used this procedure in chapter 4, where the molecular orientation is determine from the ratio of the amplitudes of the symmetric and asymmetric mode measured under *ssp* polarization combination. In this case, the ratio $\chi^{ss}_{xxz}/\ \chi^{as}_{xxz}$ is determined and further used to calculate the angle θ from equations A.6 and A.7. We used here again $r = 2.3$ and $\alpha_{caa}/\ \alpha_{aac} = 4.2$ [5].

References:

[1] C. Hirose, N. Akamatsu, and K. Domen, Appl. Spectro. **46**, 1051 (1992).

[2] C. Y. Wang, H. Groenzin, and M. J. Shultz, J. Phys. Chem. B **108**, 265 (2004).

[3] N. Akamatsu, K. Domen, and C. Hirose, J. Phys. Chem. **97**, 10070 (1993).

[4] X. Zhuang, P. B. Miranda, D. Kim, et al., Phys. Rev. B **59**, 12632 (1999).

[5] G. Ma and H. C. Allen, Langmuir **22**, 5341 (2006).

Summary

In this thesis, the molecular orientation and structure at the lipid-water interface is investigated by using vibrational sum-frequency generation (SFG) spectroscopy. Lipids are the main building block of the biological membranes. These molecules are amphiphilic molecules, having a hydrophilic headgroup and two hydrophobic tails. As such, these molecules self-assemble on the water surface- forming a lipid monolayer. This lipid monolayer closely resembles the cell membrane, as the two lipid monolayers that form the membrane are weakly coupled. Water molecules surrounding the membrane, plays an important role in membrane formation and function. Therefore, the lipid-water interface represents a good model system for the biological membrane.

A non-invasive way of investigating the molecular structure is to use vibrational spectroscopy, as described in chapter 1. By probing specific molecular vibrations, knowledge about the local environment can be gained. As an illustration, let us consider the hydrogen-bonded network of water molecules. When a water OH group forms a hydrogen bond, the O-H stretch frequency of this group decreases by an amount determined by the H-bond strength. Therefore, the frequency and lineshape of the O-H stretch vibration of water provides a sensitive probe of the local environment of water molecules. As such, vibrational spectroscopies can be used to investigate water structure.

A distinct challenge, however, in investigating the surfaces lies in specifically probing vibrations originating only from the molecules forming the surface, as for the majority of experimental approaches the response of the minor fraction of interfacial water molecules remains buried beneath the bulk response. A solution to this problem is the even-order non-linear optical techniques, as sum-frequency generation spectroscopy. Its selection rules result in the suppression of the signal from the isotropic bulk, and make it inherently sensitive to the region where the symmetry is broken, i.e. the interface. In SFG spectroscopy, an infrared (IR) and a visible (VIS) beam are combined at an interface to generate a signal at the sum frequency of the infrared and visible frequencies. When the IR frequency is resonant with the molecular vibrations at the surface, the sum-frequency signal can be strongly enhanced, providing the vibrational spectrum of essentially one molecular layer at the interface. Here, SFG spectroscopy is used to probe molecular vibrations from both lipid and water molecules at the lipid-water interface.

In chapter 2, we introduce in detail the technique of broad-band sum-frequency generation. In this approach, a femtosecond IR pulse is combined at the surface with a picosecond VIS pulse (the VIS narrow spectral bandwidth providing the spectral resolution of the SFG experiment). The IR pulse typically covers a frequency window of ~200 cm^{-1}, such that a multitude of vibrational modes are probed by the infrared profile at once. In this chapter, we use the broad window of the IR pulse to probe the modes from the lipid tails (the C-H stretch modes). The advantage of this approach is that the sample response is recorded with every individual laser pulse at all frequencies. Therefore, all data points in the SFG spectrum are measured under the same conditions. Since in this mode of operation every pair of laser pulses contributes to the whole spectrum, the signal-to-noise ratio of the acquired spectra in broad-band configuration is inherently not limited by the laser fluctuations, generally leading to improved SFG spectra. Further improvement of the broad-band SFG techniques is achieved when the IR frequency is swung over a region of ~1200 cm^{-1} for probing simultaneously lipid and water vibrations. Typical SFG spectra obtained with broad-band SFG are shown and analyzed in chapter 2 of this thesis.

Another improvement of the broad-band SFG setup is presented in chapter 3. Namely, a new conformation of the setup allows for the simultaneous recording of SFG spectra with different polarization combinations of the SFG, visible and infrared beams. By placing a displacing prism in the generated SFG beam, the different polarizations of the SFG can be separated and detected simultaneously. This method is particularly advantageous for studies in which surface properties are time-dependent, such as kinetic studies. The technique is illustrated by a study that mimics the lung surfactant relaxation during the breathing cycle: a lipid monolayer is compressed from a disordered phase to an ordered phase, and then the monolayer is allowed to relax to its initial state. During the relaxation process, the lipid tails are first changing their orientation on a time scale of tens of seconds, and subsequently the lipids respread to form a homogeneous disordered phase.

In chapter 4, we investigate the conformational change of a lipid monolayer as a function of surface pressure. Those conformational changes are quantified by using the ratio between the CH_3 and CH_2 symmetric stretch oscillator strengths from the lipid tails. This ratio represents an sensitive measure of the order of the lipid tails, as the CH_2 intensities decrease when the surface pressure of the monolayer increases, while the CH_3 intensities increase due to a narrowing of the angular distributions of chain tilt angles. Using this ratio as an order parameter for the lipid monolayers, in conjunction with surface pressure measurements and fluorescence microscopy, the effect of ions on the lipid monolayers is measured. Two types of lipid monolayers are investigated: a zwiterionic and an anionic lipid. We find that the presence of sodium ions does not change significantly the lipid monolayer structure. In contrast, the divalent calcium ion effect on monolayer is large and the effect strongly depend on the surface pressure. At low surface pressures (~5 mN/m), the presence of Ca^{2+} results in the unexpected appearance of ordered domains, while at pressures between ~5 and ~25 mN/m, Ca^{2+} ions induce molecular disorder in the monolayer. For pressures exceeding 25 mN/m, the calcium cations expand the monolayer, while simultaneously ordering the lipid chains. Interestingly, these effects are similar for both zwitterionic lipids and negatively charged lipids. In both SFG and surface tension measurements, the molecular signature of the association of Ca^{2+} with the lipids is evident from Ca^{2+}- induced changes in the signals corresponding to area changes of 4 Å^2/lipid – precisely the surface area of a Ca^{2+} ion. These changes also show evidence for a change in lipid:Ca^{2+} complexation at high pressures: from 1:1 to 1:2 Ca^{2+}-lipid complex.

The next chapter focuses on the SFG spectrum of interfacial water, and the interpretation of the double-peaked structure that appears in the vibrational surface response for all aqueous interfaces. We demonstrate that the two spectral features originate from vibrational coupling between the stretch and bending overtone, rather than from structural effects. This new interpretation is demonstrated by isotopic dilution experiments, which reveal a smooth transition from two peaks to one peak, as D_2O is replaced by HDO. Our results show that the water interface is structurally more homogeneous than previously thought. Furthermore, these results imply that the average hydrogen bond strength and its distribution must be inferred through the center frequency and width, respectively, of the O-D stretch vibration of isotopically diluted HDO in H_2O. We find that at the HDO-air interface, the SFG spectrum in the hydrogen-bonded region strongly resembles the Raman spectrum, indicating that at this interface the interfacial hydrogen bonding properties are very similar to those in bulk water. In contrast, for HDO interfaces of silica-water and lipid-water, interfacial hydrogen bonding is substantially stronger, with a larger degree of heterogeneity. The larger heterogeneity can be easy understood due to the water association with either the silica surface or the lipid headgroups.

In chapter 6, the molecular orientation at the interface is determined by applying the Maximum Entropy Method (MEM) to the SFG spectra. MEM is a numerical algorithm that retrieves the absolute phase of the sum-frequency signal. From the obtained absolute phase we are able to determine the molecular orientation – i.e. whether molecular groups are pointing ‘up’ or ‘down’ – with respect to the interface. The phase retrieval algorithm is successfully applied to spectra containing different resonance widths and various levels of nonresonant backgrounds. For the negatively charged SiO_2-water interface (giving rise to an SFG spectrum with broad vibrational peaks), we find that the water molecules are oriented with their hydrogen atoms toward the surface. For the surfactant monolayers on either water or gold substrate we find, as expected, that the methyl groups point away from the surface.

In the final chapter, the water orientation and structure near different types of lipid headgroups is determined by combining the methods presented in chapter 5 and 6. Namely, the water structure is determined from the lineshape of SFG spectra of the HDO molecules, while the molecular orientation is determined from the phase of the SFG spectra, retrieved using MEM. In this chapter, we compare the water orientation at phospholipid-water interface with the orientation found at simple surfactants-water interfaces. Our results demonstrate that water molecules at classical cationic surfactant are oriented with its O-H groups pointing down, i.e. with its oxygen towards the surfactant charge, and that the orientation is inverted when the surfactant charge becomes negative. Remarkably, at the negatively charged phosholipid-water interface and at the zwitterionic lipid-water interface, water orients with their oxygen up, towards the air phase. The orientation of water at phospholipid interfaces is therefore opposite to those of simple surfactants, which is due to the presence of ‘buried’ water molecules between the phospholipid headgroups and their alkyl chain. Following this approach, we also study the change in the water *structure* near the different types of lipid headgroups. We find that water molecules situated below the lipid headgroup form stronger H-bonds than the ‘buried’ water molecules. Additionally, we find that charged lipid headgroups induce a larger heterogeneity of water structure. The results presented in this chapter show that interfacial water molecules near lipid headgroup do not simply terminate the bulk, and illustrate the complexity of water near biological membranes.

Samenvatting

Dit proefschrift beschrijft onderzoek naar de structuur en oriëntatie van moleculen aan het water-lipide oppervlak. Voor dit onderzoek werd vibrationele som-frequentie generatie (SFG) spectroscopie gebruikt.

Lipiden zijn de belangrijkste bouwstenen van biologische membranen. Deze moleculen hebben een tweeslachtig karakter. Ze hebben een hydrofiele kop en hydrofobe staarten. Hierdoor vormen deze moleculen vanzelf een monolaag op het water oppervlak. Deze monolaag lijkt sterk op een biologisch membraan, omdat de twee monolagen waaruit een biologisch membraan bestaat maar zwak gekoppeld zijn. Water moleculen in the omgeving spelen een belangrijke rol bij de formatie en het functioneren van het membraan. De lipide-monolaag op water is een goed modelsysteem voor de interactie van water met biologische membranen.

Een niet-invasieve methode om de moleculaire structuur te bestuderen is vibrationele spectroscopie, zoals beschreven in hoofdstuk 1. Door specifieke moleculaire vibraties te meten, kan men iets te weten komen over hun lokale omgeving. Ter illustratie kijken we naar water verbonden door een netwerk van waterstof-bruggen. Wanneer een OH-groep een brug vormt, zal de frequentie van de O-H strek vibratie afnemen. De verandering van de frequentie wordt bepaald door de sterkte van de waterstof-brug. Om deze reden zijn de frequentie en lijnvorm van de O-H strek vibratie een gevoelige indicator van de lokale omgeving van de watermoleculen. Daarom kan vibrationele spectroscopie toegepast worden om de water structuur te bestuderen.

Het is een grote uitdaging in het onderzoek naar het oppervlak, om alleen de vibraties van de moleculen die het oppervlak vormen te meten, omdat voor de meerderheid van experimentele technieken de respons van het oppervlak overschaduwd wordt door de respons van de rest van het water. Een oplossing voor dit probleem is het inzetten van een even-orde niet-lineaire techniek, zoals som-frequentie generatie spectroscopie. De selectie regels van deze techniek hebben als resultaat dat het signaal van de water massa onder het oppervlak onderdrukt wordt en het alleen gevoelig is in het gebied waar de symmetrie verbroken is; het oppervlak. Met SFG spectroscopie worden een infrarode (IR) en zichtbare (VIS) bundel gecombineerd aan het oppervlak, om de som-frequentie van deze twee bundels te genereren. Als de IR frequentie resonant is met een moleculaire vibratie aan het oppervlak, wordt het signaal versterkt, waardoor het som-frequentie spectrum overeenkomt met het vibrationele spectrum van de moleculaire monolaag aan het oppervlak. We hebben SFG spectroscopie toegepast om vibraties van de lipiden en het water aan het oppervlak te meten.

In hoofdstuk 2 introduceren we in detail de methode van breed-bandige som-frequentie generatie. In deze aanpak, wordt een femtoseconde IR puls gecombineerd men een picoseconde VIS puls. Het smalle spectrum van de VIS puls geeft de spectrale resolutie van het SFG experiment. Het IR spectrum bestrijkt typische zo'n 200 cm^{-1}, zodat meerdere vibrationele modes tegelijker tijd gemeten worden. In dit hoofdstuk gebruiken we het brede spectrum van de IR puls om de modes in de straarten van de lipiden te meten (C-H strek modes). Het voordeel van deze aanpak is dat de hele respons van het sample met elke laser puls gemeten wordt. Hierdoor wordt de data op elke positie in het spectrum onder dezelfde condities gemeten. De signaal-ruis verhouding van het spectrum wordt hierdoor inherent niet beinvloed door fluctuaties in laser puls energie, wat in het algemeen betere SFG spectra oplevert. De breedband SFG techniek kan verder verbeterd worden door de IR frequentie te 'schommelen' over een gebied van 1200 cm^{-1}, waardoor lipide- en watervibraties gelijktijdig gemeten kunnen worden. Typische spectra gemeten met breedbandige SFG worden geanalyseerd in hoofstuk 2.

Een verdere verbetering van de breedbandige SFG opstelling is beschreven in hoofdstuk 3. Namelijk, een nieuwe opbouw van de opstelling waardoor gelijktijdig SFG spectra voor verschillende polarisaties combinaties voor SFG, VIS en IR gemeten kunnen worden. Door het plaatsen van een prisma in de SFG bundel worden de polarisaties gescheiden. Deze methode heeft vooral voordelen in situaties waarin de eigenschappen van het oppervlak tijdsafhankelijk zijn. De techniek wordt gedemonstreerd met een experiment waarin het ontspannen van de longblaasjes wordt gesimuleerd: een lipide-monolaag wordt gecomprimeerd van een wanordelijke tot een geordende laag, waarna de laag losgelaten wordt en ontspant naar de begin toestand. Tijdens het ontspannen veranderen eerst de lipide staarten hun oriëntatie, waarna de lipiden spreiden tot een homogene wanordelijke fase.

In hoofdstuk 4 onderzoeken we de verandering van de conformatie van een monolaag als functie van de oppervlakte spanning. Deze veranderingen worden gekwantifiseerd door middel van de ratio tussen de CH_3 en CH_2 symmetrische strek vibraties in de lipide-staarten. Deze ratio is een gevoelige maat voor de orde in de staarten, omdat de CH_2 intensiteit afneemt wanneer de spanning in de monolaag toeneemt, terwijl de CH_3 intensiteit toeneemt door een versmalling van de distributie van hoeken waarin de straarten gedraait staan. Gebruik makend van deze ratio samen met metingen van oppervlakte spanning en fluorescentie microscopie, werd ook het effect van ionen op de monolagen gemeten. Twee typen monolagen werden bestudeerd: een laag met een zwitterionische lipide en een anionische lipide. We vonden dat natrium ionen weinig invloed hebben op de structuur van de monolaag. Echter, divalente calcium ionen hebben een significant effect op de structuur van de monolaag en dit effect hangt sterk af van de oppervlakte spanning. Bij lage oppervlakte spanning (~5 mN/m) resulteert de aanwezigheid van Ca^{2+} in het onverwacht optreden van geordende domeinen. Bij spanningen tussen 5 en 25 mN/m induceren de Ca^{2+} ionen wanorde in de monolaag. Voor spanningen groter dan 25 mN/m expandeert de monolaag onder invloed van de calcium ionen, terwijl de lipide staarten geordend worden. Interessant is dat deze effecten zowel voor zitterionische als negatief geladen lipiden optreden. In de SFG en oppervlakte spanning metingen is de binding van de Ca^{2+} ionen met de lipiden te zien door veranderingen in het signaal, corresponderend met een oppervlakte verandering van 4 $Å^2$/lipide – exact het oppervlak van een enkel Ca^{2+} ion. De veranderingen in signaal geven ook een bewijs voor de verandering van de Ca^{2+}:lipide complexen: van 1:1 naar 1:2 Ca^{2+} ionen:lipide

Het volgende hoofdstuk gaat over het SFG spectrum van water aan het oppervlak en de interpretatie van een dubbelpiek-structuur die optreedt in alle water oppervlakte spectra. We laten zien dat de twee pieken zijn te verklaren door een koppeling tussen de strek en de overtoon van de buig vibratie, in plaats van effecten in moleculaire structuur. We demonsteren dit door middel van experimenten op isotopisch verdund water. Deze experimenten laten een vloeiende overgang zien tussen een dubbelpiek naar een spectrum met één piek, wanneer D_2O wordt vervangen door HDO. Onze resultaten laten zien dat het water oppervlak in strutuur meer homogeen is dan voorheen gedacht werd. Verder laten deze resultaten zien dat de sterkte van de waterstofbrug en distributie daarin, alleen bepaald kan worden uit de centrale frequentie en breedte van de O-D strek vibratie in isotopisch verdund HDO in H_2O. We vonden dat aan het HDO-lucht oppervlak het SFG spectrum in het waterstofbrug gebied sterk lijkt op het Raman spectrum, wat suggereert dat de water structuur aan het oppervlak sterk lijkt op de structuur in de rest van het water.

In HDO-silica, water-silica en water-lipide oppervlakken zijn de waterstofbruggen daarentegen veel sterker met een grotere spreiding. Deze spreiding kan makkelijk begrepen worden door binding tussen water en silica of de lipide kopgroepen.

In hoofdstuk 6 bepalen we de moleculaire oriëntatie aan het oppervlak door de 'Maximum Entropy Method' (MEM) op de SFG spectra toe te passen. MEM is een numeriek algoritme, dat de absolute fase uit het som-frequentie signaal terug haalt. Met de bepaalde absolute fase kunnen we de oriëntatie achterhalen – bijvoorbeeld of de groepen 'omhoog' of 'omlaag' staan in het oppervlak.

MEM wordt succesvol toegepast op spectra met resonanties van verschillende breedtes en verscheidene niveaus van niet-resonante achtergrond. In het negatief geladen SiO_2-water oppervlak (SFG spectrum met brede vibratie pieken) vinden we dat water met de waterstofatomen richting het oppervlak staat. In oppervlakte-actieve stoffen op water of een goud-substraat vinden we, als verwacht, dat de methyl groepen weggedraaid van het oppervlak staan.

In het laatste hoofdstuk combineren we de methoden van hoofstuk 5 en 6 om de water structuur en oriëntie rond verschillende lipiden te bepalen. De water structuur wordt bepaald uit de lijnvorm van SFG spectra van HDO moleculen, terwijl moleculaire oriëntatie bepaald wordt uit de absolute fase van de SFG spectra (via MEM). In dit hoofdstuk vergelijken we de water oriëntatie rond fosfaatlipiden met de oriëntatie rond andere eenvoudige oppervlakte-actieve stoffen. Onze resultaten laten zien dat rond kationische oppervlakte-actieve stoffen gericht staat met de O-H groep naar beneden (met het zuurstof atoom richting de lading van de kopgroep) en dat deze richting omkeert rond anionische stoffen. Verrassend is dat rond de negatief geladen fosfaatlipiden en zwitterionische lipiden het water met zijn zuurstof omhoog, richting de lucht fase, staat. De oriëntatie van water in een fosfaatlipide oppervlak is daarom tegengesteld aan die van eenvoudige oppervlakte-actieve stoffen, hetgeen is doordat er watermoleculen 'begraven' zijn tussen de lipide kopgroepen en hun staarten.

Verder hebben we met deze aanpak de *structuur* van water rond de verschillende lipide groepen bepaald. We vonden dat water onder de lipiden sterkere waterstofbruggen vormt dan de 'begraven' moleculen. Verder zagen we dat geladen kopgroepen een grotere heterogeniteit in de water structuur veroorzaakten. De resultaten in dit hoofdstuk laten zien dat het water aan het oppervlak niet simpelweg het einde van de water massa is en illustreren de complexiteit van water nabij biologische membranen.

Acknowledgments

All the work presented in this thesis would not have been possible without the help of many people. The help and patience of my colleagues and friends will always be remembered. It is hard to thank everyone and make sure nobody is forgotten. The poem below expresses my thoughts and the gratitude for all of you, and lessons learned in four years at AMOLF. This poem is translated and adapted from the Romanian poem 'Avem timp pentru toate' ('We have time for everything') by Octavian Paler. If you recognize yourself between the lines while reading it, that is indeed you! Thank you all!

We have time for everything

To sleep, to run from left to right,
To regret that we made a mistake, and to repeat it,
To judge others and to excuse ourselves,
We have time to help and to smile; to cry and to laugh,
To be late and to lie; to hate and to love.
We have time to be frustrated and to wash it with a beer.

We have time to read and write,
To correct what we wrote, to regret that we wrote,
We have time to make plans and not to apply them.
To banish the questions and to avoid the answers.

We have time for dreams and ambitions; to blame the destiny and the details,
We have time to destroy a dream and to reinvent another one,
We have time to make friends and to loose them.
To teach and to be patient; to receive lectures and then to forget them.
We have time to write a poem,
We have time for everything.

I have learned a few things in life and I would like to share them with you.
I have learned that you cannot make someone to love you.
Everything you can do is to be a nice person. The rest…. depends on the others.

I have learned that the heroes are the ones who are doing
what should be done,
when it should be done,
no matter the consequences.

That no matter how many good friends you have,
they will make you suffer sometimes, and you'll have to forgive them.
I have learned that it is not enough to forgive,
but sometimes you have to forgive yourself as well.

I have learned that it does not matter what you have in life, but whom you have;
That it takes years to gain trust and that I can loose it just in a few seconds.
I have learned that no matter how much I care, others might not care at all.
I have learned that you have the right to be upset,
but you have no right to be unkind.

I learned that it is useful to use your charm for 12 minutes.
Afterwards, is good knowing something!
I learned that I cannot compare what others can do, but what I can do.
I have learned that two people can watch the same thing
and see completely different things.
I learned that everything has two faces.

I have learned that I can keep on going for a long time,
after I said I cannot any longer.
I have learned that no matter how much I might suffer;
the world will not stop for my pain.
That it is very difficult to draw a line between being polite,
not to offend someone and still keep your opinion.

I learned that there are people who love me, but don't know how to show it.
I learned that the true friendship exists also at long distances.
I have learned that if two people are fighting,
does not mean that they do not love each other.
And if they do not fight, does not mean that they do love.

I learned to love, so I can be loved.